Oxide Nanoelectronics

by

Cheng Cen

Bachelor of Science, University of Science and Technology of China, 2004

Master of Science, University of Pittsburgh, 2006

Submitted to the Graduate Faculty of

Art and Science in partial fulfillment

of the requirements for the degree of

Doctor of Philosophy

University of Pittsburgh

2010

UNIVERSITY OF PITTSBURGH

School of Art and Science

This thesis was presented

by

Cheng Cen

It was defended on

January 14th, 2010

and approved by

David Jasnow, Professor, Department of Physics and Astronomy

Hrvoje Petek, Professor, Department of Physics and Astronomy

Chandralekha Singh, Associate Professor, Department of Physics and Astronomy

Jennifer Lynn Gray, Assistant Professor, Department of Mechanical Engineering and Materials Science

Thesis Director: Jeremy Levy, Professor, Department of Physics and Astronomy

Oxide Nanoelectronics

Cheng Cen, PhD

University of Pittsburgh, 2010

Copyright © by Cheng Cen

2010

Oxide Nanoelectronics

Cheng Cen, PhD

University of Pittsburgh, 2010

This thesis describes research performed on two types of complex oxide heterostructures. The first consists of ultrathin $LaAlO_3$ films grown on $SrTiO_3$ substrates. At the interface between these two insulating oxides, a quasi-two dimensional electron gas may form under proper conditions. This interface has remarkable properties such as interfacial superconductivity, interfacial magnetism and a hysteretic voltage-controlled metal-insulator transition. An Atomic Force Microscope (AFM) lithography technique is developed which is capable of switching reversibly at room temperature this metal-insulator transition with nanometer scale spatial resolution. Based on this technique, conducting nanowires as thin as 2 nm and nanodots array with density up to 10^{14} inch^{-2} were written, probed and erased. Sketch-defined field effect transistors (SketchFET) with channel lengths as short as 2 nm were fabricated. These structures were characterized over a temperature range 15 K-300 K, revealing a complex energy landscape. Magnetotransport measurements performed at temperatures at and below 1 K reveal a variety of intriguing quantum phenomena, including integer and fractional quantum Hall states.

The second material system consists of thin films of $SrTiO_3$ grown directly on silicon. Although $SrTiO_3$ is not ferroelectric at any temperature in bulk form, when strained to the silicon lattice it can become ferroelectric at and above room temperature. Temperature-dependent piezo force microscopy was performed to verify that those strain engineered films with certain thickness are indeed ferroelectric. Ultrafast optical experiments were carried out to measure lattice dynamics in these strained films. A coherent acoustic phonon mode was observed and

studied as a function of film thickness and laser polarization. Using $SrTiO_3$ grown on silicon-on-insulator structures, ferroelectric field effect transistors (FeFET) were fabricated and characterized at room temperature.

TABLE OF CONTENTS

PREFACE XVI

1.0 INTRODUCTION 1

1.1 $LaAlO_3/SrTiO_3$ INTERFACE 2

1.1.1 Theory of Formation of q-2DEG 2

1.1.2 Material Fabrication 4

1.1.3 Novel properties discovered in $LaAlO_3/SrTiO_3$ interface 5

1.2 STRAINED $SrTiO_3$ THIN FILM GROWN DIRECTLY ON Si 9

1.2.1 $SrTiO_3$ 9

1.2.2 Strain Induced Ferroelectricity 10

1.2.3 Material Fabrication 12

1.2.4 Applications 14

2.0 NANOSCALE CONTROL OF AN INTERFACIAL METAL-INSULATOR TRANSITION AT ROOM TEMPERTURE 15

2.1 INTRODUCTION 16

2.2 SAMPLES INVESITIGATED 17

2.3 EXPERIMENT SET UP AND RESULTS 18

2.4 MECHANISM DISCUSSIONS 26

2.5 KELVIN PROBE IMAGING 32

2.6 CONCLUSIONS 33

3.0 OXIDE NANOELECTRONICS ON DEMAND 34

3.1 INTRODUCTION 34

3.2 SAMPLE INVESTIGATED 36

3.3 EXPERIMENTS AND RESULTS 38

3.4 DISCUSSION AND PERSPECTIVE 55

4.0 THERMAL ACTIVATION AND QUANTUM TUNNELING IN A SKETCH-BASED OXIDE NANO TRANSISTOR 57

4.1 INTRODUCTION 57

4.2 EXPERIMENT AND RESULTS 58

4.3 CONCLUSION 68

5.0 OBSERVATION OF POSSIBLE INTEGER AND FRACTIONAL QUANTUM HALL STATES IN AN INTERFACIAL OXIDE NANOSTRUCTURE 69

5.1 INTRDUCTION 70

5.2 EXPERIMENT AND RESULTS 73

5.3 DISCUSSION AND PERSPECTIVE 79

6.0 A FERROELECTRIC OXIDE MADE DIRECTLY ON SILICON 87

6.1 INTRODUCTION 88

6.2 SAMPLE INVESTIGATED 88

6.3 EXPERIMENTS AND RESULTS 91

6.4 CONCLUSION 99

7.0 FERROELECTRIC FIELD EFFECT TRANSISITORS ON SILICON 100

7.1 INTRODUCTION 100

7.2 SAMPLE INVESTIGATED ... 102

7.3 EXPERIMENTS AND RESULTS ... 102

7.4 PERSPECTIVE ... 108

8.0 TIME RESOLVED LATTICE DYNAMICS STUDY OF $SrTiO_3$ ULTRATHIN FILMS GROWN DIRECTLY ON SILICON ... 109

8.1 INTRODUCTION ... 109

8.2 SAMPLE INVESTIGATED ... 111

8.3 EXPERIMENTS AND RESULTS ... 111

8.4 CONCLUSION ... 116

9.0 SUMMARY AND OUTLOOK ... 117

10.0 EXPERIMENTAL METHODS AND THEORY ... 119

10.1 SAMPLE PREPARATION METHOD ... 119

10.1.1 Electron Beam Lithography (EBL) and photolithography ... 119

10.1.2 Dry Etching ... 121

10.1.3 Metal Deposition ... 121

10.2 ATOMIC FORCE MICROSCOPY (AFM) ... 122

10.2.1 Conductive AFM ... 124

10.2.2 Kelvin probe microscopy ... 125

10.2.3 Piezo force microscopy ... 128

10.3 ELECTRO-OPTIC EFFECT ... 130

10.3.1 Raman and Brillouin Scattering ... 130

10.3.2 Impulsive Stimulation and Probing Method ... 132

10.4 HALL EFFECT MEASUREMENT ... 134

10.4.1 Classic Hall Effect 134

10.4.2 Conventional Magnetotransport Measurements.................................... 135

10.4.3 Quantum Hall Effect 137

BIBLIOGRAPHY 142

LIST OF TABLES

Table 2-1 25

LIST OF FIGURES

Figure 1-1 Illustration of charge redistribution due to polar catastrophe at interfaces of samples grown with different termination conditions 3

Figure 1-2 Tunability of $LaAlO_3/SrTiO_3$ interface by voltage applied at the back of $SrTiO_3$ substrate. 6

Figure 1-3 Interfacial superconductivity discovered in $LaAlO_3/SrTiO_3$ 7

Figure 1-4 Sheet resistance at 0.3K of an n-type $LaAlO_3/SrTiO_3$ interface, showing hysteresis under magnetic field sweeping. 8

Figure 1-5 Ferroelectric materials have a spontaneous polarization, the direction of which can be switched by applied electric field. 11

Figure 1-6 Phase diagram for SrTiO3 under varying amounts of biaxial strain......................... 12

Figure 1-7 Cross sectional scanning transmission electron microscope (STEM) images of $SrTiO_3$ films grown on Si, conforming of the absence of a extending interface layer. 13

Figure 2-1 Writing and erasing nanowires at the $LaAlO_3/SrTiO_3$ interface 18

Figure 2-2 Current-voltage characteristics of $LaAlO_3/SrTiO_3$ interface. 21

Figure 2-3 Measuring the limits of conducting island density.. 24

Figure 2-4 Stable structures of a 3 uc $LaAlO_3$ film on $SrTiO_3$.. 26

Figure 2-5 Calculated local density of states of $LaAlO_3/SrTiO_3$ for "ideal" and reduced $LaAlO_3$ surfaces 28

Figure 2-6 Schematic band diagrams of $LaAlO_3/SrTiO_3$ heterostructures. 29

Figure 2-7 "Water cycle" model for the writing and erasing of metallic area at $LaAlO_3/SrTiO_3$ interface........ 31

Figure 2-8 Surface potential of interfacial structures measured with Kelvin probe microscopy. 32

Figure 3-1 Images of $LaAlO_3/SrTiO_3$ samples used in experiments 36

Figure 3-2 For the SketchFET structure, source-drain current measured as a function of the tip position across the wire, while cutting the wire with the tip biased negatively........ 38

Figure 3-3 Creation of nanoscale tunnel barriers. 40

Figure 3-4 T-Junction........ 43

Figure 3-5 SketchFET device 44

Figure 3-6 Mutual coupling between leads in SketchFET and double junction structure........ 45

Figure 3-7 I-V characteristics of a SketchFET with a larger barrier. 46

Figure 3-8 Frequency response of SketchFET........ 48

Figure 3-9 Double-Junction device. 50

Figure 3-10 Negative Differential Resistance (NDR)........ 51

Figure 3-11 Lateral modulation doping of nanowires 54

Figure 4-1 Schematic of the SketchFET structure and conduction band along the channel 60

Figure 4-2 *I-V* characteristic of SketchFET at 295 K, 150 K, 20 K with V_G = -2 V, 0 V, 2 V applied........ 62

Figure 4-3 Resistance of an uncut wire written with V_{tip} = 10 V as a function of temperature, exhibiting a metallic characteristic. 63

Figure 4-4 Arrhenius plot of drain current and activation energy 64

Figure 4-5 Drain current magnitude $|I_D|$ at various source bias measured at temperatures below 150 K when gate voltage V_{GD} = -2 V applied.. 65

Figure 4-6 At temperatures below 150 K, drain current plotted as a function of temperature for various gate and source biases. 67

Figure 5-1 Illustration of electron scattering environment in reduced dimensions 72

Figure 5-2 AFM image patterned $LaAlO_3/SrTiO_3$ device showing six low-resistance contacts. 73

Figure 5-3 Nanowire conductance *G* measured as a function of temperature during cooldown. 74

Figure 5-4 Even symmetry of magnetoresistance in nanowire 75

Figure 5-5 Low-temperature (*T*=0.25 K) magnetoresistance of a nanowire formed at the interface between $LaAlO_3$ and $SrTiO_3$ 77

Figure 5-6 Temperature dependence of the magnetoresistance 79

Figure 5-7 Schematic and equivalent-circuit model of nanowire 81

Figure 5-8 Equivalent circuit of a single scatter-free section of the nanowire. 82

Figure 5-9 Illustration of second nanostructure and Hall resistance data 84

Figure 6-1 Structure of the $SrTiO_3$/Si interface, written and imaged on a 6 ML thick $SrTiO_3$/Si sample by piezo force microscopy 89

Figure 6-2 The strain state of the $SrTiO_3$ films revealed by x-ray diffraction 90

Figure 6-3 Bistable piezoelectric response. 93

Figure 6-4 Retention of ferroelectric domains 95

Figure 6-5 2 μm × 2 μm AFM topography images of the 6 ML thick SrTiO3/Si sample taken simultaneously with the PFM images of Fig. S8A during a period of 72 hours.......................... 96

Figure 6-6 PFM images (1 μm × 1 μm) of a 4×4 pattern of domains written on the 5 ML thick $SrTiO_3$/Si sample at different temperatures. 97

Figure 6-7 1 μm × 1 μm PFM image of four square domain patterns written and imaged on the 6 ML thick SrTiO3/Si sample at *T*=300 K and at *T*=410 K. 98

Figure 6-8 Temperature-dependence of the out-of-plane lattice constant of $SrTiO_3$ strained commensurately to the underlying silicon substrate.. 99

Figure 7-1 Illustration of FeFETs made in $SrTiO_3$/SOI samples and the measuring sequence. 103

Figure 7-2 Nonvolatile switching effect on the Si channel conductance *G* by voltage pulse applied across the gate $SrTiO_3$. Sample favors the states with a spontaneous polarization pointing down. 104

Figure 7-3 Switching effect amplitude and absolute value of channel conductance as functions of switching pulse amplitude applied across the gate $SrTiO_3$. 106

Figure 7-4 Switching amplitude and absolute value of channel conductance as functions of voltage applied to the back of Si handle. 107

Figure 8-1 Layout of pump-probe setup and coherent phonon oscillations measured in $SrTiO_3$ films with different thicknesses. 112

Figure 8-2 Damped phonon oscillation signal extracted after background subtraction. 114

Figure 8-3 Coherent phonon oscillations in 20 ML thick $SrTiO_3$ film at three different relative polarization angles between pump and probe $\theta = 0^\circ, 45^\circ, 90^\circ$. 115

Figure 10-1 Illustration of typical photolithography procedures. 120

Figure 10-2 Illustration of essential components of an atomic force microscope and two most commonly used scanning modes: AC mode and contact mode 123

Figure 10-3 Illustration of typical operating method of Kelvin probe force microscopy 126

Figure 10-4 Illustration of in-phase and out-of-phase piezoresponse. 129

Figure 10-5 Illustration of classic Hall effect, charges accumulate at sample edges and induce a Hall voltage to balance the Lorentz force. 134

Figure 10-6 Schematic of conventional magneto transport measurement performed in a Hall bar structure.. 135

Figure 10-7 Example of quantum Hall effect measured in GaAs/AlGaAs heterostructures 137

PREFACE

I want to thank a lot of people for finally being able to get to this point. First to Jeremy, my advisor, your passion for research and inspirational guidance are most admired and appreciated. Also to friends in my lab, without you guys, all those years wouldn't be fun at all. Botao, your help got me to Pitt at the first place. Momo and S.B., your kind accompany during my thesis writing will never be forgotten.

1.0 INTRODUCTION

Semiconductors have been the workhorse of modern electronics industry for decades. To obtain ever higher device integration densities, the size of metal-oxide-semiconductor field-effect transistors (MOSFET) have been successfully reduced in scale for over four decades, in accordance with Moore's Law. Now, due to the intrinsic limitations, the scaling of MOSFET devices is truly reaching fundamental limits. Alternative device concepts are necessary not only to maintain the increase of integration intensity but also to promote the integration of greater functionality.

Complex oxides are famous for their great variety of emergent phenomena. Transition metal oxides are long known for their complex phases, structural phase transitions, metal-insulator transitions and magnetic ordering transitions. Cuprates ($YBa_2Cu_3O_7$, $La_{2-x}Sr_xCuO_4$, Bi-Sr-Ca-Cu-O, etc) are well known high T_c superconductors. Colossal magnetoresistance was discovered in manganites ($LaMnO_3$ and relatives). Ferroelectricity and piezoelectricity in $PbZr_xTi_{1-x}O_3$ have wide applications. Methods, including doping, epitaxial superlattice growth and nanoengineering techniques, intermingle ferromagnetic ordering with ferroelectric ordering and lead to a new class of multiferroic oxide materials. These novel properties make oxide electronics and the combination of oxides with semiconductors promising approaches to extend and accelerate information technology development.

My graduate research focused on two classes of complex oxide heterostructures: $LaAlO_3/SrTiO_3$ and $SrTiO_3/Si$, which are briefly introduced below.

1.1 $LaAlO_3/SrTiO_3$ Interface

$LaAlO_3$ and $SrTiO_3$ are both band insulators at room temperature (band gaps $E_g^{(LaAlO_3)} = 5.6\,eV;\ E_g^{(SrTiO_3)} = 3.2\,eV$). It was reported for the first time in 2004 by Ohtomo *et al.* [1] that a high mobility electron gas can be formed at the interface between these two insulating oxides. It was found that oxygen vacancies play an important role in contributing to high sheet conductance at the interface [1-4]. Density and motions of oxygen vacancies govern the carrier transport in samples grown under low oxygen pressures. However, in well oxidized samples, a metallic electron gas can still form and is both theoretically predicted [5-6] and experimentally found [1,7-9] to be confined within a few nanometers in $SrTiO_3$ top atomic layers, making the electron transport quasi-two dimensional. The abundant physics and various application potentials make this system subject of many studies.

1.1.1 Theory of Formation of q-2DEG

Although a complete quantitative explanation of the formation of quasi-two dimensional electron gas (q-2DEG) at the interface between $LaAlO_3$ and $SrTiO_3$ is still under debate, the most well accepted qualitative theory so far is the so called "polar catastrophe" picture as illustrated in Figure 1-1[10].

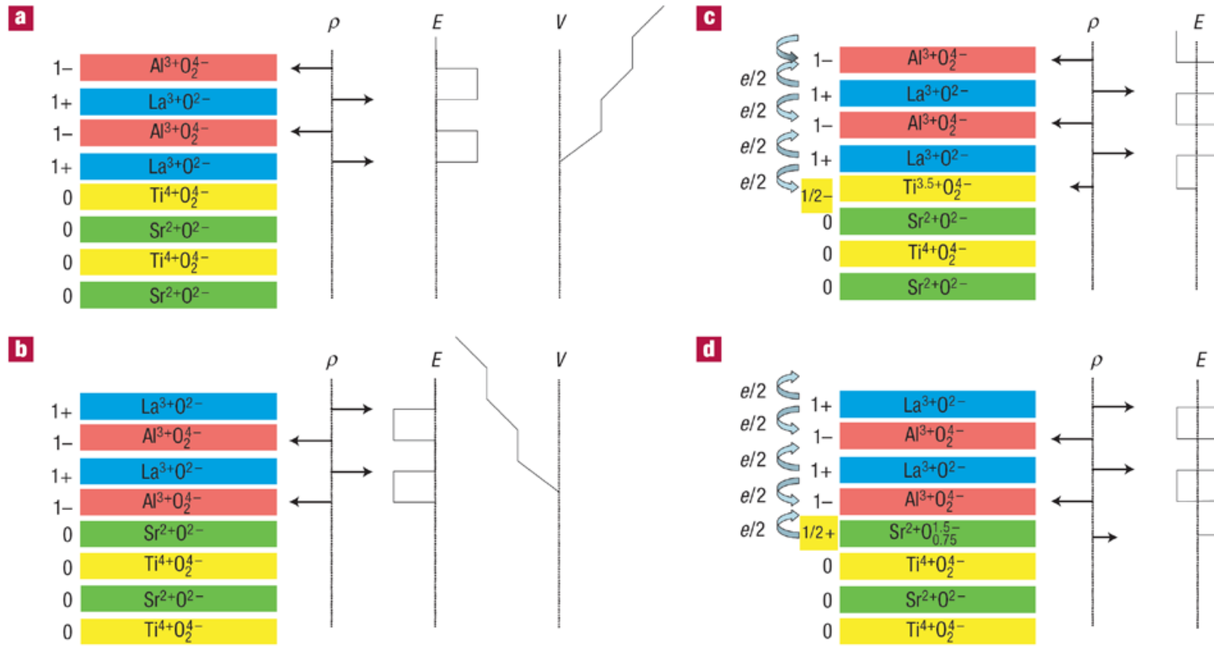

Figure 1-1 Illustration of charge redistribution due to polar catastrophe at interfaces of samples grown with different termination conditions (Adapted from Ref [10]). (a) Non-reconstructed LaO/TiO_2 interface. A positive potential exists in $LaAlO_3$ layer and diverges with film thickness. (b) A similar but negative potential occurs in the case of AlO_2/SrO interface. (c) At LaO/TiO_2 interface, adding 1/2 electron per unit cell to top TiO_2 layer can minimize the potential in $LaAlO_3$. (d) At AlO_2/SrO interface, adding 1/2 hole per unit cell to top SrO layer can minimize the potential in $LaAlO_3$.

The lattices of $LaAlO_3$ and $SrTiO_3$ are both of typical Perovskite ABO_3 structure. The growth of $LaAlO_3$ on $SrTiO_3$ is usually done with the interface parallel with ABO_3 (001) planes, which are composed of alternating layers of AO and BO_2 planes. In $LaAlO_3$, LaO (AO) layers are positively charged and AlO_2 (BO_2) layers are negatively charged, which give rise to a non-zero electric polarization perpendicular to the interface, while in $SrTiO_3$, all layers (SrO, TiO_2) are neutral in charge so there is no polarization. The discontinuity at the interface induces an electric potential in $LaAlO_3$ film diverging with the film thickness, which is called "polar

catastrophe". This non-reconstructed atomically sharp interface is energetically costly to maintain. The system can balance the polar discontinuity and minimize the potential energy through electronic reconstruction in which a net charge transfer of 1/2 electron per unit cell occurs between the top $LaAlO_3$ surface and the top $SrTiO_3$ layer. The redistribution of charge gives rise to the formation of q-2DEG at the interface.

In the case of $LaAlO_3$ films grown on TiO_2 terminated $SrTiO_3$ substrates, electrons from top $LaAlO_3$ surface will n-dope the TiO_2 layer and form a conducting interface, as observed in experiments. However, the sheet carrier density measured in fully oxidized samples is one order of magnitude smaller than the 1/2 electron per unit cell value predicted by polar catastrophe picture [2-4,7,11]. Models involving two types of carriers (localized and extended) [12] and carrier localization induced by crystal field and pseudo-Jahn-Teller effect [13] were suggested to resolve the discrepancy.

In the case of $LaAlO_3$ films grown on SrO-terminated $SrTiO_3$ substrates, holes from the top $LaAlO_3$ surface are expected to p-dope the SrO layer, but such a hole-doped interface is measured to be insulating. This absence of conductivity at the interface might be due to a lack of available mixing valence states to accommodate those extra hole (in electron doping circumstances, there are available Ti valence states of 3+ and 4+), which leads to a atomic reconstruction instead to avoid the diverging potential.

1.1.2 Material Fabrication

$SrTiO_3$ substrates are commercially available. To achieve TiO_2-terminated surfaces, (001) oriented $SrTiO_3$ substrates are first subjected to chemical etching followed by annealing in

Oxygen, while SrO-terminated surfaces are obtained by deposition of a SrO monolayer on TiO_2-terminated substrates.

The most commonly used growing method is by pulsed laser deposition (PLD) [1,7], although q-2DEG can also be obtained by molecular beam epitaxy (MBE) [14].

1.1.3 Novel properties discovered in $LaAlO_3/SrTiO_3$ interface

Tunable Metal-Insulator Transition

An interfacial insulator-to-metal transition as a function of $LaAlO_3$ thickness was discovered in 2006 by Thiel *et al.* for $LaAlO_3/SrTiO_3$ heterostructures [7]. Above a critical thickness of $LaAlO_3$ of d_c=3 unit cell (uc), the interface between $LaAlO_3$ and $SrTiO_3$ is conducting, while below d_c, the interface is insulating. In samples grown with approximately 3uc of $LaAlO_3$ which are originally insulating, the interfacial metal-insulator transition can be controlled by voltage applied at the back of $SrTiO_3$ substrate. This transition is a hyterestic function of the applied electric field (Fig. 1-2).

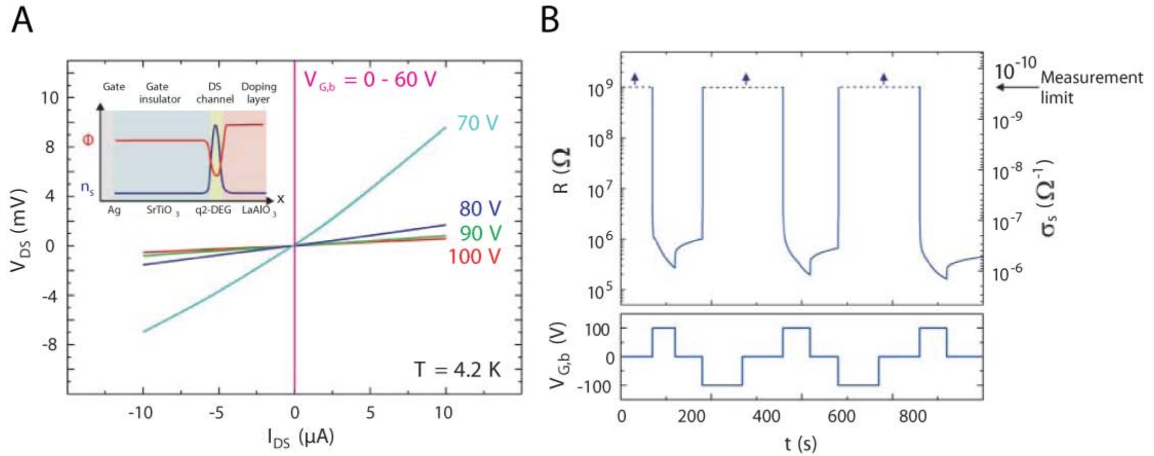

Figure 1-2 Tunability of $LaAlO_3/SrTiO_3$ interface by voltage applied at the back of $SrTiO_3$ substrate. Adapted from Ref [7]. (A) I-V characteristic showing when the voltage exceeds 60 V, the interface becomes conducting. (B) Applying a large positive voltage to the back gate makes the interface conducting. After voltage is turned off, the interface remains conducting until a negative voltage reverts it back to an insulating state.

The mechanism giving rise to metastability has not been conclusively identified. However, a plausible explanation involves the motion of oxygen vacancies in the $SrTiO_3$ substrate which are electrically charged (nominally Z=+2 in the ionic limit). As these vacancies are pushed toward the interface by positive voltages, making the interface conducting (or pulled away from the interface by negative voltages, making the interface insulating), they may reversibly and hysteretically drive the metal-insulator transition.

Interfacial Superconductivity

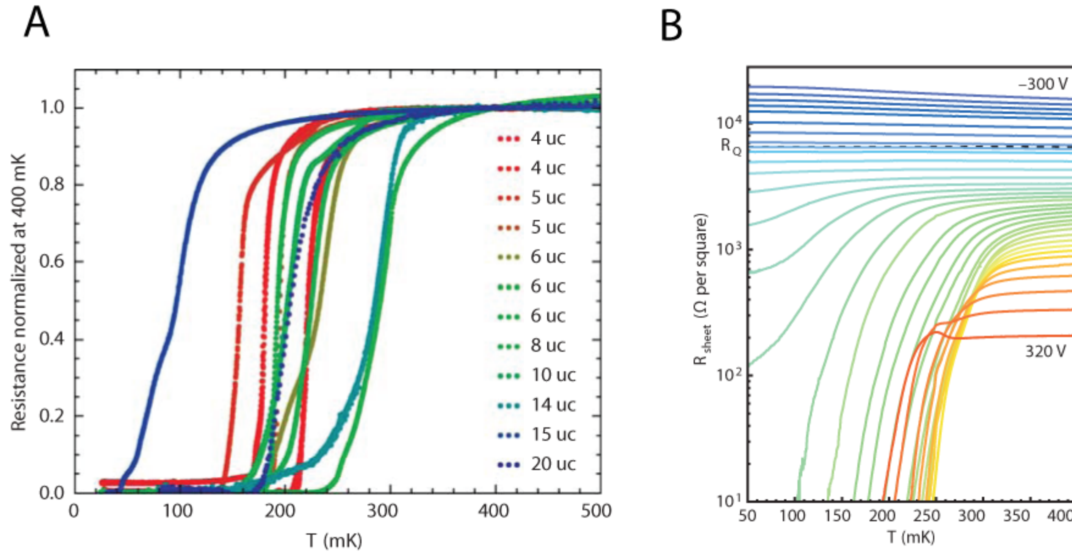

Figure 1-3 Interfacial superconductivity discovered in $LaAlO_3/SrTiO_3$ (A) $LaAlO_3/SrTiO_3$ interface is superconducting at low temperature. Adapted from Ref [15]. (B) Electric field can induce a superconductor-insulator transition. Adapted from Ref [16]

Doped $SrTiO_3$ was known for a long time to be superconducting at low temperature [17]. More recently, measurements have revealed a superconducting ground state confined to the interface between $LaAlO_3$ and $SrTiO_3$ [15]. The measured transition temperature T_c is around 200 mK (comparable to bulk superconducting $SrTiO_3$) and is $LaAlO_3$ thickness dependent [15] (Fig. 1-3 (A)). Subsequent investigations showed that applied electric fields can tune the carrier density and induce a superconductor-insulator quantum phase transition [16] (Fig. 1-3 (B)).

Interfacial Ferromagnetism

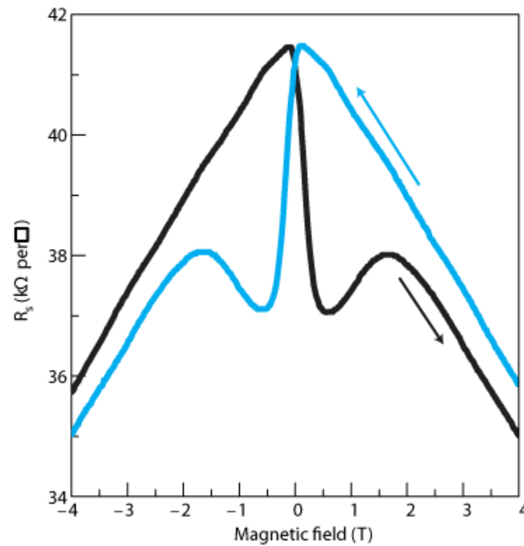

Figure 1-4 Sheet resistance at 0.3K of an n-type $LaAlO_3/SrTiO_3$ interface, showing hysteresis under magnetic field sweeping. Adapted from ref [18]

Although neither $LaAlO_3$ nor $SrTiO_3$ is magnetic , magnetotransport experiments measured a large negative magnetoresistance and magnetic hysteresis at $LaAlO_3/SrTiO_3$ interface (Fig. 1-4) at low temperature, indicating some type of magnetic ordering [18]. The origin of this magnetism has not yet been determined, although magnetic impurities have largely been ruled out.

1.2 Strained $SrTiO_3$ Thin Film Grown Directly On Si

Great effort has been made to integrate of traditional semiconductors with complex oxides. On the one hand, high-*k* dielectrics have been aggressively pursued as replacements for SiO_2 as the gate dielectric for MOSFET devices, in order to continue Moore's law scaling. On the other hand, combining the great variety of functional properties in perovskite materials with well-developed fabrication techniques of semiconductors may potentially bring new functionality that take advantage of the diverse properties of oxides. Examples include spintronic devices, ultra-high-density memories, post-CMOS logic families, and quantum information technologies.

1.2.1 $SrTiO_3$

$SrTiO_3$ is probably the most important material among perovskites, both technologically and scientifically Its multifaceted properties have been appreciated for decades. Bulk $SrTiO_3$ has a dielectric constant $\varepsilon \sim 300$ at room temperature and more than 20,000 below 4 K, which can be tuned with electric field by more than 80% [19]. These properties alone lead to various applications of $SrTiO_3$ in gate dielectrics, microwave devices and electro-optic devices. The lattice constant of $SrTiO_3$ at room temperature is 3.905Å, compared with a much larger value of 5.431Å in Si crystal. However, if rotated by 45° around [001] axis, the diagonal of $SrTiO_3$ unit cell only has a 1.7% lattice mismatch with Si, making commensurate and epitaxial growth of $SrTiO_3$ on Si feasible. Indeed, a MBE technique has been developed to successfully deposit high quality commensurate $SrTiO_3$ thin film on Si [20]. In this way, $SrTiO_3$ becomes also a useful template layer for the integration of other type of perovskite materials. $SrTiO_3$ is a model system for

studying structural and ferroelectric phase transitions. Below 4K, large quantum fluctuations destabilize the ferroelectric state of bulk $SrTiO_3$ in favor of a paraelectric state, which possesses no net polarization order even at zero temperature [21]. Reduced $SrTiO_3$ crystals undergo a superconducting transition around 250 mK [17]. Electron doped, it becomes superconducting with the lowest known carrier density of any material [22].

1.2.2 Strain Induced Ferroelectricity

Most insulators are linear dielectrics, meaning that their induced polarization scales linearly with applied electric field. Ferroelectric materials demonstrate a more pronounced nonlinear polarization. In addition to being nonlinear, they may demonstrate a spontaneous (zero-field) polarization (Fig. 1-5) below a critical temperature (called the Curie Temperature) and are called ferroelectric materials in analogy with ferromagnetic materials. The distinguishing feature of ferroelectrics is that the direction of the spontaneous polarization can be reversed by an applied electric field, yielding a hysteresis loop. Typically, materials demonstrate ferroelectricity only below a certain phase transition temperature, called the Curie temperature, T_c, and are paraelectric above this temperature.

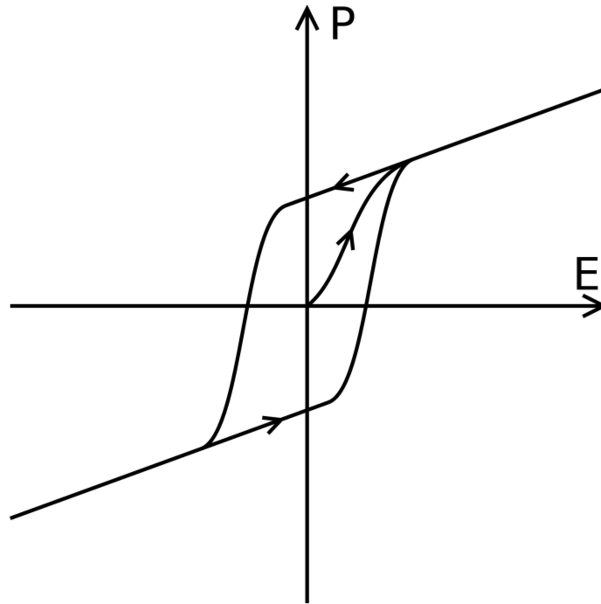

Figure 1-5 Ferroelectric materials have a spontaneous polarization, the direction of which can be switched by applied electric field.

Although known to be paraelectric down to zero temperature, strain has long known to be able to induce ferroelectricity in $SrTiO_3$ [23]. The strain imposed by the substrate onto which the films are epitaxially grown provides extra degrees of freedom to tune the behavior of the films (Fig. 1-6). It has been theoretically predicted [24] that a moderate amount of biaxial strain in $SrTiO_3$ thin film can lead to a room-temperature ferroelectric state, which was observed experimentally [20,25-27].

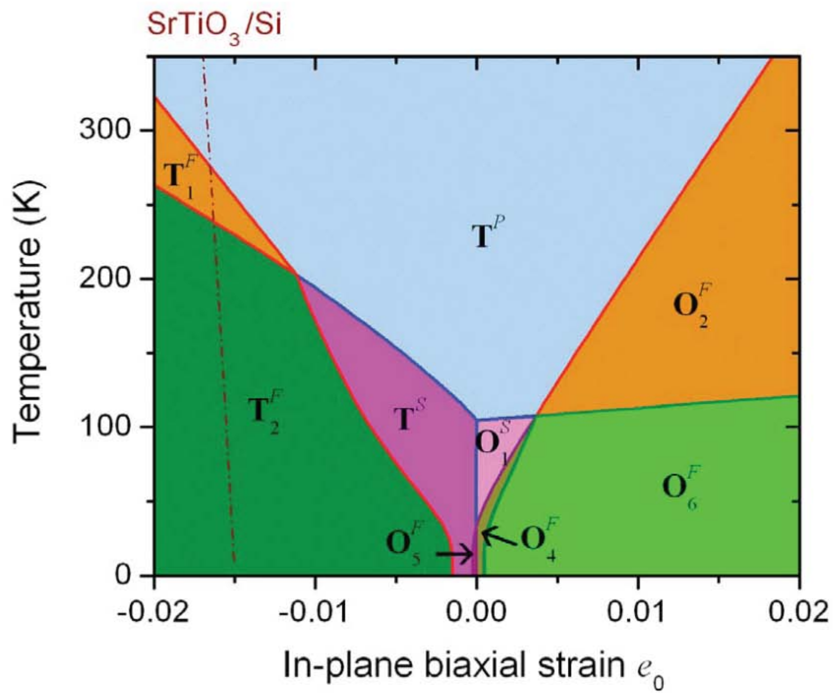

Figure 1-6 Phase diagram for $SrTiO_3$ under varying amounts of biaxial strain. Image adapted from Ref[20]. Commensurate growth on silicon corresponds to ~1.7% compressive strain at room temperature (indicated at left).

1.2.3 Material Fabrication

In many studies utilizing biaxial stress to create or enhance ferroelectricity, the substrates and films are isostructural. For $SrTiO_3$/Si, the interface is far more complex, connecting a diamond structure (Si) with a perovskite ($SrTiO_3$). Also, the high reactivity of Si with many elements and their oxides as well as the tendency of a pristine Si surface to rapidly form its own oxide present formidable challenges.

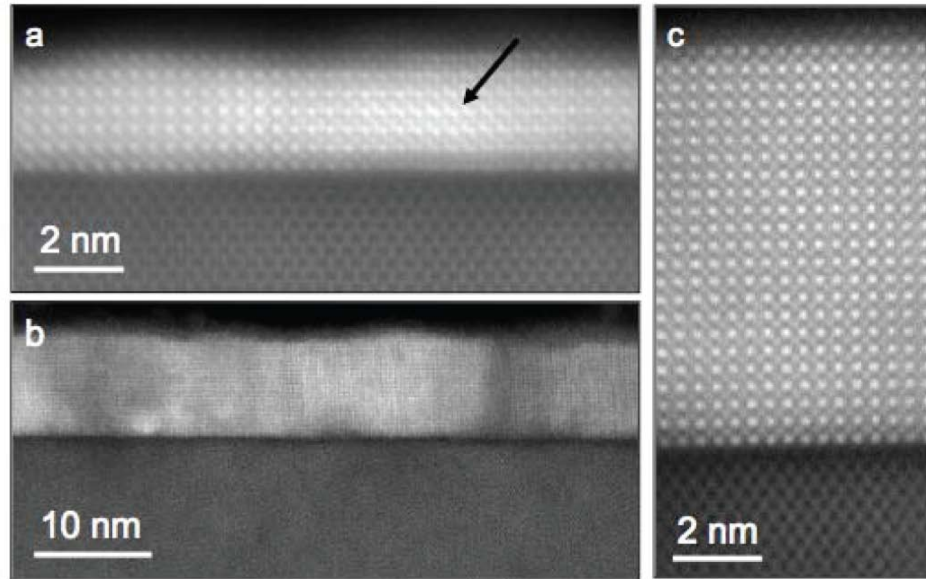

Figure 1-7 Cross sectional scanning transmission electron microscope (STEM) images of $SrTiO_3$ films grown on Si, conforming of the absence of a extending interface layer. Adapted from Ref [20].

Direct growth of ferroelectric $SrTiO_3$ films on Si substrates is achieved by MBE using element Sr and Ti sources and molecular oxygen for oxygenation [20] (Fig. 1-7). The Sr and Ti fluxes are carefully calibrated by adjustment during a calibration growth that precedes each actual growth such that characteristic surface reconstructions due to Sr and Ti excess do not appear in RHEED during the growth of thick $SrTiO_3$ films. The native surface oxide of the Si substrate is thermally removed *in situ* prior to film growth via a Sr-assisted deoxidation process. With an oxygen flux, meticulously controlled using a piezoelectrically controlled leak valve, the $SrTiO_3$ film is grown in layers one to few molecular-strata at a time until the desired thickness is reached. Each layer grown involves a controlled sequence of steps, which kinetically suppress the oxidation of the substrate and reduce tendency of the film to form islands.

1.2.4 Applications

One straightforward application of ferroelectric $SrTiO_3$ on Si is ferroelectric field effect transistor (FeFET), which replaces the normal gate oxide layer in traditional MOSFET structure with a ferroelectric layer to achieve non-volatility. Electric polarization in ferroelectric layer can be induced by voltage pulse and then maintained spontaneously. Similar to the case when a constant voltage is applied to the gate in MOSFET, carrier density underneath Si channel will change to screen the bound charge on top, which will modulate the channel conductance as the read out. Ferroelectric random access memory (FeRAM) constructed on the basis of FeFET as a new type of non-volatile memory device offers advantages like low power consumption, faster writing performance and more write-erase cycles.

It was demonstrated that electrically biased atomic force microscope (AFM) probes are able to switch the polarization in ferroelectric $SrTiO_3$ film locally and read out the polarization states in piezo force microscopy mode, which brings the possibility for a probe-based solid state memory device.

$SrTiO_3$/Si is also a great candidate for Si based spintronic devices. The absence of an amorphous barrier and the chemical isolation of Si from ferromagnetic materials that are chemically incompatible with Si could lead to intriguing potential of injecting tunneling spin polarized carriers from above $SrTiO_3$ layer into Si.

2.0 NANOSCALE CONTROL OF AN INTERFACIAL METAL-INSULATOR TRANSITION AT ROOM TEMPERTURE

This Chapter is largely identical to the published paper in Nature Materials [28]. Samples and electrical contacts were prepared by collaborators in Augsburg University. DFT calculations were performed by collaborators in Naval Research Laboratory. Atomic force microscope lithography and transport measurements were carried out by the author at the University of Pittsburgh.

Experimental [2,29-34] and theoretical [35-36] investigations have demonstrated that a quasi-two-dimensional electron gas (q-2DEG) can form at the interface between two insulators: non-polar $SrTiO_3$ and polar $LaTiO_3$[30], $LaAlO_3$[31-33] , $KTaO_3$[2] or $LaVO_3$ [34]. Electronically, the situation is analogous to the q-2DEGs formed in semiconductor heterostructures by modulation doping. $LaAlO_3/SrTiO_3$ heterostructures have been shown recently[7] to exhibit a hysteretic electric field-induced metal-insulator quantum phase transition for $LaAlO_3$ thicknesses of 3 unit cells (uc). Here reports the creation and erasure of nanoscale conducting regions at the interface between two insulating oxides, $LaAlO_3$ and $SrTiO_3$. Using voltages applied by a conducting atomic force microscope (AFM) probe, the buried $LaAlO_3/SrTiO_3$ interface is locally and reversibly switched between insulating and conducting states. Persistent field effects are observed using the AFM probe as a gate. Patterning of conducting lines with widths ~3 nm, as well as arrays of

conducting islands with densities $>10^{14}$ in^{-2}, is demonstrated. The patterned structures are stable for >24 hours at room temperature.

2.1 INTRODUCTION

The success of semiconductors as technological materials is based on three important features: (1) their electrical conductivity can be tuned over a wide range, either by doping or through electric field effects; (2) insulating layers (i.e., SiO_2) can be formed readily, allowing field effect devices to be fabricated; (3) devices can be scaled to nanoscale dimensions. Oxide materials combine many of the important electronic properties of semiconductors[7,37] with additional emergent phenomena, such as interfacial superconductivity[15], strain-driven ferroelectricity[25], interfacial ferromagnetism[11] and colossal magnetoresistance[38].

The discovery of metallic and superconducting interfaces between insulating oxides has led to many subsequent investigations about the origin of this effect, and in particular the role played by oxygen vacancies[39-40]. In samples that are heated to ~800°C in high vacuum (order of 10^{-6} mbar), oxygen defects are created in the $SrTiO_3$ substrates which *n*-dope the material, regardless of the presence of a $LaAlO_3$ layer[2-4,17]. For samples grown under oxygen pressures $\geq 10^{-5}$ mbar, (as in the experiments described here), the interfacial conductance is dominated by the potential profile generated between the $SrTiO_3$/$LaAlO_3$ interface and the top $LaAlO_3$ surface. Thiel et al. found recently that for samples with 3 uc $LaAlO_3$, a bistable metal-insulator transition can be tuned with a voltage applied between the $LaAlO_3$/$SrTiO_3$ interface and the bottom $SrTiO_3$

substrate[7], suggesting a role played by both the polar discontinuity and residual oxygen vacancies in the $SrTiO_3$.

While oxides provide a wealth of opportunities for probing the rich physics of correlated electronic systems, for technological applications it is essential to scale device concepts to nanoscale dimensions. Ferroelectric field effects at ~350 nm scales have been reported for oxide heterostructures[41]. Here presents a technique which can dynamically define at room temperature nanoscale conducting structures at the interface of two insulating oxides, $LaAlO_3$ and $SrTiO_3$, through reversible control of a localized metal-insulator transition. Both isolated and continuous conducting features with length scales well below 5 nm are demonstrated. Strong nonlinear electric field effects are also observed. One possible theoretical explanation for this behavior is suggested in terms of the creation of oxygen vacancies in the topmost $LaAlO_3$ surface.

2.2 SAMPLES INVESITIGATED

The material system investigated here consists of 3 uc of $LaAlO_3$, grown at 770°C in an O_2 pressure of 6×10^{-5} mbar by pulsed laser deposition on a TiO_2-terminated insulating $SrTiO_3$ substrate[7]. The samples were cooled in 400 mbar of O_2 with a 1 hour oxidation step at 600°C. Several samples were prepared under identical conditions and characterized. One of these identical samples was used for the studies described here. All measurements are performed in air at 295 K. The sample is maintained in a dark environment to suppress carrier photoexcitation in $SrTiO_3$ (bandgap ~ 3.2 eV). A set of electrodes, in contact with the interface and spaced $D_0 = 150$ μm apart, is fabricated using the techniques described in Ref. 7.

2.3 EXPERIMENT SET UP AND RESULTS

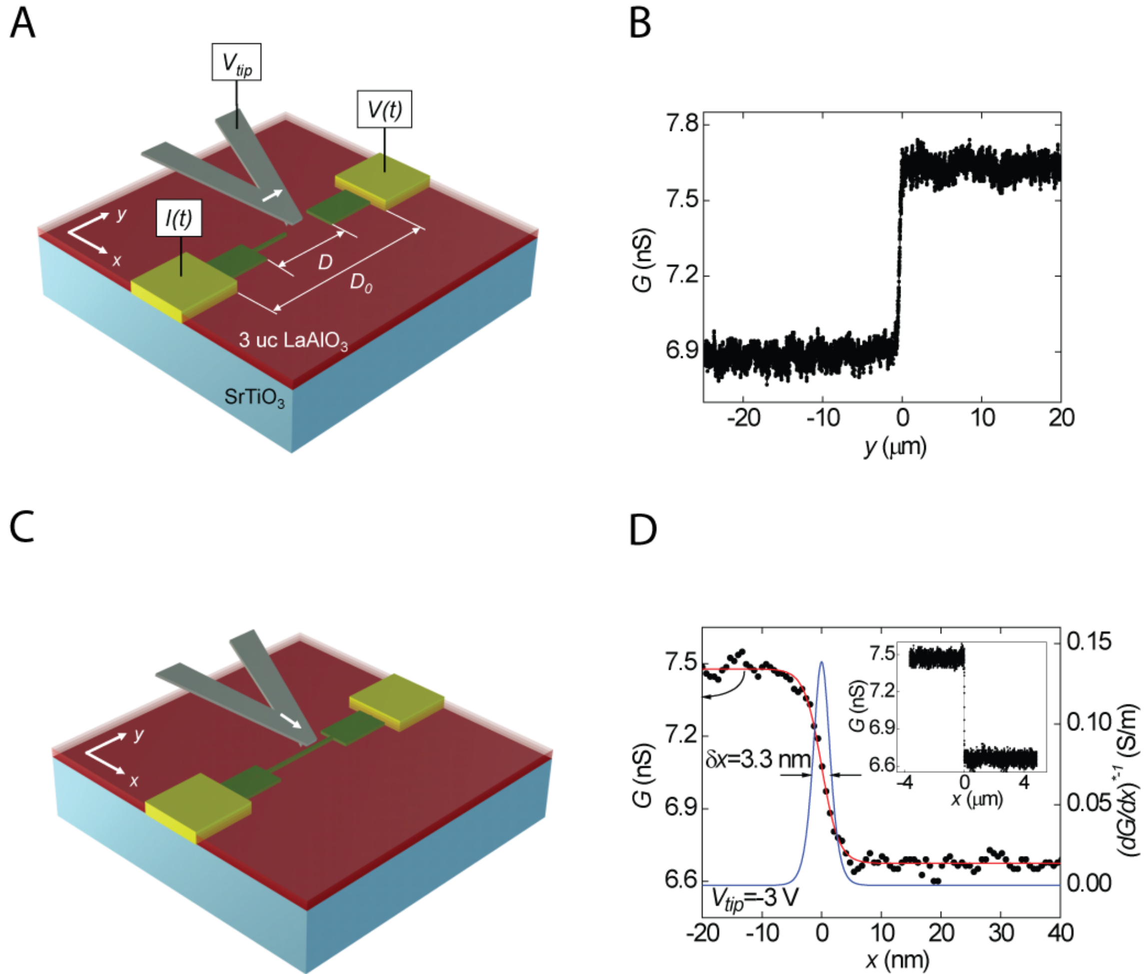

Figure 2-1 Writing and erasing nanowires at the $LaAlO_3/SrTiO_3$ interface. (A) Sketch of the experimental setup for writing a conducting wire. A voltage-biased AFM tip is scanned from one electrode toward a second one in contact mode. The tip generates an electric field that causes a metallic quasi-two-dimensional electron gas to form locally at the interface under the route of the tip. (B) Conductance between the two electrodes measured with a lock-in amplifier as a function of the tip position while writing a conducting wire with 3 V bias applied to the tip. A steep increase in conductance shows when the tip reaches the second electrode. (C) Sketch of the experimental setup for cutting a conducting wire. The negatively biased AFM tip moves in contact mode across the conducting wire. The tip erases the metallic q-2DEG locally when it crosses the conducting wire. The conductance between two electrodes is monitored as the tip scans over the wire. (D) Conductance between the two electrodes measured as a

function of the tip position across the wire, while cutting the wire with the tip biased at -3 V. A sharp drop in conductance occurs when the tip passes the wire. The inset at right shows the conductance measured over the entire 8 μm scan length. The decrease in conductance can be fit to a profile $\sigma(x) = \sigma_0 - \sigma_1 \tanh(x/h)$ with best-fit parameters given by $\sigma_0 = 7.1\ \mathrm{nS}$, $\sigma_1 = 0.40\ \mathrm{nS}$ and $h = 2.9\ \mathrm{nm}$. Also plotted is the deconvolved differential conductance $(d\sigma/dx)^{*-1}$ showing a full width at half maximum $\delta x = 3.3\ \mathrm{nm}$.

A conducting atomic force microscope (AFM) tip, in contact with the top $LaAlO_3$ surface and biased at V_{tip} with respect to the interface, produces an interfacial metallic ($V_{tip} > 0$) or insulating ($V_{tip} < 0$) state directly below the area of contact. Detailed information regarding the mechanism of conductive AFM can be found in Section 10.2.1. Note that V_{tip} is applied between the *top* $LaAlO_3$ surface and the $LaAlO_3/SrTiO_3$ interface; in the experiments of Thiel et al.[7] the voltage was applied between the interface and the *bottom* $SrTiO_3$ substrate surface. For the experiment described below, the gap between the conducting electrodes is first reduced to D=40 μm by "writing" (i.e., raster-scanning at V_{tip}=+10 V) two rectangular pads (Fig. 2-1A). The electric conductance between the two electrodes is monitored using a lock-in amplifier. Without any further writing, there is a measurable background conductance (Fig. 2-1B) which is related to factors such as residual oxygen vacancies in $SrTiO_3$ substrate or a nominal $LaAlO_3$ layer thickness slightly above 3 uc. With more precise control of sample growing process, this conductance background can be suppressed (data presented in Chapter 3-5). The AFM tip, now biased at V_{tip} = +3 V, writes a line by scanning from one electrode to the other. As the tip reaches the second electrode, a pronounced and abrupt conductance increase $\Delta G \approx 0.8$ nS is observed (Fig. 2-1B). This increase is not associated with any observed topographic changes of the structure, nor is it affected by subsequent imaging by an electrically isolated or grounded probe.

To provide a measure of the transverse dimension of the conducting wire, and to demonstrate that the writing process is reversible, the wire is subsequently "cut" with a reverse voltage V_{tip}=−3 V (Fig. 2-1C). As the AFM tip crosses the wire, the conductance decreases abruptly by $\Delta G \approx -0.8$ nS (Fig. 2-1D). Assuming the erasure process to have a resolution comparable to the writing process, the deconvolved differential profile $(d\sigma/dx)^{*-1}$ thus exhibits a full width at half maximum (FWHM) $\delta x = 3.3\text{ nm}$. Subsequent writing with positive voltages over the affected area (e.g., V_{tip}=+3 V) restores the conductance of the wire. The wire width depends sensitively on V_{tip}, increasing by three orders of magnitude as V_{tip} is raised from 3 V to 10 V. Test measurements were performed over a 24-hour interval and showed that the wires remain stable over that time frame.

The written wires are highly sensitive to externally applied electric fields. Figure 2-2A shows the current-voltage (I-V) characteristics of a 20 μm long wire, created with V_{tip}=10 V, that has been perturbed by the AFM probe with varying voltages. The AFM probe functions much like the gate of a ferroelectric field-effect transistor, except that the probe can be scanned. For each curve, the AFM probe is set to a voltage V_{gate} and scanned once across the wire. Afterwards, the in-plane current $I_{||}$ is measured (using a picoammeter referenced to virtual ground) as a function of the voltage V_{sd} applied to one electrode. For low $|V_{gate}|$, the wire conductance is unaffected. However, as the tip bias becomes more negative, the wire becomes insulating and conducts only above a finite bias. This turn-on bias increases monotonically with $|V_{gate}|$. Eventually the I-V curve becomes asymmetric, the likely origin of which is an asymmetry in the insulating barrier profile, produced by unequal electric fields on both sides of the AFM tip.

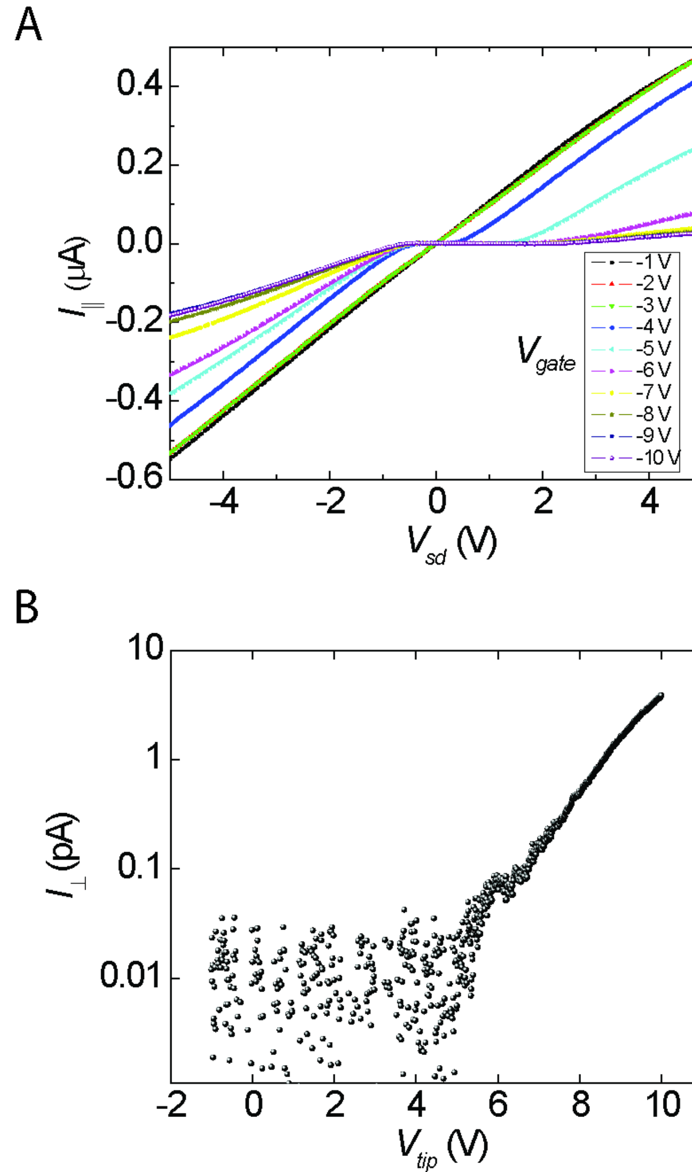

Figure 2-2 Current-voltage characteristics of $LaAlO_3/SrTiO_3$ interface. (A) Current I_{P} versus "source-drain" voltage V_{sd} of a 20 μm long q-2DEG wire with a potential barrier near the center, created with a negative "gate" bias V_{gate}. The barrier is created using the method shown in Fig. 2-1C. Different colors represent different tip biases. When the line is interrupted with a sufficiently large tip bias, the I-V characteristic becomes strongly nonlinear. Conducting behavior is observed at large dc source voltages. (B) AFM tip current $I_{\perp}$ versus tip voltage V_{tip} with respect to grounded interface.

It is also possible to write isolated conducting islands or "dots" by applying voltage pulses $V_{tip}(t)$ with amplitude V_{pulse} and duration t_{pulse} to the tip while keeping the tip at a fixed position. During pulsed writing the two electrodes are grounded. The size of the dots depends on both V_{pulse} and t_{pulse}. For simplicity, V_{pulse} is fixed at 10V and t_{pulse} is varied to change the size of the dots. To determine the effective size of the dots, linear arrays of dots are created with various separations *d* (Fig. 2-3A). After writing the arrays, the ends of the arrays are contacted by writing conducting electrodes, which are separated by *D*=1 μm. As the contacts are being written, the conductance between the two electrodes is monitored using a lock-in amplifier. If the spacing between the dots is greater than the dot diameter, the dots will not overlap and no increase in conductance will be observed. Once the spacing becomes equal to or smaller than the dot diameter, the linear array will form a conducting wire, manifested as an abrupt increase in conductance between the two electrodes (*ΔG*), once the wire is attached. For each pulse duration, a sharp metal-insulator transition is observed as the dot spacing is reduced (Fig. 2-3B). The smallest non-conducting spacing $\underline{d_{nc}}$ and the largest conducting spacing $\overline{d_c}$ are plotted as a function of t_{pulse} (Fig. 2-3C). The critical spacing for conduction d_c is bound by these two measured quantities (i.e., $\underline{d_{nc}} > d_c \geq \overline{d_c}$) and scales linearly with pulse duration until pulse durations $t_{pulse} < 1\ \text{ms}$ are used. Below that threshold, the critical spacing levels off at $\overline{d_c}$ ~1 nm.

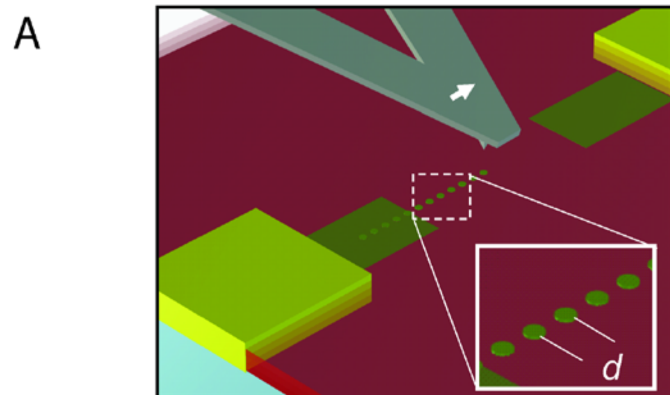
A
d

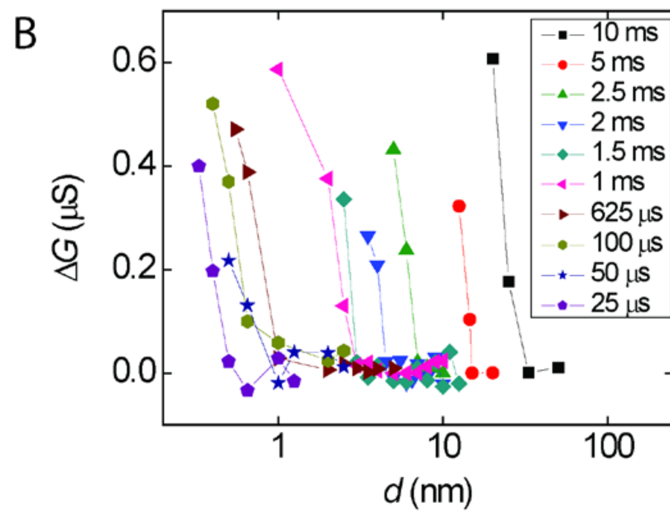
B
0.6
0.4
0.2
0.0
ΔG (μS)
1
10
100
d (nm)
10 ms
5 ms
2.5 ms
2 ms
1.5 ms
1 ms
625 μs
100 μs
50 μs
25 μs

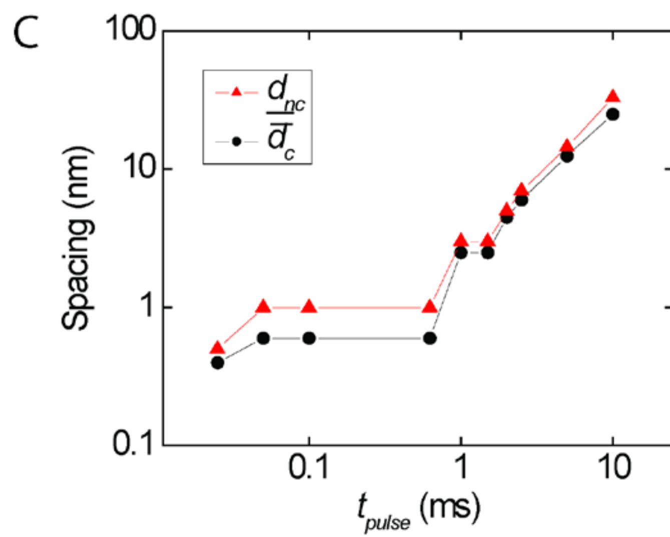
C
100
10
1
0.1
Spacing (nm)
0.1
1
10
t_pulse (ms)
d_nc
d_c

Figure 2-3 Measuring the limits of conducting island density. (A) Schematic showing linear array of dots written with voltage pulses. (B) Conductance change as array is connected to electrodes, for various spacing between dots and different pulse durations. (C) Plot of minimum dot spacing for which the array is non-conducting $\underline{d_{nc}}$ and the maximum dot spacing for which the array is conducting $\overline{d_c}$, presented as a function of pulse duration t_{pulse}.

The exceptionally small size of the features results from the nature of the writing process. The voltage-biased AFM tip produces large local electric fields (E~V_{tip}/L) across the L=1.2 nm thick $LaAlO_3$ barrier. Tunnelling measurements performed between the conducting AFM tip and the $LaAlO_3/SrTiO_3$ interface (Fig. 2-2B) show that for voltages $V_{tip} > V_t$ ~6 V the current $I_\perp$ is governed by Fowler-Nordheim tunnelling between the tip and the interface. Tunnelling takes place over an area the radius of which may be estimated by assuming Hertzian contact[42] to be $r_{contact} = 1.2\text{ nm}$. Writing at voltages smaller than V_t is possible, but not via direct tunnelling. Writing of conducting wires at, e.g., V_{tip}=3 V is only achieved if a conducting path already exists to one of the electrodes (e.g., Fig. 2-1). Isolated conducting regions cannot be written with $V_{tip}<V_t$.

Because there is no strong anisotropy present in the $SrTiO_3$ or $LaAlO_3$, the minimum lateral feature size is expected to be comparable to the scale for vertical confinement of the mobile electrons. Indeed, the smallest dot spacing observed is comparable to the observed thickness $\delta z = 2\text{ nm}$ for the q-2DEG of a closely related system, $LaTiO_3/SrTiO_3$[30]. Using $\delta x = \delta z = 2\text{ nm}$ and l=1 μm, one obtains a resistivity for the wires $\rho = \delta x \delta z / \sigma l = 2\times10^{-3}\,\Omega$-cm , which is close to the Mott-Ioffe-Regel threshold.

$LaAlO_3$ layer thickness	0 uc	2 uc	3 uc	4 uc
Photosensitive?	No	No	Yes	Yes
Background conductance	<10 nS	<10 nS	<10 nS	>1 µS
Write isolated structure?	No	No	Yes	Yes*
Write connected structure?	Not possible without producing damage	Not possible without producing damage	Possible for V_{tip}>3 V	Possible* for V_{tip}>7 V
Topography change after writing	Yes	Yes	No	No
Cut with V_{tip}=-10 V	NA	NA	Yes	Yes*, after several attempts

Table 2-1 Summary of findings for four $LaAlO_3/SrTiO_3$ samples investigated. * For the 4 uc sample, writing and cutting procedures only modulate the conductivity. The interface is always conducting.

Similar experiments are also performed on bare $SrTiO_3$, 2uc $LaAlO_3$ on $SrTiO_3$ and 4uc $LaAlO_3$ on $SrTiO_3$. Experiments show that only in the sample with 3 uc $LaAlO_3$ layer thickness[7] conducting regions can be created and cleared at an insulating interface (Table 2-1).

2.4 MECHANISM DISCUSSIONS

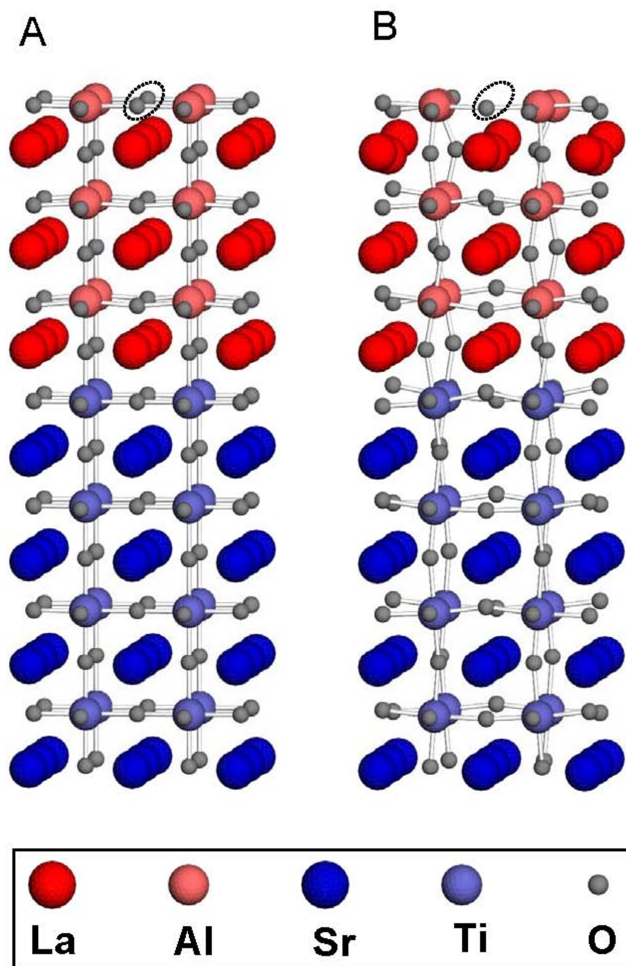

Figure 2-4 Stable structures of a 3 uc $LaAlO_3$ film on $SrTiO_3$. (A) Ideal film with no vacancies and (B) film with one surface oxygen vacancy per 2×2 unit cells. Dashed ovals indicate the row of oxygen atoms with the vacancy in the structure. The oxygen vacancies cause a significant rotation of the oxygen octahedra which propagates into the $SrTiO_3$.

To provide insight into the electronic structure and stability of the metallic and insulating state of $LaAlO_3/SrTiO_3$, collaborators in Navy research lab performed first-principles Density Functional Theory (DFT) calculations of $LaAlO_3$ films on $SrTiO_3$ substrates. These calculations

do not consider possible correlation effects at the interface[35-36]. Computational details are given below. Considering the experiment, an *n*-type (LaO/TiO_2) interface is used. The top surface of the $LaAlO_3$ is assumed to be clean and terminated with an AlO_2 layer. For 3 uc thick films, two structures are predicted to be stable. As shown in Figure 2-4, the two structures differ by the presence of oxygen vacancies on the surface. The two structures are predicted to have dramatically different electrical properties. The "ideal" film without vacancies (Fig. 2-4A) is insulating. Removing oxygen ions from the $LaAlO_3$ surface layer (Fig. 2-4B) accompanies the accumulation of mobile electrons at the interface.

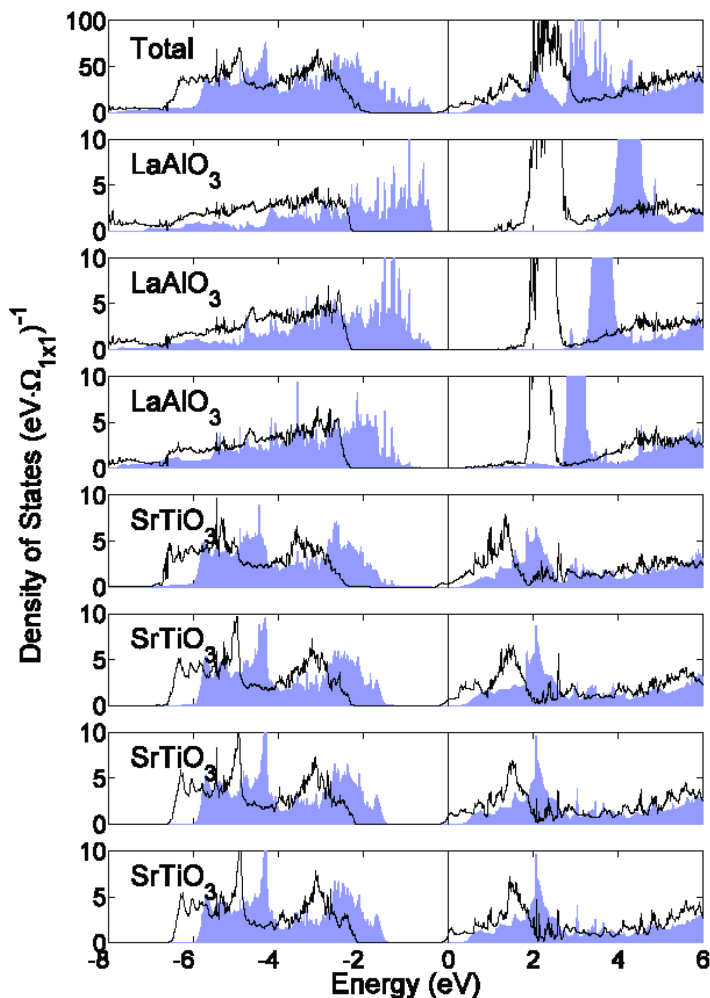

Figure 2-5 Calculated local density of states of $LaAlO_3/SrTiO_3$ for "ideal" and reduced $LaAlO_3$ surfaces for each layer in the 3 uc $LaAlO_3$ film and for the first 4 uc of the $SrTiO_3$ substrate. The solid blue curve corresponds to the "ideal" film, while the black curve corresponds to the film with surface oxygen vacancies. The ideal film is insulating and has a strong electric field in the $LaAlO_3$. With oxygen vacancies in the $LaAlO_3$ surface, the field is compensated, and 0.5 electrons per 1×1 unit cell enter the $SrTiO_3$ conduction states.

The predicted behaviour of the two structures can be understood by examining the local density of states (LDOS), shown in Figure 2-5, and the schematic band diagrams derived from the LDOS (Fig. 2-6). The ideal film has a strong electric field in the $LaAlO_3$, but at 3 uc the

heterostructure is insulating. With one additional $LaAlO_3$ unit cell the system becomes metallic[7]. The strong field is energetically expensive; by including oxygen vacancies at the $LaAlO_3$ surface, it's find that the electric field can be reduced or completely compensated. Such $LaAlO_3$ oxygen vacancies contribute electrons to the conduction band, and the lowest energy conduction band states are in the $SrTiO_3$ (Fig 2-6A). At a density of n_V =1/4 vacancies per 1×1 surface cell, the formal charge of the surface has changed from -1*e* for the ideal AlO_2 surface to -1/2*e* for the $AlO_{1.75}$ surface. The 1/2 electron per unit cell populates the $SrTiO_3$ conduction band on the opposite side of the $LaAlO_3$ film. In this scenario, the oxygen vacancies in the $LaAlO_3$ and conduction electrons of the $SrTiO_3$ together cancel the field in the $LaAlO_3$, as seen in Figure 2-5 and Figure 2-6B. The only metallic region in this system is the $SrTiO_3$ at the $LaAlO_3/SrTiO_3$ interface —the surface remains insulating.

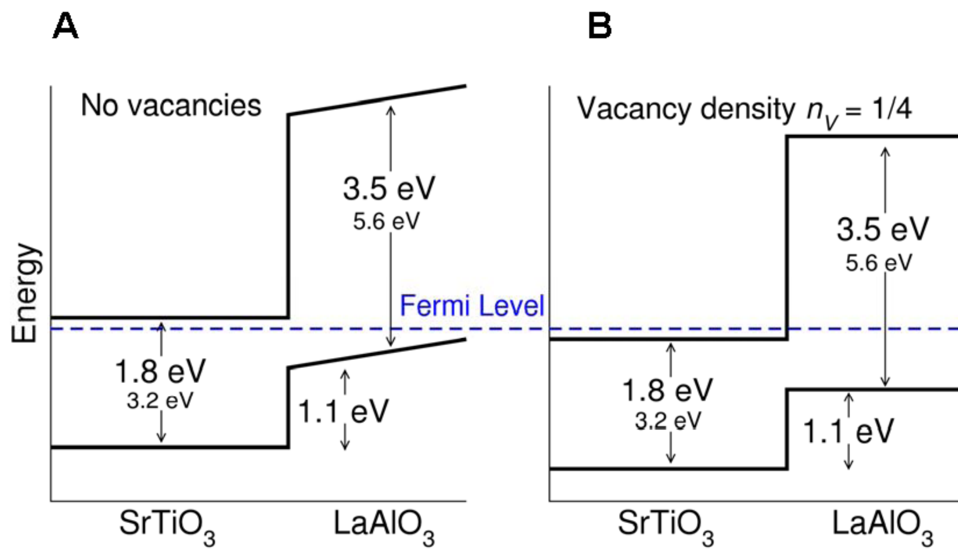

Figure 2-6 Schematic band diagrams of $LaAlO_3/SrTiO_3$ heterostructures. (A)Ideal films without oxygen vacancies. (B) Films with oxygen vacancies (density n_V = 1/4). Computed energy differences are shown in large font. Experimental values (where known) are given in smaller font.

In this model, switching between the two stable structures requires removing oxygen from the $n_V = 0$ surface and adding oxygen to the n_V=1/4 surface. The theoretical calculations described here do not explain how oxygen might be removed or restored to the $LaAlO_3$ surface; they simply predict that a metal-insulator transition will result from this process. There are likely significant kinetic barriers to these processes, which the charged AFM tip may be difficult to overcome. Thus, an alternative model based on similar idea is later proposed, in which interface electric states switch is achieved by selective removal of OH^- or H^+ in the water layer naturally adsorbed at $LaAlO_3$ top surface. Without ruling out other mechanisms such as charging of trap states, this model suggests the possibility that a positively charged AFM tip "writes" metallic wires at the interface by removing OH^-, and a negatively charged AFM tip "erases" metallic regions by removing H^+ and allowing the re-adsorption of another H_2O molecule (Fig. 2-7). Further experimental and theoretical study is required to provide further insight into the physical mechanism that governs this effect.

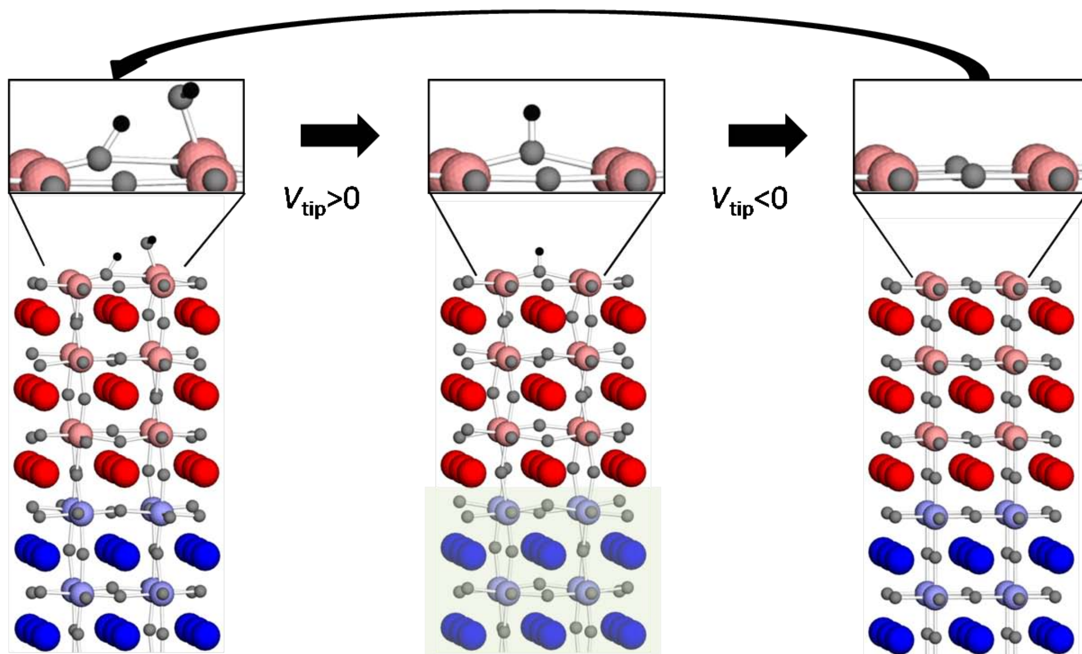

Figure 2-7 "Water cycle" model for the writing and erasing of metallic area at $LaAlO_3/SrTiO_3$ interface. Layers of water molecule will be adsorbed on $LaAlO_3$ top surface when sample is placed in atmosphere. The large binding energy makes the first layer stable even in ultra high vacuum. Positively biased AFM probe removes OH^- and leaves positive charged H^+ ion behind. At interface, metallic electron gas will form to screen the positive charge at top surface. Negatively biased AFM probe removes H^+ allowing a new H_2O molecule to be re-adsorbed and restore the system back to insulating states

2.5 KELVIN PROBE IMAGING

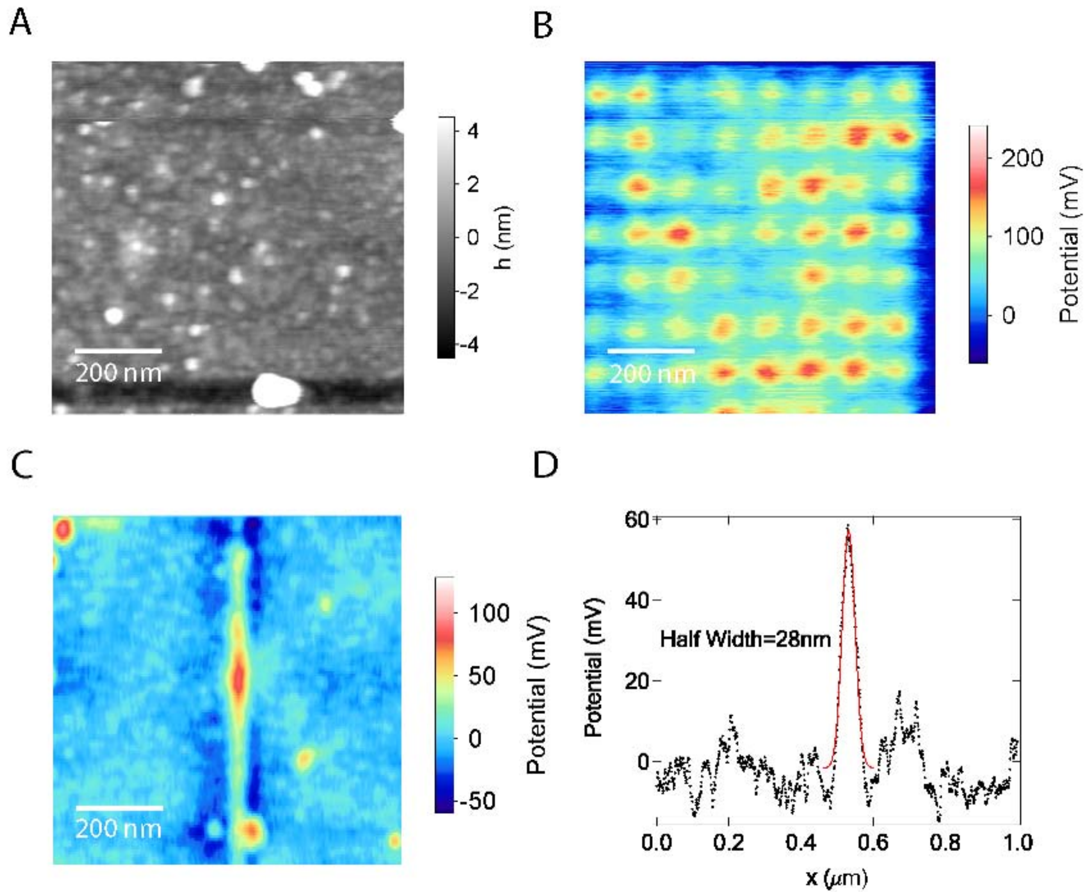

Figure 2-8 Surface potential of interfacial structures measured with Kelvin probe microscopy. (A) Topography of a 1 μm × 1 μm area with dots array written. (B) Surface potential image of the same area. (C) Surface potential image of a 1 μm × 1 μm area with a wire written in the middle. (D) Line cut of (C) showing a wire half width of 28 nm which is limited by AFM probe size.

According to the mechanism proposed above, charge and discharge occurs during the writing and erasing process which is expected to alter the surface potential locally at the top surface of $LaAlO_3$. Therefore, Kelvin probe force microscopy (KFM) is used to image the structures written. Details concerning the operation of KFM is described in Section 10.2.2.

Features of various written structures which are completely invisible in surface topography can be clearly observed in surface potential images (Fig. 2-7). However, KFM fails to measure the real dimension of the interfacial structures due to the resolution limit of this imaging method imposed by the coulomb interaction nature. In the cutting process which is used to measure wire width, the highly nonlinear tunneling process determines that the resolution of measurement is governed only by the contact area with a radius approximately 1.2 nm, while in KFM measurement, the whole radius of curvature of the AFM probe (~20 nm) plays an important role.

2.6 CONCLUSIONS

The ability to pattern reversibly high-mobility electron gases at nanoscale dimensions provides new ground to develop devices for ultrahigh density information storage and processing. Integration with silicon-based devices is possible, as shown by reports of high-quality $SrTiO_3$/Si heterostructures produced by molecular-beam epitaxy [43].

3.0 OXIDE NANOELECTRONICS ON DEMAND

This chapter is largely identical to the published paper in Science [44]. Samples and electrical contacts were prepared by collaborators at the University of Augsburg. AFM lithography and transport measurements were carried out by the author at University of Pittsburgh.

Electronic confinement at nanoscale dimensions remains a central means of science and technology. Here demonstrates nanoscale confinement of a quasi-two-dimensional electron gas at the LaAlO3/SrTiO3 interface and show how it can be exploited to create a variety of electronic devices. Tunnel junctions and field-effect transistors (FETs) with spatial dimensions comparable to single-wall nanotubes are created. The devices can be modified or erased without complex or irreversible lithographic procedures. This new on-demand nanoelectronics platform has the potential for widespread technological application.

3.1 INTRODUCTION

Controlling electronic confinement in the solid state, a key step to numerous scientific and technological advances, becomes increasingly challenging as the dimensionality and scale

are reduced. Bottom-up approaches to nanoelectronics utilize self-assembly and templated synthesis, e.g., junctions between self-assembled molecule layers [45-46] metallic [47] and semiconducting [48] quantum dots, carbon nanotubes [49-50], nanowires [51] and nanocrystals [52]. Top-down approaches strive to retain the lithographic design motif used extensively at micron and sub-micron scales and make use of tools such as electron-beam lithography, atomic-force microscopy (AFM) [53], nanoimprint lithography [54], dip-pen nanolithography [55], and scanning tunneling microscopy [56]. Among the top-down approaches, those which begin from modulation-doped semiconductor heterostructures [57], for example, have led to profound scientific discoveries [58].

The interface between polar and non-polar semiconducting oxides displays remarkable emergent properties reminiscent of modulation-doped semiconductors [1-2,7,30-31,33]. When the thickness of the polar insulator (e.g., $LaAlO_3$) exceeds a critical value, a "polarization catastrophe" induces the formation of a quasi-two-dimensional electron gas (q-2DEG) at the interface joining the two insulators [1,9,15,28-29,31]. In addition to the key role played by the polar discontinuity, there is evidence that, when present, oxygen vacancies in the $SrTiO_3$ also contribute to the formation of the electron gas [2-4,9].

Here focuses on $LaAlO_3/SrTiO_3$ heterostructures, the most extensively investigated system. Due to the large conduction-band offset between $LaAlO_3$ and $SrTiO_3$, the q-2DEG is confined largely within the first few unit cells of $SrTiO_3$ [9,28], with very little penetration into the $LaAlO_3$ layer [59]. Electric fields have been used to control the metal-insulator transition at room temperature [29], and the superconductor-insulator transition at cryogenic temperatures [15]. Further in-plane confinement of the q-2DEG has been achieved by lithographically modulating the

thickness of the crystalline $LaAlO_3$ layer [29]. Control over the metal-insulator transition at <4 nm scales was demonstrated using a conducting AFM probe [28]. This latter method forms the basis for the results reported below.

3.2 SAMPLE INVESTIGATED

The structure investigated here consists of nominally 3.3 unit cells (uc) of $LaAlO_3$, grown by pulsed laser deposition at 780°C in an O_2 pressure of $7.5x10^{-5}$ mbar on a TiO_2-terminated insulating $SrTiO_3$ substrate. After growth, the sample was cooled in 400 mbar of O_2 with a 1 h oxidation step at 600°C. All measurements are carried out in air at 295 K. The sample is maintained in a dark environment to suppress carrier photoexcitation in $SrTiO_3$ (bandgap E_g~3.2 eV).

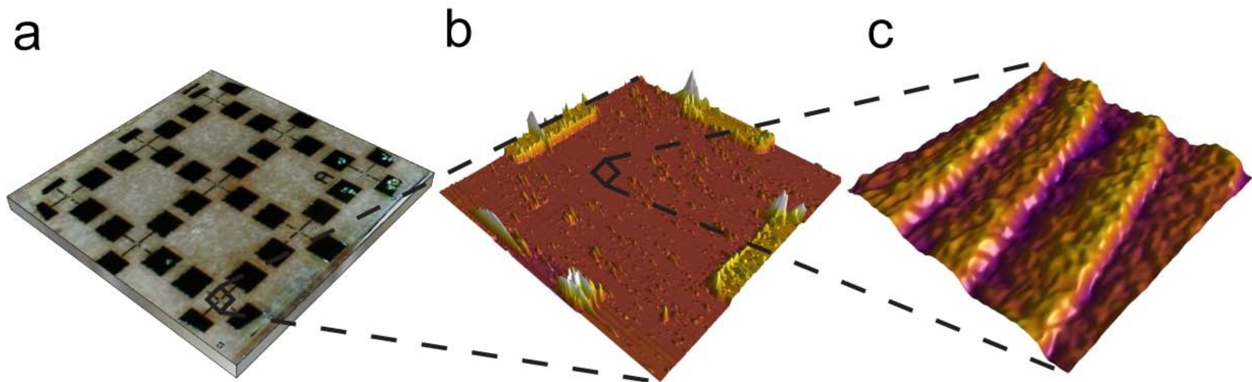

Figure 3-1 (a) 5mm x 5mm optical image of patterned $LaAlO_3/SrTiO_3$ structure with nine electrode sets. (b) 50 μm × 50 μm AFM image showing ends of four Au electrodes and central writable area. (c) 1μm × 1μm AFM image showing (~3Å) terrace structure due to the substrate miscut.

Sets of electrodes, consisting of four gold fingers that connect to macroscopic pads suitable for placing electrical contacts (Fig. 3-1a), form ohmic contacts with the interface due to the Ar-ion etching prior to the gold deposition. Between the ends of the four gold fingers is a 40 μm × 40 μm unetched area (Fig. 3-1b) where the devices are formed. A close-up AFM image (Fig. 3-1c) reveals a terrace structure, resulting from a slight miscut of the $SrTiO_3$ substrate (See Section 10.2 for the topography imaging mechanism of AFM).

3.3 EXPERIMENTS AND RESULTS

Writing and Erasing

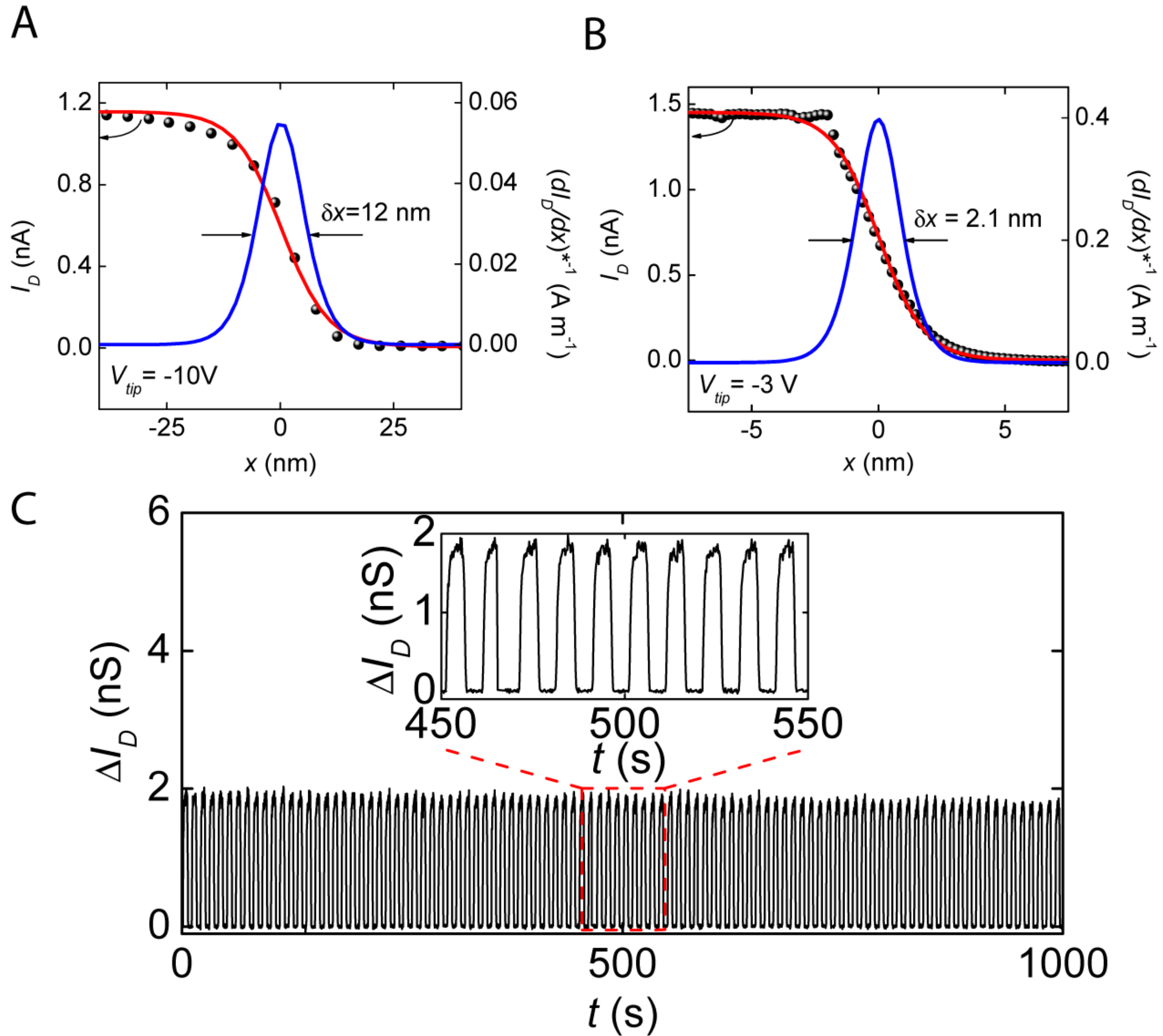

Figure 3-2 For the SketchFET structure, source-drain current measured as a function of the tip position across the wire, while cutting the wire with the tip biased negatively. A sharp drop in conductance occurs when the tip passes the wire. The decrease in conductance can be fit to a profile $I(x)=I_0-I_1\tanh(x/h)$. Also plotted is the deconvolved differential current $(dI/dx)^{*-1}$. (A) Cutting a wider portion of the channel (written with 10 V) with -10 V tip bias, deconvolved differential current shows a full width at half maximum of δx = 12 nm. (B) Cutting narrower portion of

the channel (written with 3 V) with -3 V tip bias, deconvolved differential current shows a full width at half maximum of δx = 2.1 nm. (C) Repeated cutting and restoring of a 12 nm nanowire using V_{tip} = +/-10 V

Based on the experimental finding that nanoscale conducting regions can be created and erased using voltages applied by a conducting AFM probe [28], various multi-terminal devices are constructed (See Section 10.2.1 for detail information about conductive AFM). A conducting AFM tip is scanned along a programmed trajectory (x (t), y (t)) with a voltage V_{tip} (t) applied to the tip. Positive tip voltages above a threshold $V_{tip}>V_t$~2-3 V produce conducting regions at the $LaAlO_3/SrTiO_3$ interface directly below the area of contact. The lateral size δx of this conducting nanoregion increases monotonically with tip bias. Typical values are δx=2.1 nm and δx =12 nm at V_{tip}=+3 V and at +10 V, respectively (Fig. 3-2). Subsequent erasure of the structures can be induced by scanning with a negative voltage or by illuminating with light of photon energy $E>E_g$ [29]. All of the structures described here are written within the same working area; similar structures have been created and measured for other electrode sets, with consistent results.

Designer Potential Barriers

Here demonstrates that the writing and erasing process allows for a remarkable versatility in producing quantum-mechanical tunneling barriers (Fig. 3-3a). The transport properties of these tunnel barriers are investigated in two different experiments. Both begin with w~12 nm wide nanowires written with a positive tip voltage V_{tip}=+10 V. In the first study, a four-terminal transport measurement is performed. A current (I) is sourced from two leads, while a second pair

of sense leads is used to measure the voltage (V) across a L=2 µm section at the middle of the nanowire (Fig. 3-3b). As prepared, the nanowire is well conducting (R_0=147 kΩ, corresponding to a conductivity σ=6.8 µS). This conductivity together with its the aspect ratio a (length/width=160) corresponds to a sheet conductance σ_S= 1.1x10^{-3} S, which is ~100x larger than that of the unstructured film ($\sigma_S^{film} \approx 10^{-5}$ S, [7]).

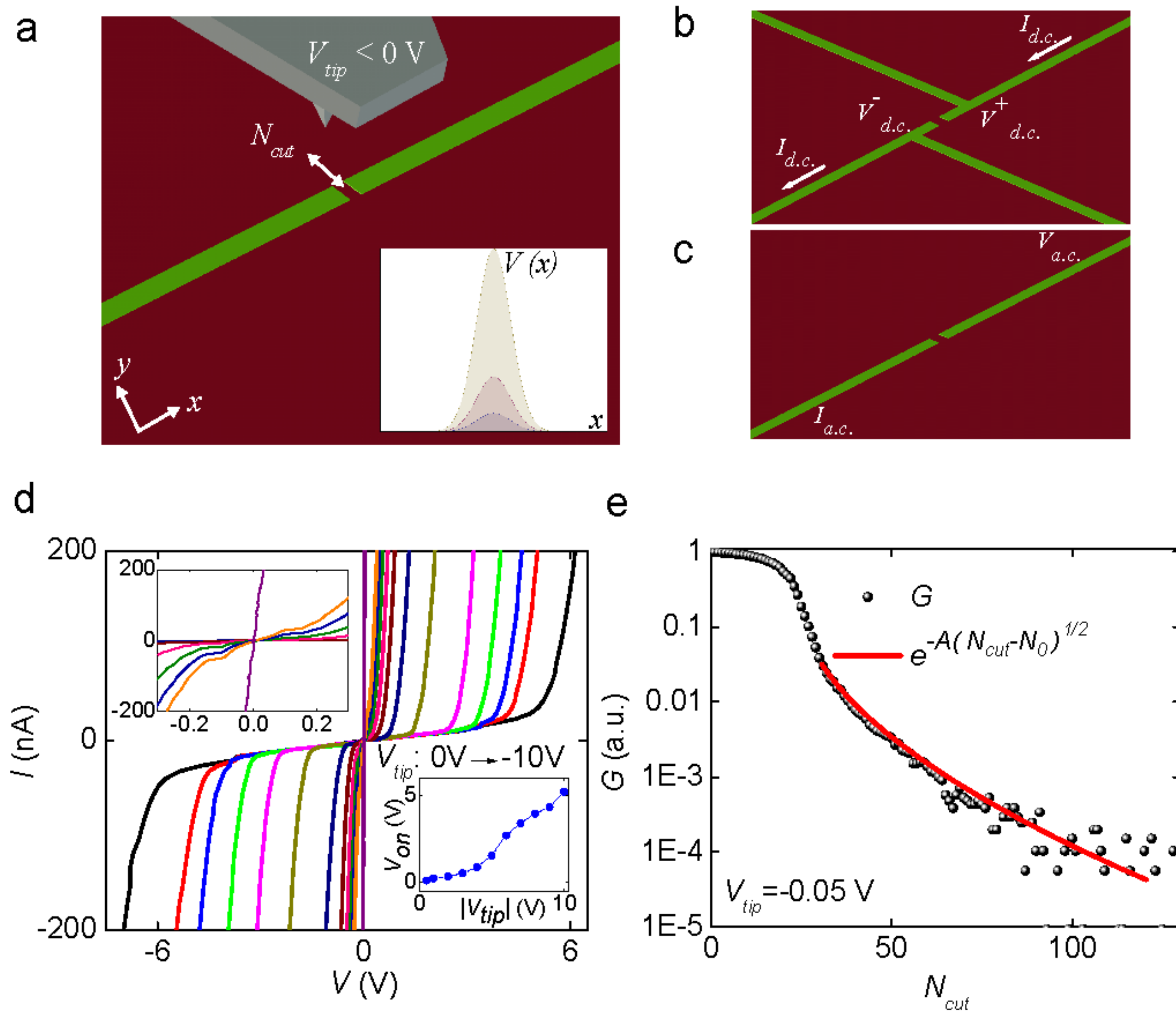

Figure 3-3 Creation of nanoscale tunnel barriers. (a) Sketch illustrating how a potential barrier is created by scanning a negatively biased AFM probe. (Inset (a)) Either increasing the magnitude of negative tip bias (V_{tip}) or scanning across the wire for more times (N_{cut}) with the same tip bias will increase the height of potential barrier. (b)

Illustration of structure used for four-probe measurement (c) Sketch of two-probe a.c. measurement scheme. (d) *I-V* characteristics of a 2 μm long and 12 nm wide uncut wire section and the same section with different potential barrier in the middle created with different negative tip bias (V_{tip}=-0.5 V, -1 V, -2 V, …, -10 V). The upper inset shows the conductance of the uncut wire (slope of the *I-V* curve) to be 6.8 μS. The lower inset shows the turn-on voltage of the nanowire section with a potential barrier as a function of the V_{tip} that is used to create the barrier. (e) Conductance of a 12 nm wide wire with a potential barrier at the middle with V_{tip}=-0.05 V measured as number of cuts N_{cut} increases (i.e., barrier height increases). The red solid line shows a reference curve following typical tunneling behavior $G \propto \exp\left[-A\sqrt{N_{cut}-N_0}\right]$ with best-fit parameters A= 0.99, N_0=17.2.

A negatively biased tip (V_{tip}<0 V) is then scanned across the wire. I-V curves are acquired after each pass of the tip. Scanning with a negative bias restores the insulating state, presumably by shifting the local density of states in the $SrTiO_3$ upward in energy [28], thus providing a barrier to conduction (Fig. 3-3a inset). Hereby, the tip bias starts at V_{tip}=-0.5 V and then increases linearly in absolute numbers (-1 V, -2 V, -3 V,..-10 V). All I-V characteristics are highly nonlinear (Fig. 3-3d), showing vanishing conductance at zero bias, and a turn-on voltage V_{on} (defined as the voltage for which the current exceeds 10 nA) that increases monotonically with tip voltage (lower inset of Fig. 3-3d). A small residual conductance (4.1 nS) is observed which is independent of V_{tip} and hence associated not with the nanowire and tunnel barrier but with an overall parallel background conductance of the heterostructure.

In the second study, the conductance of a nanowire is measured as the AFM tip is scanned repeatedly across the wire with a small fixed negative bias V_{tip}=-50 mV (Fig. 3-3a,b). With each pass of the AFM tip, the conductance decreases monotonically, exhibiting three qualitatively distinct regimes (Fig. 3-3e). For N_{cut}<10, the conductance reduces only slightly

with each pass. For $10<N_{cut}<25$ the behavior transitions to one in which the conductance decays approximately exponentially with N_{cut}. For $N_{cut}>25$, a clear deviation is observed from this straight exponential falloff to one that exponentially decreases as $\exp[-A\,(N_{cut}-N_0)^{1/2}]$, the origin of which is discussed below. Based on these results, I propose the AFM probe is gradually increasing the potential barrier between the nanowire leads [28]. While this process must eventually saturate for large N_{cut}, for the regime explored the potential appears to scale linearly with N_{cut}, as evidenced by the observed dependence of the conductance with N_{cut} over many experiments (Fig. 3-3e). Along the center of the wire, the induced potential after N_{cut} passes is therefore modeled by an effective potential: $V_N\,(x)=V_0+N_{cut}\,V_b\,(x)$ where $V_b\,(x)$ is a sharply peaked (~2 nm-wide) function of position. The conductance of the nanowire measured as a function of N_{cut} (Fig. 3-3e) shows evidence for a crossover from a highly conducting regime ($N_{cut}<10$) to an exponential thermal hopping regime ($10<N_{cut}<25$) to one dominated by quantum-mechanical tunneling through the barrier ($N_{cut}>25$). The latter non-exponential form is consistent with a tunneling probability $t \propto \exp\left[-A'\sqrt{V-E_F}\right]$, as can be seen by a comparison with the functional form $G \propto \exp\left[-A\sqrt{N_{cut}-N_0}\right]$. Based on this dependence it is concluded that the barrier written by the AFM tip acts as a tunnel junction that interrupts the written nanowires.

SketchFET

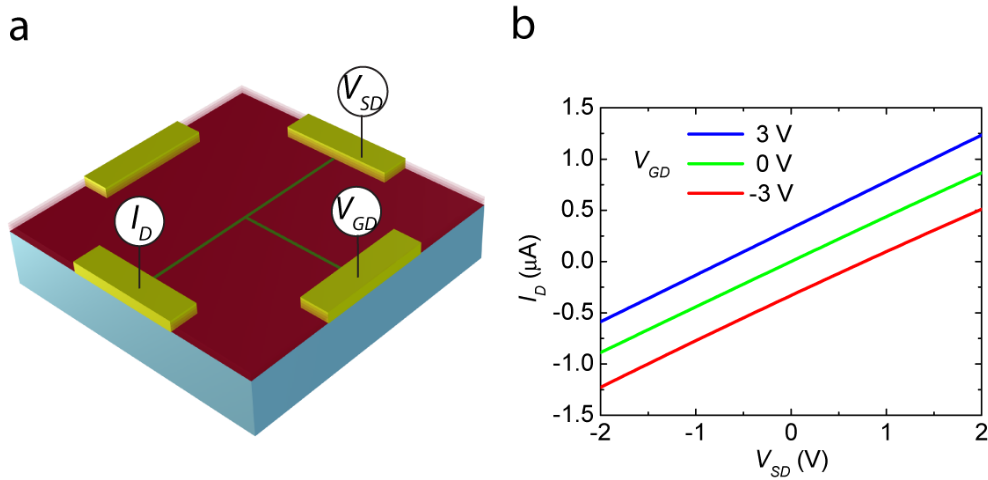

Figure 3-4 T-Junction. (a), I-V characteristic between source and drain (b) at different gate bias (V_{GD}= -3 V, 0 V, 3 V) is all linear. The behavior is well described by a simple resistive network.

The ability to produce ultrathin potential barriers in nanowires allows to create field-effect devices with strongly nonlinear characteristics. Two families of such devices are demonstrated below. Both begin with a "T-junction" of nanowire leads (Fig. 3-4a). The portions of the nanowires that are further than 1 μm from the junction are written with V_{tip}=10 V (w_2~12 nm), while the central region of the junction is written with V_{tip}=3 V, resulting in a narrower conducting channel (w_1~2 nm) (Fig. 3-5a). As constructed, the T-junction behaves as a simple resistive network (Fig. 3-4b).

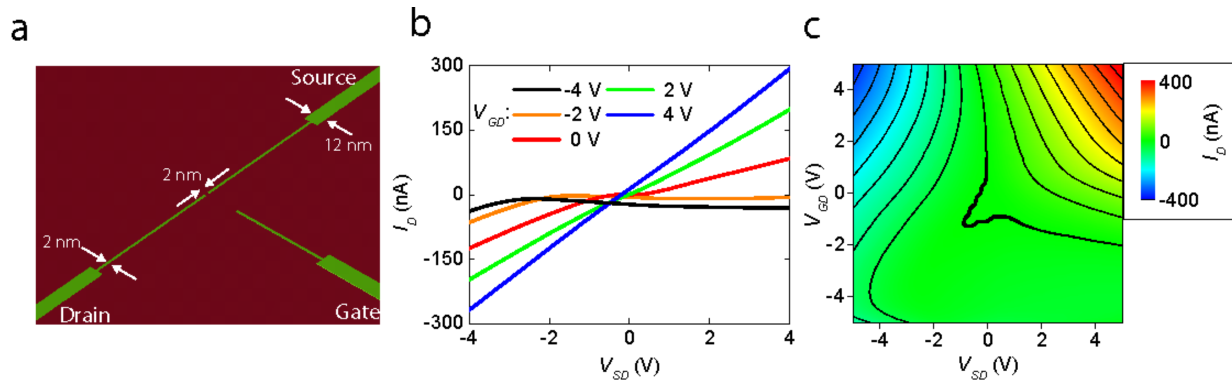

Figure 3-5 SketchFET device. (a) Schematic diagram of SketchFET structure. (b) *I-V* characteristic between source and drain for different gate biases V_{GD}=-4 V,-2 V,0 V,2 V,4 V. (c) Contour plot of I_D (V_{SD} ,V_{GD}). Contours are spaced 50 nA apart.

The creation of the first device (Fig. 3-5a) begins by writing a T-junction of source (S), gate (G) and drain (D) electrodes, followed by a subtractive step in which the AFM probe is scanned under negative bias (V_{tip}=-3 V), starting from the center of the junction and moving a gap distance g_2=50 nm along the direction of the gate electrode. A second writing step with negative bias across the source-drain channel creates a g_1=2 nm barrier. The asymmetry in the two gaps (Fig. 3-6a) enables the gate electrode to modulate the source-drain conductance with minimal gate leakage current. This device is referred to as a Sketch-defined Electronic Transport within a Complex-oxide Heterostructure Field-Effect Transistor (SketchFET).

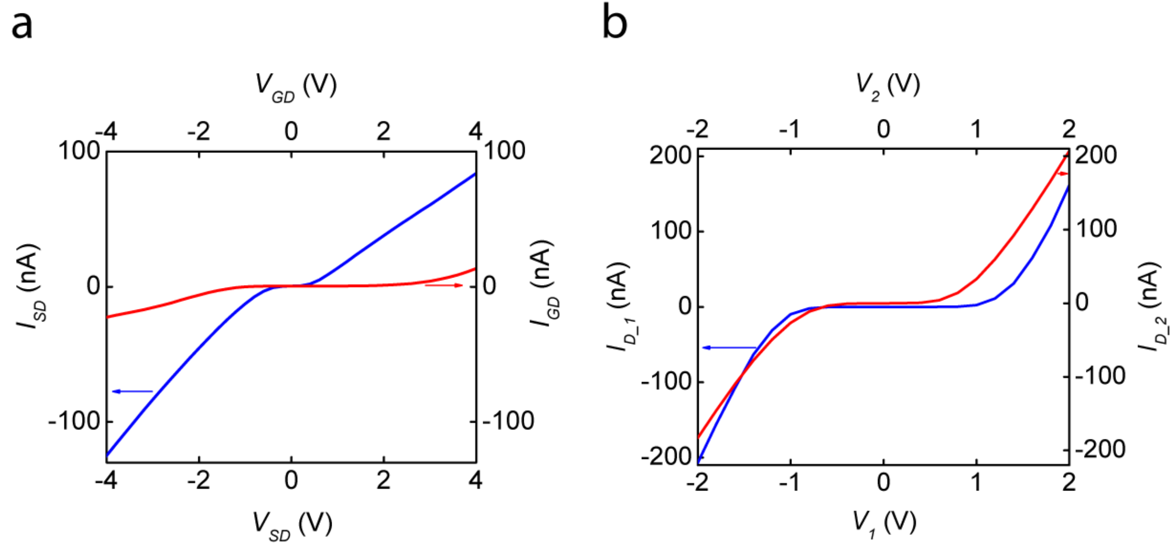

Figure 3-6 (a) For the SketchFET structure, *I-V* characteristic between source and drain (blue curve) is plotted together with I-V characteristic between gate and drain (red curve). (b) For the Double-Tunnel junction structure, *I-V* character between source 1 and drain (blue curve) is plotted together with I-V character between source 2 and drain (red curve).

Transport measurements of this SketchFET are performed by monitoring the drain current I_D as a function of the source and gate voltages (V_{SD} and V_{GD}, respectively). Both V_{SD} and V_{GD} are referenced to the drain, which is held at virtual ground. At zero gate bias, the *I-V* characteristic between source and drain is highly nonlinear and non-conducting at small $|V_{SD}|$ (Fig. 3-5c,b). A positive gate bias V_{GD}>0 lowers the potential barrier for electrons in the source and gate leads. With V_{GD} large enough (>=4V in this specific device), the barrier eventually disappears. In this regime, ohmic behavior between source and drain is observed. This field effect in this case is non-hysteretic, in contrast to field effects induced by the AFM probe [28]. At negative gate biases the nonlinearity is enhanced, and a gate-tunable negative-differential resistance (NDR) is observed for V_{SD} > -2.5 V (Fig. 3-10a). When a sufficiently large gate bias is

applied, a small gate leakage current I_{GD} also contributes to the total drain current I_D (Fig. 3-6a). The NDR regime is associated with this gate leakage current as discussed in more detail below.

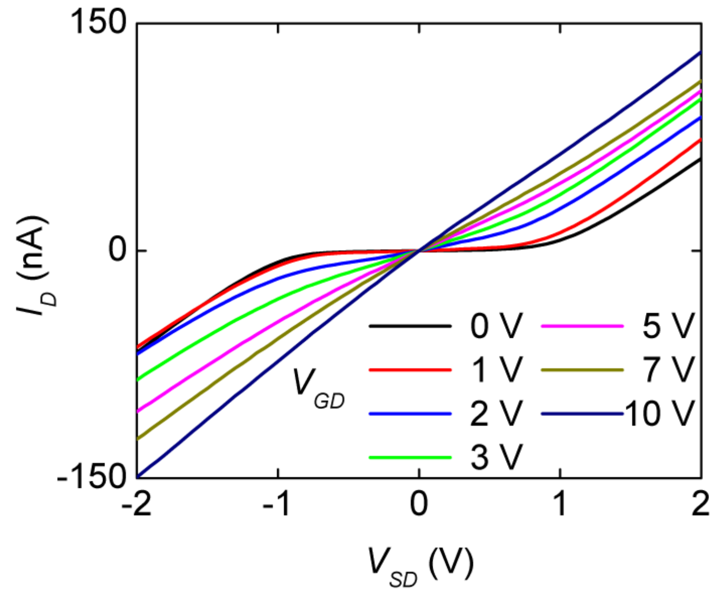

Figure 3-7 I-V characteristics of a SketchFET with a larger barrier. Drain current I_D is plotted as a function of source bias V_{SD} at various gate biases V_{GD}, showing a more pronounced field effect.

By increasing the source-drain gap (g_1=12 nm) of the SketchFET (Fig. 3-7), the source-drain characteristic becomes more symmetric. However, this structure requires a larger positive gate bias to switch the channel on. Tunneling through such a wide barrier width is highly unusual, but it is assisted by the triangular nature of the tunneling barrier under a large applied field (E~MV/cm), and the barrier width is renormalized by the large dielectric constant of $SrTiO_3$ (ε~300 at room temperature).

One of the most important technological applications of FETs are logic elements. The

applied values of V_{SD}, V_{GD} can be interpreted as “on” (>4 V) or “off” (< 4 V) input states of a logic device, the measured values of I_D can be understood as "on" (>200 nA) or "off" (<200 nA) output states. A full exploration of I_D (V_{SD},V_{GD}) reveals an “AND”- functionality (Fig. 3-5c). Due to the nonlinear character of the junction, the resultant drain current when both V_{SD} and V_{GD} are “on” is approximately three times the sum of the individual contributions when only one input is “on”: I_{D} (4V,4V)~3 (I_D (4V, 0V)+I_D (0V,4V)), which yields a promising on-off current ratio.

Frequency response

One gauge of the performance of a transistor is its ability to modulate or amplify signals at high frequencies, as quantified by the cutoff frequency f_T. Characterization of the frequency dependence of the SketchFET described in Figure 3-6 is done using a heterodyne circuit that incorporates the SketchFET as a frequency mixer. The experimental arrangement is shown schematically in Figure 3-8 (a).

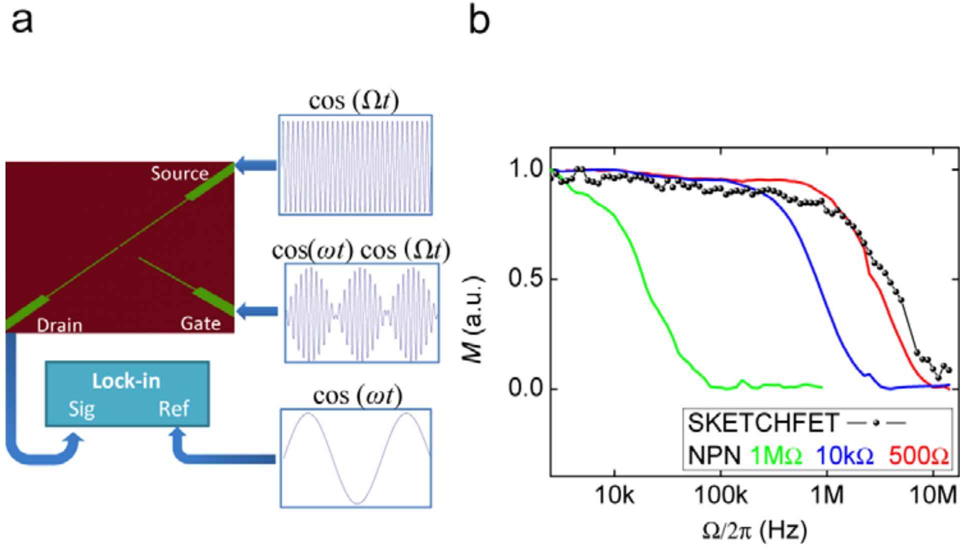

Figure 3-8 (a) Schematic diagram of frequency response measurement. (b) Normalized frequency response of SketchFET and a commercial NPN small signal transistor (cut-off frequency is 900MHz) with no external resistor and resistor of 500 Ω, 10 k Ω, 1M Ω connected in series with the emitter.

A small-amplitude (V_{S0} ~ 100 mV) sinusoidal bias signal $V_S(t)=V_{S0}\cos(\Omega t)$ is applied to the source. The gate signal is derived by amplitude modulating at a low frequency: ω/2π =1.248 kHz: $V_G(t) = \cos(\omega t)V_S(t) = V_{S0}(\cos\Omega_+ t + \cos\Omega_- t)$ where $\Omega_\pm = \Omega\pm\omega$. The resulting drain current I_D is measured by a lock-in amplifier at the reference frequency ω/2π. Detection of a non-zero component of I_D at frequency ω/2π arises due to signal mixing by the transistor, i.e., $I_D(t)$~$g(\Omega_+)\cos(\Omega_+ t)\cos(\Omega t) + g(\Omega_-)\cos(\Omega_- t)\cos(\Omega t) + I_{\Omega,\Omega+,\Omega-} = M(\Omega)\cos(\omega t)$ + higher frequency terms. The mixing strength M characterizes the frequency response of the SketchFET.

The results of this heterodyne measurement over a frequency range 3 kHz<Ω/2π<15 MHz show that the SketchFET operates at frequencies in excess of 5 MHz (Fig.

3-8b). The source-gate capacitance can be estimated from the cutoff frequency using $1/f_T = 2\pi R_S\left(C_{SG} + C_{DG}\right)$. By measuring the *I-V* characteristic of a T-junction with 12 nm wide lead of same size as SketchFET (Fig. 3-4), typical value of the lead resistance is estimated to be R_S =1MΩ, together with f_T =5 MHz , and obtain $C_{SG} \approx C_{DG} \approx 20\,\text{fF}$.In the measurement setup used, this frequency is most likely limited by the large (~MΩ) resistance of the three leads connecting to the device. For comparison, a commercial NPN small signal transistor (Central Semiconductor Corp. 2N709A) is characterized with various resistances R_e = 500 Ω, 10 kΩ and 1MΩ connected in series with the emitter. This transistor has a specified f_T of 900 MHz and collector-base capacitance C_{cb}^{spec}=3pF. By increasing R_e, f_T drops monotonically (Fig. 3-8b), eventually scaling according to $f_T = (2\pi R_e C_{cb})^{-1}$. When R_e=1MΩ, f_T is 20 kHz, calculated C_{cb}^{meas} = 8 pF in reasonably good agreement with the manufacturer's specifications. The high mobility of the channel and the fact that the *I-V* characteristics are far from saturation in the conducting regime suggest that f_T of the SketchFET, without the large lead resistances, could extend into the GHz regime.

Double Junction

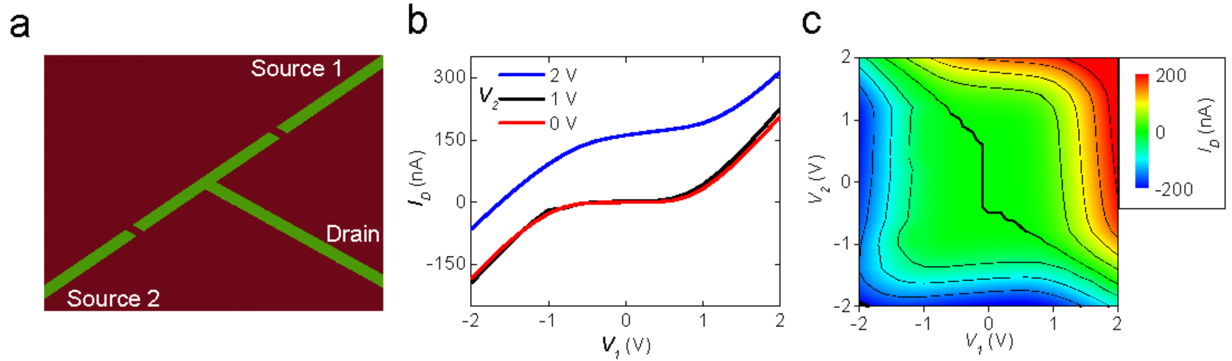

Figure 3-9 Double-Junction device. (a) Schematic diagram of a double junction structure. (b) I-V characteristic between source 1 and drain for three source biases V_2 = 0V, 1V, 2V. (d) Contour plot of I_D (V_1, V_2). Contours are spaced 50 nA apart.

The fabrication of a second family of structures begins by patterning the T-junction described, followed by two erasure steps in which a negatively-biased AFM probe (V_{tip}=-10 V) scans across two of the leads (Fig. 3-9a). The result is a device with two comparable tunneling gaps separated by a distance l from the intersection. (The I-V characteristic of each junction is shown in Figure 3-6b). The electrodes connected by these two sections are labeled V_1 and V_2; the third electrode is labeled as "Drain" (D). Transport experiments to measure I_D (V_1,V_2) are performed using the methods described above. The two tunneling barriers are comparable in their characteristics (Fig. 3-6b). Positive values of V_2 have little effect on the I-V characteristic between V_1 and D (Fig. 3-9b), and vice-versa. Negative values of V_2 can induce NDR in channel between V_1 and D (Fig. 3-10b), which will be discussed later. A full exploration of I_D (V_1,V_2) reveals an "OR"- functionality (Fig. 3-9c) which is not surprising given the topology of the junctions. This structure is referred as a "Double Junction".

Negative differential resistance

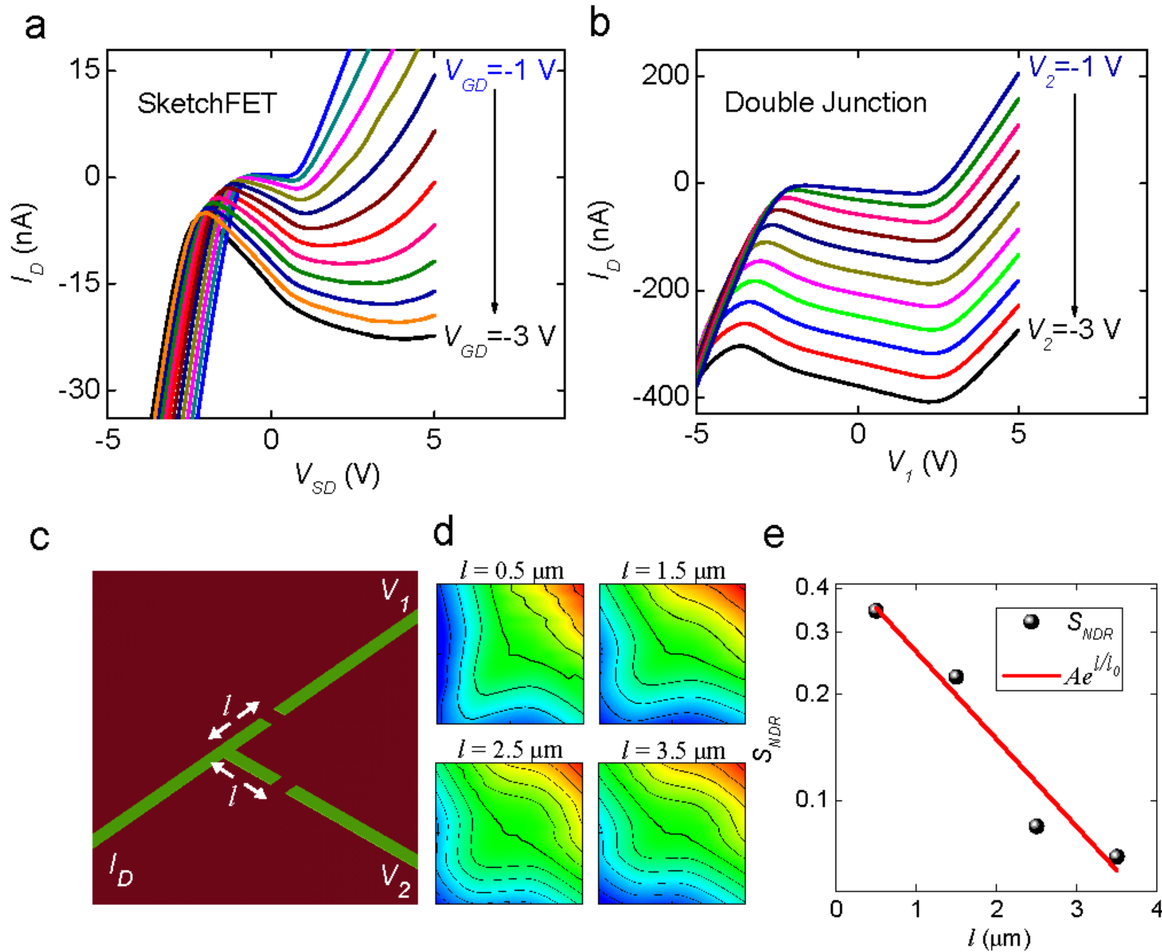

Figure 3-10 Negative Differential Resistance (NDR). (a) NDR observed in SketchFET structure. Gate bias V_{GD} ranges from -1 V to -3 V with steps of -0.2 V. (b) NDR observed in Double-Junction structure with a junction separation of l=5 μm. Source bias V_2 ranges from -1 V to -3 V with steps of -0.2 V. (c) Schematic of a structure of two perpendicular junctions with a distance l from the junction. (d) For structure with l= 0.5 μm, 1.5 μm, 2.5 μm, 3.5 μm, Drain current I_D plotted as V_1 and V_2 is varied from -2 V to 2 V. Contours are spaced 100 nA apart. (e) NDR strength ($S_{NDR} = \max\left(-\left(\partial I_D / dV_1\right)/\left(\partial I_D / dV_2\right)\right)$), equivalent to largest contour line slope) plotted as a function of l (black dot) fitted with exponential decay function A exp $(-l/l_0)$, with best-fit parameters A=0.47, l_0=1.75 μm

A qualitative explanation of the SketchFET NDR originates from the fact that for a three-terminal junction each nanowire exhibits a field effect on the other two. In the range -3 V<V_G<-1 V, the *I*-*V* characteristic between source and gate is nonlinear. When $|V_{SD}|$ is small, conductivity between source and drain is greatly suppressed; I_D is mainly composed of current from the negatively biased gate. Increasing V_S will improve the conductivity between gate and drain and drive more negative gate current to the drain, which manifests itself as NDR. When $|V_{SD}|$ is large enough, the drain current I_D is dominated by current flowing from the source, and the NDR vanishes.

For the Double-Junction structure, the origin of the NDR is less straightforward. To study the nature of the coupling, a family of Double-Junction structures is created and characterized for various distances l from center of the T-intersection, as defined in Figure 3-10c. Normalized magnitude of NDR is quantified as $-(\partial I_D / dV_1)/(\partial I_D / dV_2)$, which can be visualized as the slope of contour lines in 2D plot of I_D (V_1, V_2). Smaller values of l resulted in stronger coupling between the two junctions (Fig. 3-10d), manifested as larger NDR effect. The coupling strength, given by the maximum NDR observed $S_{NDR} = \max\left(-(\partial I_D / dV_1)/(\partial I_D / dV_2)\right)$ is calculated as a function of junction separation (Fig. 3-10e). An approximately exponential decay of this coupling strength is observed, with a fitted decay length l_0 = 1.75 μm.

The long-range coupling of tunnel junctions is consistent with the observation that the sheet conductance of the nanowires is two orders of magnitude larger than for unpatterned

interfaces A possible explanation of where these extra electrons come from, consistent with both observations, is sketched in Figure 4. The writing process is assumed to create positively charged regions (e.g., oxygen vacancies) on the top $LaAlO_3$ surface (Fig. 3-11a) [28]. Directly below, at the $LaAlO_3/SrTiO_3$ interface, electrons screen this positive charge (Fig. 3-11b). These electrons can come from two sources: either from the top $LaAlO_3$ surface, or from weakly bound donor states (associated with defects in the $SrTiO_3$) that become ionized over a length scale $\xi \sim \mu m$ (Fig. 3-11c). This screening is a type of *lateral* modulation doping that can produce a significantly higher electron density as compared to planar unpatterned devices and also a lateral potential profile much wider than the real conductive nanowire region. Experiments in which many parallel wires are connected show saturation of the net conductance toward the bulk value, again consistent with this picture of lateral modulation doping.

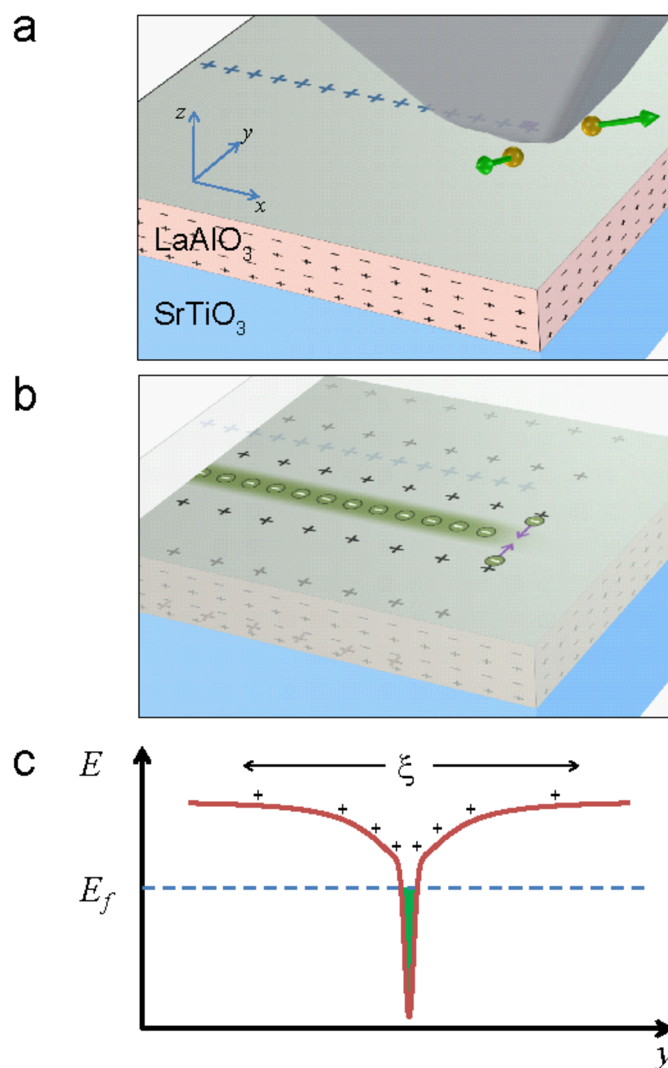

Figure 3-11 Lateral modulation doping of nanowires**.** (a) AFM tip moving left to right above $LaAlO_3/SrTiO_3$ heterostructure, removing oxygen-containing ions and locally changing the charge state of the surface. (b) View of same structure, revealing the conducting nanowire formed at the interface. Electrons screen the surface charges by ionizing nearby states in the $SrTiO_3$ (lateral modulation doping) as well as from the top surface. (c) Illustration of potential profile across the nanowire. Modulation doping occurs over a screening length ξ~µm.

3.4 DISCUSSION AND PERSPECTIVE

The nanoscale structures described above are representative of a new and versatile family of nanoelectronic devices operating at the interface between a polar and non-polar oxide insulator. In addition to the obvious logic and memory applications, the devices demonstrated here suggest many other possible applications which are discussed briefly below.

Nanoscale magnetism and spin resonance. A 2 nm nanowire carrying 100 nA of current will produce an in-plane magnetic field B~10 Gauss at the top surface of the $LaAlO_3$. These magnetic fields are large enough to excite and detect spin waves in nearby magnetic nanostructures, and if the frequency response can be improved it may be possible to sketch current loops around nanoscale samples for nuclear magnetic resonance or electron spin resonance experiments. On-site amplification of these small signals might be possible with SketchFET-based pre-amplifiers.

Nanoscale chemical or electrical sensors. The tunnel junctions at the center of the SketchFETs can be optimized to be sensitive to the charge or oxidation state of the $LaAlO_3$ surface above. The active area is <5 nm^2, allowing for high spatial selectivity for a variety of biological and chemical sensing applications.

Self-referential measurements. The $LaAlO_3/SrTiO_3$ system is sufficiently versatile as to allow basic materials physics questions to be addressed. Previously it was argued [28] that the measured width of written nanowires places a strong constraint over the thickness of the q-2DEG layer. Four-terminal resistance measurements were performed on nanowires by creating

nanowire sense leads. The experiments with Double Junctions provide new quantitative evidence for in-plane modulation doping. Such self-referential measurements will continue to be useful in learning more about this fascinating material system.

Low-dimensional transport. With sufficient control it may be possible to demonstrate single-electron effects such as Coulomb blockade or resonant tunneling, or single-electron transistor behavior, possibly at room temperature. At low temperatures, strongly correlated electron behavior associated with low-dimensionality, i.e., Luttinger liquid behavior, may also be accessible. The discovery and control of superconductivity at the $LaAlO_3/SrTiO_3$ interface provides yet another rich avenue for exploration of mesoscopic superconducting phenomena.

4.0 THERMAL ACTIVATION AND QUANTUM TUNNELING IN A SKETCH-BASED OXIDE NANO TRANSISTOR

This chapter is largely identical to manuscript submitted to Nanoletters. Samples and electrical contacts were prepared by collaborators in Augsburg University. AFM lithography, transport measurements and analyses were carried out by the author at University of Pittsburgh.

Temperature-dependent transport measurements were performed on sketch-defined oxide nanotransistors created at the interface between $LaAlO_3$ and $SrTiO_3$. Analysis of the source-drain current as a function of temperature and gate bias reveals a crossover between thermally activated transport and quantum tunneling. The tunneling current shows two local maxima at T_1=65 K and T_2=25 K, which are associated with structural phase transitions in the $SrTiO_3$ top layer.

4.1 INTRODUCTION

Nanoscale control of the metal-insulator transition in oxide heterostructures [28,44] combines the precision and control of top-down lithographic approaches with the materials quality of bottom-up nanostructures formed by self-assembly. The lithographic technique, which utilizes a conducting atomic force microscope (AFM) probe to define conducting and insulating regions at

the interface between two insulating oxides ($SrTiO_3$ and $LaAlO_3$), is capable of creating nanostructures with near-atomic precision. Recently, a sketch-based transistor (SketchFET) device was created with characteristic dimensions (e.g., channel length) as small as 2 nm (Ref. [44]). In other experiments, tunnel junctions were created and a crossover between thermal hopping and tunneling behavior was observed at room temperature as the barrier height was controlled in a quasi-analog fashion [44]. An understanding of the temperature-dependence of such devices will greatly help to distinguish thermally generated versus tunneling-derived leakage current in transistor devices. Such measurements can also directly measure the energy landscape created by the nanoscale writing process, which can aid in the development of energy-scalable post-CMOS logic elements.

The electronic properties of $LaAlO_3/SrTiO_3$ nanostructures are dominated by the lower-bandgap $SrTiO_3$ layer where the electrons are believed to be localized [1,6-7,9,33,36]. $SrTiO_3$ is intrinsically a "high-k" dielectric. Its relative dielectric permittivity ε is approximately 300 at room temperature, and increases to ~20,000 or more at low temperatures as it approaches (but does not reach) a ferroelectric phase [60-63]. Both epitaxial strain [20,24-25] as well as applied electric fields [61,64-67] can strongly influence the dielectric properties, which in turn can affect the behavior of nanodevices such as the SketchFET.

4.2 EXPERIMENT AND RESULTS

Here describes temperature-dependent transport measurements on a SketchFET device. This structure is created from an oxide heterostructure consisting of 3.3 unit cells of $LaAlO_3$

grown on TiO_2-terminated $SrTiO_3$ substrates. The films were grown at the University of Augsburg by pulsed laser deposition using parameters that are described elsewhere[28,44]. Conducting nanowires are written at the interface between the two oxides using a conducting atomic force (AFM) probe (See Section 10.2.1 for detail information of conductive AFM). When in contact with the top $LaAlO_3$ surface, a positive bias with respect to the semi-insulating interface locally switches the interface to a conducting state, while a negative bias reverts the interface to a semi-insulating state. The writing mechanism is believed to involve metastable charging and discharging of the top $LaAlO_3$ surface induced by the voltage applied between the AFM tip and the $LaAlO_3/SrTiO_3$ interface [68]. In this way, writing and erasing can be regarded as a form of reversible modulation doping using surface dopants that are placed approximately one nanometer from the interface. Nanowires are written by scanning a positively biased AFM tip. Through subsequent erasure with a negatively biased tip, the width of the wires is extracted from tip displacement perpendicular to the channel over which the channel conductance drops[28]. Controllable potential barriers in the middle of nanowires can be created and tuned in a process that is similar to the cutting procedure [44]. The particular SketchFET device discussed here is constructed by three nanowire sections named as "source", "drain" and "gate" (Fig. 4-1A). Each wire is written with tip bias V_{tip}= +10V which has a width approximately 16 nm. A 16-nm wide potential barrier in the channel between source and drain is created with V_{tip}= -10V. The gate lead is oriented perpendicular to the barrier region and is separated from the channel by 50 nm.

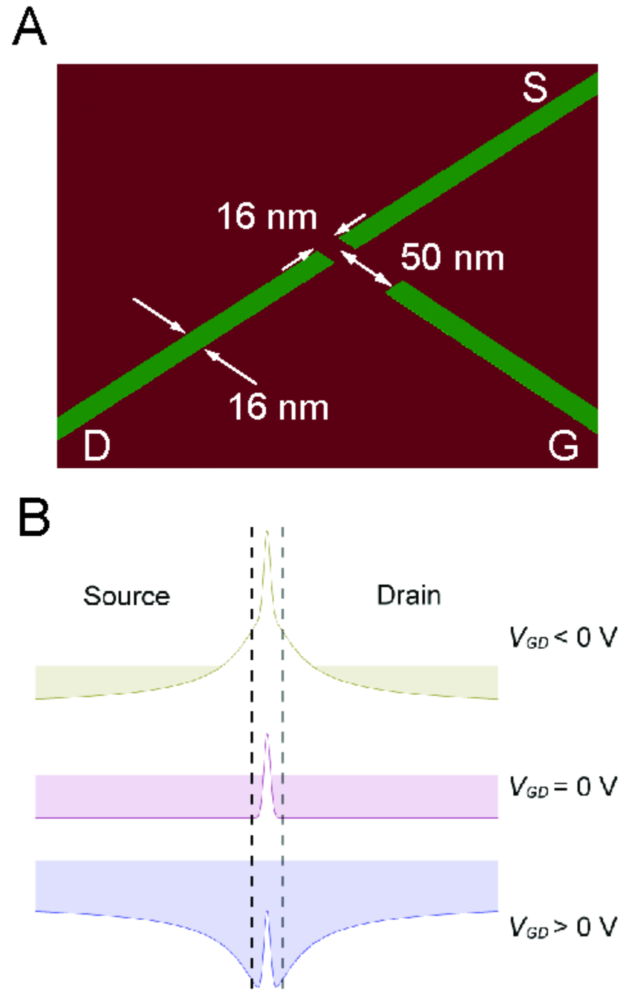

Figure 4-1 (A) Schematic of the SketchFET structure used in the experiment. The SketchFET is composed of three 16 nm wide nanowire sections: source (S), drain (D) and gate (G). The barrier width in the channel between source and drain is 16 nm. The gate is separated from the channel by 50 nm. (B) Schematic of conduction band along the channel between source and drain with a barrier in the middle created by AFM cutting. A positive gate voltage lowers the barrier and increases the conductance in the channel; a negative gate voltage increases the barrier height, lowering the conductance in the channel.

The gate-tuned drain-current I_D as a function of source voltage V_{SD} (I-V characteristics) of the SketchFET was measured at various temperatures ranging from room temperature (295 K)

down to 15 K. Representative curves for three gate biases and three temperatures are shown in Figure 4-2. In general, positive gate biases tend to increase the source-drain conductance while negative biases tend to suppress it. One qualitative interpretation is that the gate electrode is shifting the bottom of conduction band at the barrier region through the Fermi level (Fig. 4-1B) and thereby altering the carrier density as with a standard field-effect transistor. At room temperature, the channel conductance near zero source-drain bias can be tuned by the gate over more than four orders of magnitude. Most of the *I-V* curves are purely odd functions of V_{SD}, indicating that the field-tunable current flux is localized within the channel. At low temperatures and certain negative gate biases, an asymmetric *I-V* profile and slight negative differential resistance is observed (Fig. 4-2 d, g) which is associated with the existence of a small amount of leakage current from the gate lead[44]. At temperatures above 120 K, the drain current decreases monotonically with decreasing temperature.

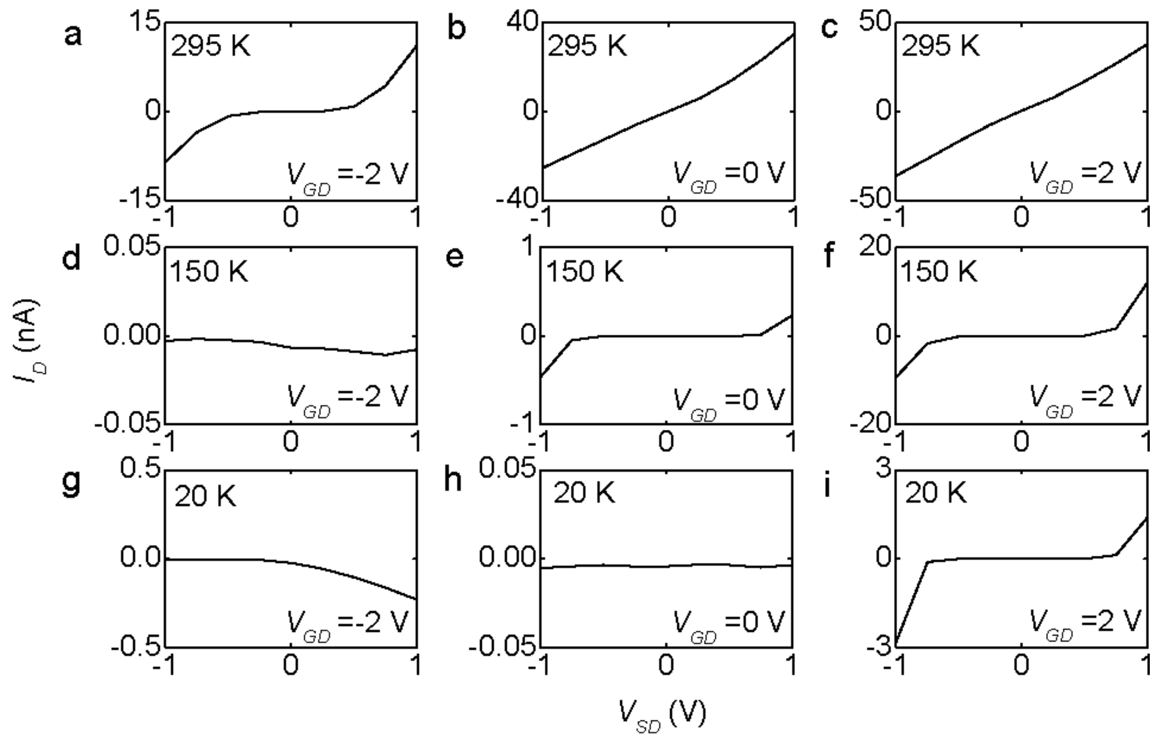

Figure 4-2 *I-V* characteristic of SketchFET at 295 K, 150 K, 20 K with V_G = -2 V, 0 V, 2 V applied.

Since uncut wires written in the same manner show a metallic behavior (resistance decreases with decreasing temperature) (Fig. 4-3), the presence of potential barriers in SketchFET devices plays a dominant role in the decrease of the channel conductance. Figure 4-4A shows an Arrhenius plot of the drain current I_D for various gate and source biases as a function of temperature. The data do not fall on a single straight line as would be the case for thermal activation over a barrier with fixed amplitude. Except for the case V_{GD} = -2 V, for which I_D drops quickly below our instrument's measurable threshold, a kink is observed at around 210 K for all other values of V_{GD}. In the temperature range between room temperature and 220 K, the activation energy E_a (Fig. 4-4B) increases monotonically from 0 eV (V_{GD} = 2 V, V_{SD} =

1 V) to 0.3 eV (V_{GD} = -2 V, V_{SD} = 0.25 V) as V_{GD} and V_{SD} are decreased. These activation energies provide a direct measure of the local barrier region that can be tuned by gate and source voltages at room temperature. With our current device geometry (gate is 50 nm away from channel), such a large local energy difference is too great to be accounted for by straightforward electrostatic coupling. One possible explanation is that electrons are emitted between the gate electrode and the junction region. The emission process leads to a non-equilibrium carrier density which, in addition to the electrostatic fields set up by the gate, source, and drain, contribute to the large tunability measured in SketchFET structures. It's expected that this field emission threshold would depend strongly on the dielectric constant of the surrounding medium (i.e., $SrTiO_3$), and would show anomalies near structural phase transitions where the dielectric constant becomes large.

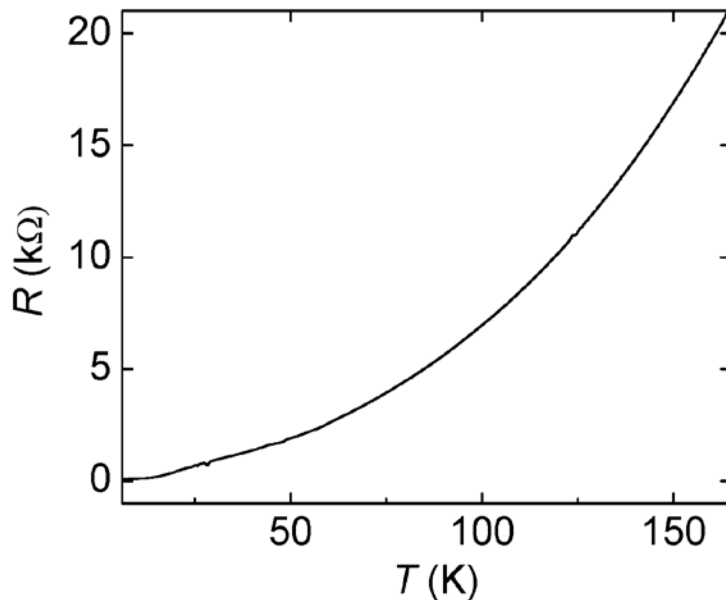

Figure 4-3 Resistance of an uncut wire written with V_{tip} = 10 V as a function of temperature, exhibiting a metallic characteristic.

For temperatures below T=210 K, leakage current from the gate is significantly suppressed, and the activation energy shifts consistently to larger values (Fig. 4-4C), which are believed to be the intrinsic barrier heights without the influence of non-equilibrium carrier population due to field emission from the gate.

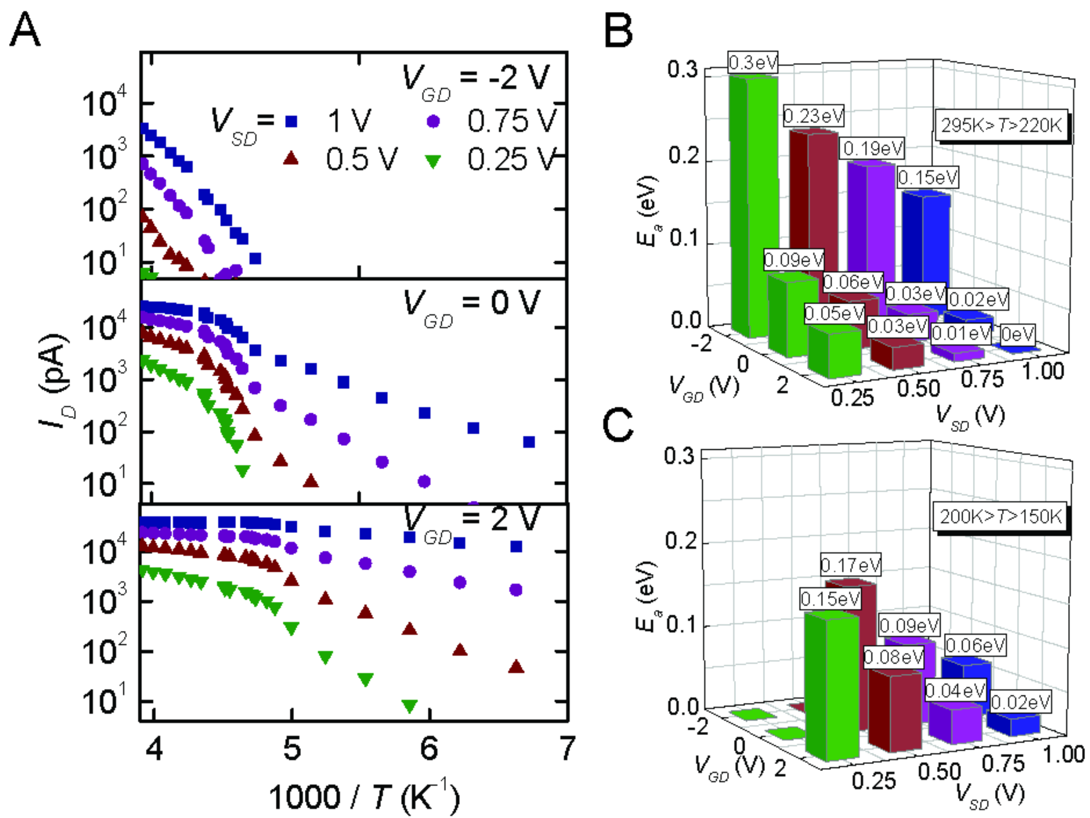

Figure 4-4 (A) Arrhenius plot of drain current as a function of temperature at gate voltage V_{GD} = -2 V, 0 V, 2 V, with source voltage V_{SD} = 1 V, 0.75 V, 0.5 V, 0.25 V applied. (B) Thermal activation energy E_a extracted from data between 220K and 295K. (C) Thermal activation energy E_a extracted from data between 200K and 150K.

Below T=150 K at sufficiently negative gate biases (e.g., when V_{GD} = -2 V), thermally activated conductance between source and drain is negligible, and a small negative leakage current from the gate lead is revealed (Fig. 4-2d, g). Due to the mutual coupling between gate and source, positive source voltages also increase the conductance between gate and drain and thus induce larger amount of negative leakage current into the drain electrode, which manifests a negative differential resistance. A closer examination of drain current at temperature below 150 K reveals that this negative leakage current has two local maxima at around T_1 = 65 K and T_2 = 25 K (Fig. 4-5).

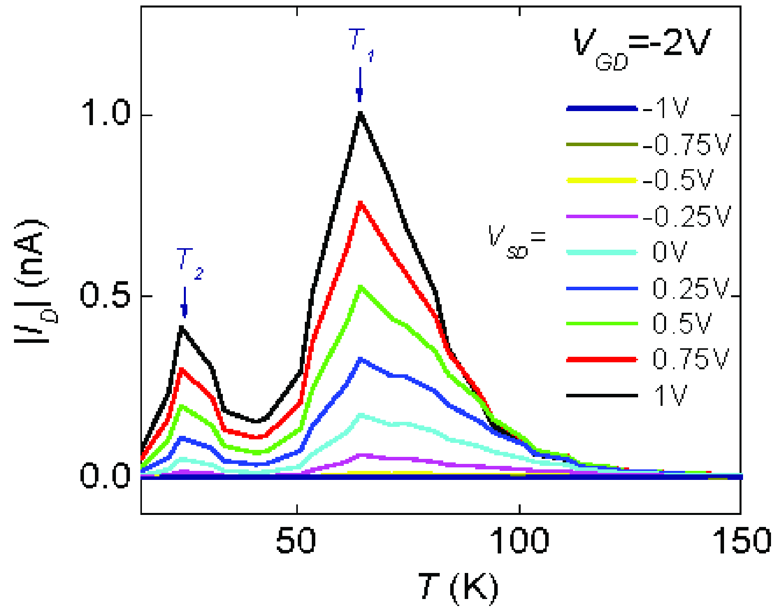

Figure 4-5 Drain current magnitude $|I_D|$ at various source bias measured at temperatures below 150 K when gate voltage V_{GD} = -2 V applied. At low temperature, negative leakage current component in $|I_D|$ coming from gate lead dominates and peaks at T_1 = 65 K and T_2 = 25 K.

I suggest that this low-temperature behavior is related to dielectric constant anomalies occurring at two structural phase transitions in the $SrTiO_3$. Similar structural anomalies have been observed in X-ray diffraction experiment[69] on lattice-mismatched epitaxial films grown on $SrTiO_3$, indicating that, mutual interaction between the $SrTiO_3$ substrate and epitaxial layers can introduce strain and modify the surface structural properties of $SrTiO_3$. At room temperature, $LaAlO_3$ has a lattice constant of a_{LAO} = 3.821 Å which is smaller than the lattice constant of $SrTiO_3$, a_{STO} = 3.905 Å. Strained $SrTiO_3$ is known to undergo multiple phase transitions at low temperatures [20,25]. At transition temperatures T_1 (paraelectric to ferroelastic) and T_2 (ferroelastic to ferroelectric), according to Curie-Weiss law, the dielectric constant diverges:

$$\frac{1}{\varepsilon}=\begin{cases}\dfrac{T-T_C}{C}, & T>T_C\\ 2\dfrac{T_C-T}{C}, & T<T_C\end{cases} \tag{4.1}$$

where T_C is the Curie-Weiss temperature and C is a constant. With such a large dielectric constant, capacitance across the barrier region increases greatly giving rise to much higher carrier density surrounding the barrier and thus modifies the band profile. In this way, the barrier width is effectively shortened and barrier height lowered, which can modify the probability for quantum mechanical tunneling. Noted that asymmetries in the drain leakage current (Fig. 4-5) display a discontinuity in slope magnitude above and below T_c that is consistent with this prediction. A similarly enhanced tunneling effect is also observed between source and drain when the barrier between them is suppressed by large positive gate bias V_{GD} = 2V (Fig. 4-6). In that case, the change in tunneling current is not as pronounced because of the background of thermally activated current. Yet another factor to consider with regard to estimating the magnitude of the tunneling current is the large electric tunability of the dielectric permittivity [25,61,65-66]. Within the nanowire, the confining electric field locally reduces the dielectric constant

in the $SrTiO_3$ compared to the surrounding region. At the phase transition temperature, such a dielectric constant contrast may get significantly larger and improve the mobility of electrons inside the nanowires and thus increase the attempt rate for electron tunneling through the barrier [70]. A full quantitative picture would need to take into account (self-consistently) the sharp variation in the dielectric permittivity within the nanowires themselves.

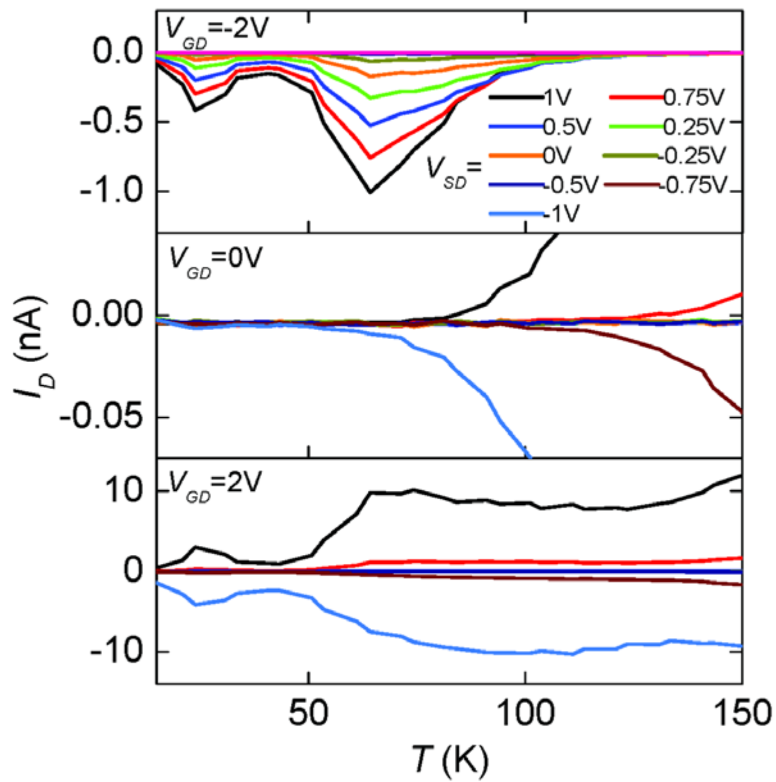

Figure 4-6 At temperatures below 150 K, drain current plotted as a function of temperature for various gate and source biases.

4.3 CONCLUSION

Temperature-dependent transport is measured in a nanotransistor (SketchFET) at the interface of $LaAlO_3$ and $SrTiO_3$ created using a rewritable AFM lithography technique. The SketchFET maintains its transistor functionality down to the lowest temperatures measured, T=15 K. Between room temperature and 150 K, transport in SketchFET is dominated by thermal activation. Changing voltages applied to gate and source electrodes can tune the channel activation energy from 0 to 0.3 eV, which guarantees more than four orders of magnitude on-off ratio in the SketchFET device. Below 150 K, at negative gate bias, thermal activation is suppressed and transport is dominated by quantum mechanical tunneling. Sharp peaks of tunneling current are observed at T= 65 K and 25 K, and are attributed to structural phase transitions in the $SrTiO_3$. This investigation marks the first step in characterizing energy landscape of oxide nanostructures, with implications for the performance of nanodevices at room temperature and at low temperatures.

5.0 OBSERVATION OF POSSIBLE INTEGER AND FRACTIONAL QUANTUM HALL STATES IN AN INTERFACIAL OXIDE NANOSTRUCTURE

$LaAlO_3$/$SrTiO_3$ heterostructures are grown by collaborators in Augsburg University and University of Wisconsin at Madison. Electrical contacts are prepared by Daniela Bogorin and the author at University of Pittsburgh. Magneto transport measurements are performed by Jeremy Levy, the author, Daniela Bogorin and Shan Hu at National High Magnetic Field Laboratory.

The discovery of a high-mobility two-dimensional electron gas at the interface between a polar and non-polar insulating oxide[1] has motivated transport experiments aiming at eliciting various quantum effects. At room temperature, an electric field-tunable hysteretic metal-insulator transition was discovered [7]. At low temperatures (below 1 K), interfacial superconductivity [15] and magnetism [11] were reported. Here describes low-temperature magnetotransport experiments in a nanowire formed [28,44] at the interface between $LaAlO_3$ and $SrTiO_3$. Distinct plateaus are observed and associated with quantized magnetoresistance at integer Landau level filling factors ν=2,3,...,9, and the fractional filling factors ν=7/3 and 11/5. The quasi-one-dimensional nature of the conducting channel, combined with the large electric field-tunable dielectric permittivity of $SrTiO_3$, is believed to contribute to the stability of the integer [71] and fractional [58] quantum Hall states.

5.1 INTRODUCTION

With the invention of the transistor and the discovery of the integer quantum Hall effect (IQHE) [71] and fractional quantum Hall effect (FQHE) [58], semiconductors embody some of the most useful and beautiful physics discovered in condensed matter (See Section 10.4.3 for detail information). For decades, these effects have been observed exclusively within high-mobility silicon or III-V heterostructures. With the maturing of silicon and III-V compound semiconductors for both science and technology, new material systems are being explored. Carbon, both in the form of quasi-one dimensional nanotubes and two-dimensional graphene, has sparked interest both for applications in high-mobility transistors and as hosts for quantized Hall phenomena [72-73].

Wide-bandgap semiconducting oxides have generated a great deal of interest due to high-mobility interfacial electron gases formed in oxide heterostructures with an interfacial polar discontinuity [1,74]. Ohtomo et al. observed [1] signatures of quantum transport in a $LaAlO_3/SrTiO_3$ heterostructure with a Hall mobility $\mu \sim 10^4$ cm^2/Vs. Subsequent experiments on well-oxidized films demonstrated electrically tunable metal-insulator [7] and superconductor-insulator [16] quantum phase transitions. In high magnetic fields, magnetoresistance oscillations have been observed [75] that were neither associated with Shubnikov de Haas nor with quantum Hall phenomena. In higher mobility (μ ~ 5,000-20,000 cm^2/Vs) ZnO-$Mg_xZn_{1-x}O$ heterostructures, Tsukazaki *et al*. observed [74] the integer quantum Hall effect.

The observation of quantum Hall phenomena in a $LaAlO_3/SrTiO_3$ two-dimensional electron gas (2DEG) seems *a priori* precluded by low carrier mobility and high carrier density. For well-oxidized structures [7], the mobility is low ($\mu \sim 10^3$ cm^2/Vs at T = 4 K) and the carrier density high ($n \sim 2\times10^{13}$ cm^{-2}) compared to modulation-doped semiconductor heterostructures. For this carrier density, the $\nu = 1$ quantum Hall plateau is expected to appear at $B_1 = nh/e = 800$ T. Generally, the mobility is expected to decrease monotonically with carrier density n. The metal-insulator transition (MIT) in bulk $SrTiO_3$ occurs at a critical density [76] $n_{MIT} = 2\times10^{12}$ cm^{-2}, which corresponds to a $\nu = 1$ quantum Hall state at a near-inaccessible 80 T. Moreover, it is far from clear that the basic condition for IQHE can be met: $\omega_c \tau_q >> 1$, where $\omega_c = eB/m^*$ is the cyclotron angular frequency, e is the electron charge, m^* is the effective band mass of the electron and τ_q is the quantum lifetime. The low-temperature Hall mobility of well-oxidized $LaAlO_3/SrTiO_3$ heterostructures is four orders of magnitude smaller than for state-of-the-art semiconductor FQHE samples.

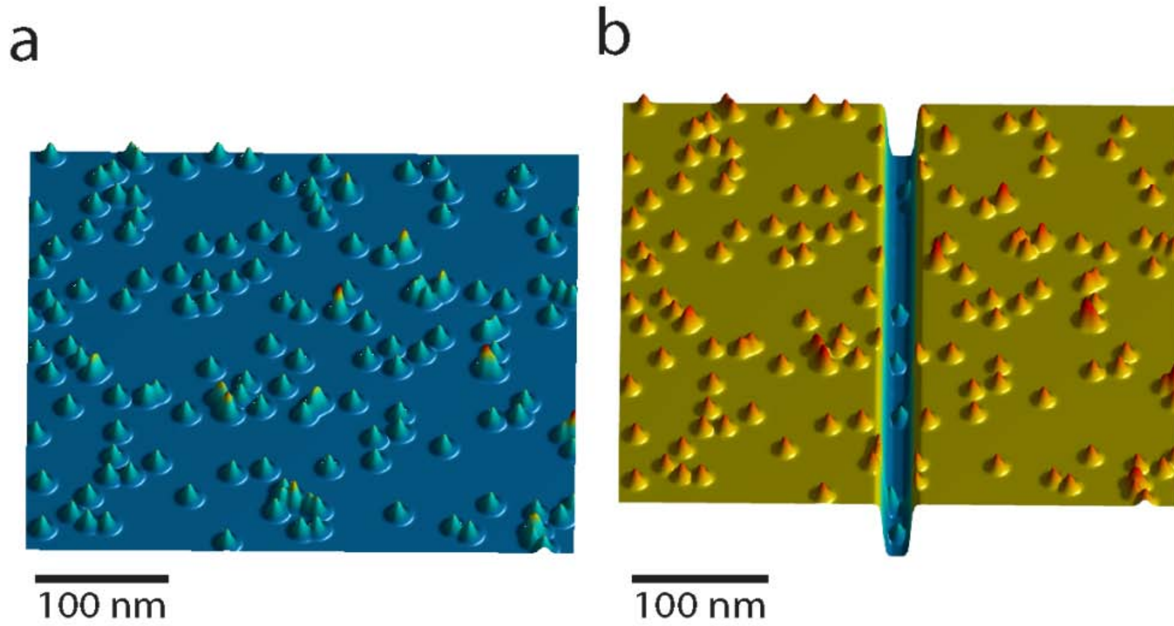

Figure 5-1 Illustration of electron scattering environment in reduced dimensions. **a**, In two dimensions, scattering electrons are subject to elastic scattering from charged impurities. For the sample investigated, impurities are spaced a mean distance $\lambda_{MF} \approx 16\,\text{nm}$. **b**, Strong quasi-one-dimensional confinement within a nanowire greatly reduces the effects of impurity scattering by restricting the path that electrons can take. When the magnetic length becomes comparable to or smaller than the mean-free path, a crossover to coherent quantum transport is observed.

The above arguments rest on the assumption that the samples are homogenous and the transport is two-dimensional (Fig. 5-1a). For nanowires, however, whose width is comparable to or smaller than the spacing between scatterers, transport can be dominated by only a few scattering sites, separated by relatively high-mobility segments (Fig. 5-1b). Dislocations are known to be strong scatterers in the $LaAlO_3/SrTiO_3$ interface [7], and the standard mobility of bulk $SrTiO_3$ is $\mu_{STO} = 2\times10^4\,\text{cm}^2/\text{Vs}$ at low temperatures, which is smaller, yet comparable to the mobility of the first semiconductor FQHE samples. It therefore seems at least possible that the high-mobility sections of lines with a width of some 10 nm may show FQHE states. Nanowires

created at $LaAlO_3/SrTiO_3$ interfaces with critical $LaAlO_3$ thicknesses close to the MIT (~3 unit cells) naturally have lower carrier densities, so that the field strengths required for quantum Hall states become experimentally accessible.

5.2 EXPERIMENT AND RESULTS

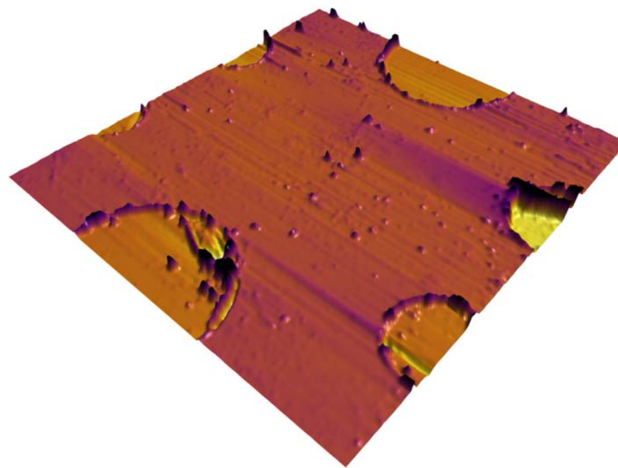

Figure 5-2 AFM image patterned $LaAlO_3/SrTiO_3$ device showing six low-resistance contacts. The image size is 50 μm × 50 μm.

Low-temperature magnetotransport is investigated in nanowires created at the interface between $LaAlO_3$ and $SrTiO_3$. The nanowires, w~14 nm wide, are created using a reversible atomic-force microscope (AFM) writing technique[28] that allows for lateral electrostatic confinement on a much smaller scale than is currently achievable for III-V modulation-doped

structures, approaching one nanometer for quasi-zero-dimensional islands [28] and two nanometers for quasi-one-dimensional wires [44] at room temperature.

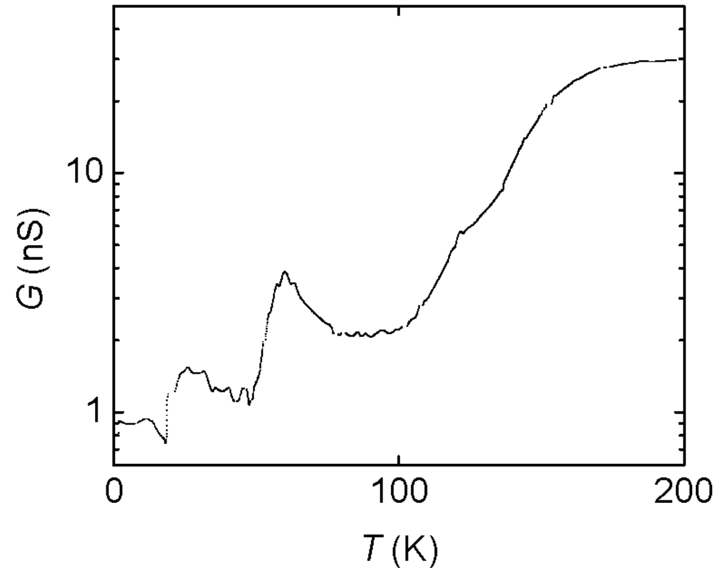

Figure 5-3 Nanowire conductance *G* measured as a function of temperature during cooldown.

Nanowires are formed within a heterostructure containing nominally 3.3 unit cell thick films of $LaAlO_3$ grown epitaxially on a $SrTiO_3$ substrate by pulsed laser deposition [7,28,44]. The sample used is the same one in which nanoscale transistors and other quantum devices were demonstrated at room temperature [44]. Nanowire devices were written on a structure containing low-resistance contacts to the interface spaced as shown in the AFM topographic image (Fig. 5-2). Two such devices were cooled to the base temperature of a ^{3}He refrigerator (250 mK). The conductance of one nanowire (Fig. 5-3) decreased by a factor of ~30, indicating that the wire is in the insulating regime. The conductance of the second nanowire decreased significantly more, falling below the measurement limit. All measurements described below were performed on the nanostructure that did not become completely insulating.

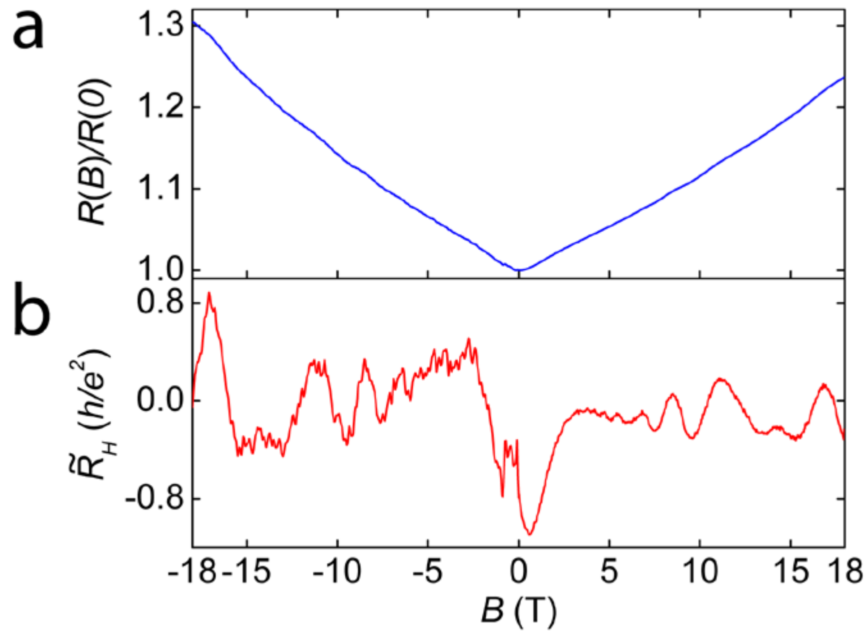

Figure 5-4 Even symmetry of magnetoresistance in nanowire. (a) Normalized nanowire resistance when magnetic field B is swept in positive and negative directions. (b) Same data as (a) but with a second order polynomial subtracted. Data taken for negative magnetic fields is noisier because of a 10x lower voltage excitation and a 3x faster magnetic field sweep rate.

Magnetoresistance measurements were performed on the structure as a function of magnetic field applied perpendicular to the plane of the sample surface (see SOM for details of the measurement methods). The magnetoresistance of the nanowire $R(B)$ is an even function of B (Fig. 5-4) and exhibits three distinct regimes. At low magnetic fields $|B|<0.5$ T (inset, Fig. 5-5a), the magnetoresistance is well described by the relation $R(B) \approx R(0)\left(1+(\mu_0 B)^2\right)$, where $\mu_0 \approx 1050\ \mathrm{cm}^2/\mathrm{Vs}$ is interpreted to be the low-field mobility of the nanowire. For $|B|>0.5$ T, $R(B)$ crosses over to an approximately linear (plus a weak quadratic component) regime. For $|B|>2.5$ T, further, small but distinct departures from this "semiclassical" response are observed.

It's subtract from $R(B)$ a second-order polynomial that describes the background magnetoresistance: $R_C(B)=R(0)\left(1+C_1B+C_2B^2\right)$ where C_1=6.94×10^{-3} T^{-1}, and C_2=1.95×10^{-4} T^{-2} and define $R_H \equiv R-R_C$. The coefficients are obtained by a linear least-squares fit, subject to the constraint $dR_H/dB=0$ at B=18 T. (The constraint $dR_H/dB=0$ embodies the hypothesis that R_H becomes quantized and independent of B in a quantum Hall state; this hypothesis will be explored in more detail below.) Figure 5-5b shows $R_H(B)$ over the range $0\,\mathrm{T}\le B\le 18\,\mathrm{T}$. Distinct plateaus appear at magnetic fields values $B_\nu = B_1/\nu$, where ν=2, 7/3, 3, 4, ... , 9 and B_1=35.2 T, reminiscent of the IQHE[71] and FQHE[58]. Within this interpretation, the carrier density n in the nanowire can be extracted by fitting B_ν with $\nu = hn/eB_\nu$ (Fig. 5-5c,d) where e is the electron charge and h is the Planck constant. The best fit yields $n=8.4\times10^{11}\mathrm{cm}^{-2}$, which is well below the critical carrier density of the superconducting phase of the $LaAlO_3/SrTiO_3$ interface [16] and even for the metal-insulator transition [76] in bulk $SrTiO_3$.

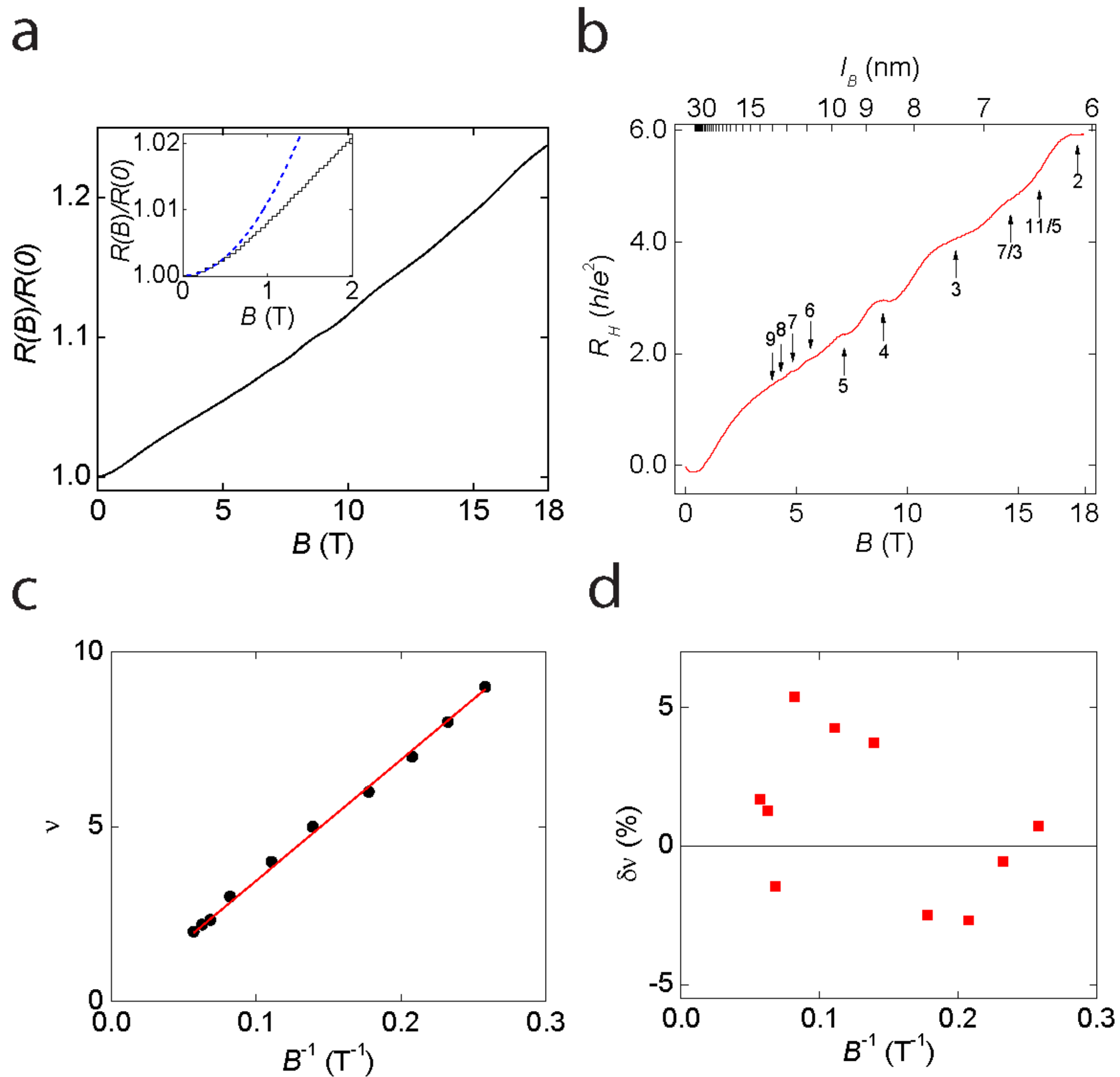

Figure 5-5 Low-temperature (T=0.25 K) magnetoresistance of a nanowire formed at the interface between $LaAlO_3$ and $SrTiO_3$. **a**, Plot of normalized magnetoresistance $R(B)/R(0)$ with R (0) = 3.08 MΩ as a function of out-of-plane magnetic field B. Inset shows a close-up at low magnetic field. The steps visible in the inset are artifacts resulting from the resolution limit of the lock-in amplifier. The blue dashed curve shows the least-squares fit of $R(B)/R(0)$ over the range $|B|<0.5$ T to the form $1+\mu_0^2 B^2$. **b**, Hall contribution $R_H(B)$ to the nanowire resistance (defined in text). The upper scale presents the magnetic length l_B that corresponds to the applied B. As indicated, plateaus are observed at integer and rational fractions of the magnetic field $B_\nu \equiv B_1/\nu$, where $B_1 = 35.2\ \mathrm{T}$ as indicated. **c**,

Plot of ν versus B^{-1} for observed plateaus. Straight line indicates least-squares fit to the form $\nu = B_1 / B$. **d**, Relative error from least-squares fit in **c**.

In order to reveal details, the average linear magnetoresistance is subtracted to obtain a flattened Hall resistance $\tilde{R}_H$. The temperature dependence of $\tilde{R}_H$, taken at T=0.25 K, 0.5 K, 1.0 K, 2.0 K, (Fig. 5-6) shows the effects of thermal activation to higher Landau levels, whose spacing is given by $\hbar\omega_c = \hbar eB / m^*$, where m^* =4.5 m_0 is the heavy electron band mass for $SrTiO_3$ (Ref. [77]) and m_0 is the bare mass. The plateaus associated with fractional filling factors decay much more rapidly with increasing temperature compared to the nearby integer plateaus. This behavior is expected since the energy gap associated with the fractional plateaus is smaller [78-79].

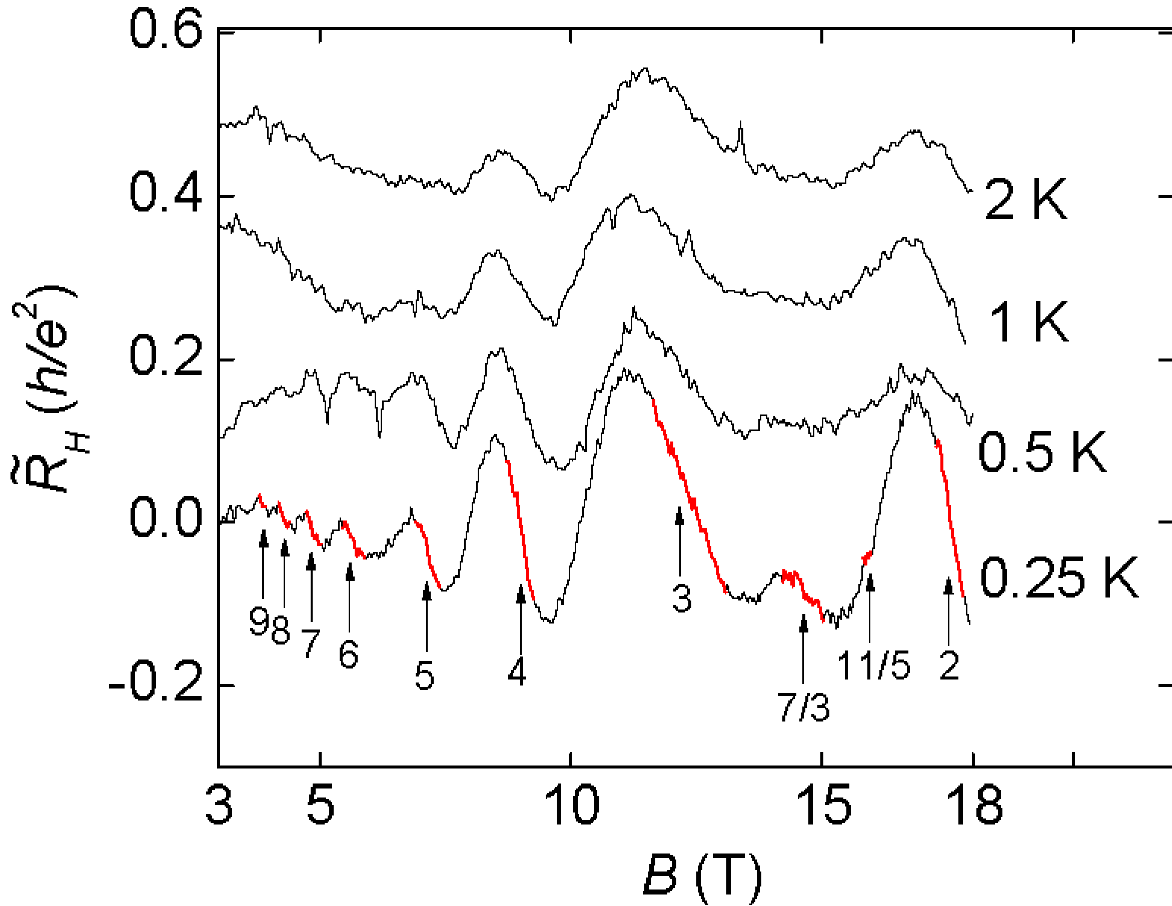

Figure 5-6 Temperature dependence of the magnetoresistance $\tilde{R}_H(B)$ measured at temperatures T = 0.25 K, 0.5 K, 1.0 K, 2.0 K. To obtain $\tilde{R}_H(B)$ a linear fit has been subtracted from $R_H(B)$ to emphasize small features. For the T=0.25 K curve, the parts that correspond to plateaus are highlighted in red. Plateaus corresponding to lower integer values of ν remain visible at higher temperatures. The filling factors 2, 11/5, 7/3, 3, 4, …, 9 are identified with arrows.

5.3 DISCUSSION AND PERSPECTIVE

The main criterion for observing the IQH effect is $\omega_c\tau_q = B\mu_q >> 1$. However, the regime in which both IQH and FQH states are observed corresponds to a regime $B\mu < 1$. Two

mechanisms exist that may explain why $\mu_q >> \mu$. First, quasi-one-dimensional confinement from the nanowire is expected to suppress backscattering [80]. At low temperatures, scattering by phonons is effectively suppressed and scattering is dominated by charged dislocation cores or by ionized impurities. In one dimension, conservation of energy and momentum allow only for elastic scattering in the forward or backward direction. Ionized impurity scattering from impurities outside the nanowire are predicted to decay nearly exponentially with impurity separation d from the nanowire [80]. If an impurity directly intersects the nanowire, it can form a quantum point contact (QPC); otherwise, the scattering effects are greatly suppressed compared to 2D.

A second effect arises from the peculiar dielectric properties of $SrTiO_3$ at low temperature. The large low-temperature permittivity ε~20,000 (Ref. [21]) is highly susceptible to disturbance by doping, electric field or strain. The condition in a nanowire formed at the $LaAlO_3/SrTiO_3$ interface is such that there is a large local electric field (presumably due to positive charges on the top $LaAlO_3$ surface left by the writing process [44]) that is gradually screened self-consistently by the mobile electrons in the nanowire. Within the nanowire, the confining electric field locally reduces the dielectric constant in the $SrTiO_3$ compared to the surrounding. For geometries in which the dielectric constant of the nanowire is significantly less than the surrounding region, Jena et al. [70] predict an order-of-magnitude mobility enhancement in two dimensions, and additional enhancements for one-dimensional geometries.

The geometry of the sample investigated, a 14 nanometer wide line in which the transport is strongly affected by individual scattering centers, differs substantially from the more uniform, two-dimensional samples usually investigated in exploring the quantum Hall effect in III-V

heterostructures. IQH and FQH effects have been reported in narrow quasi-one-dimensional constrictions [81] and in channels where single-mode transport has been verified using the Aharonov-Bohm effect [82].

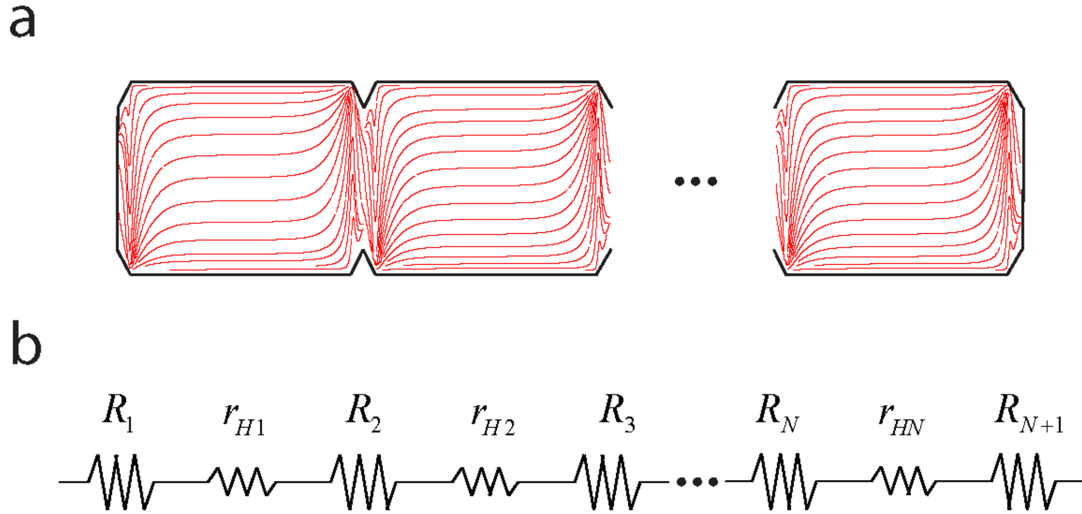

Figure 5-7 Schematic and equivalent-circuit model of nanowire**. a,** Sections with small or even no scattering are bounded by high-impedance quantum point contacts. Red lines indicate current flow along the nanowire. **b,** An equivalent circuit model illustrates how a quantum Hall impedance $r_{Hi} = h/\nu e^2$ is associated with each scatter-free section. The total resistance consists of two terms: $R = R_H + R_C$, where $R_H = \sum r_{Hi}$ exhibits Hall plateaus, and $R_C = \sum R_i$ exhibits a linear magnetoresistance.

To understand the origin of quantized magnetoresistance in the channel investigated, ar a model (Fig. 5-7) is considered in which the nanowire contains N low-impedance sections with resistances $r_{H1},...,r_{HN}$ connected by high-impedance QPCs $R_1,...,R_N$. The low-impedance sections are presumably regions where the linear density of scattering centers is small compared to the magnetic length. the mean free path can be estimated to be $\lambda_{MF} = \mu\hbar k_F / e \approx 16\text{ nm}$ where

$k_F = \sqrt{2\pi n}$ is the Fermi momentum. The crossover to edge-state quantum transport is expected to take place at a magnetic field $B_Q > \hbar / e\lambda_{MF}^2 \approx 2.6\,\mathrm{T}$, at which the probability of multiple back-scattering events between classical skipping orbits becomes low[83]. The QPCs are formed presumably by the charged defects discussed or by fluctuations in the lateral confinement potential that locally alter the carrier density. The model described above is consistent with the Landauer-Buttiker framework, and is equivalent to the circuit model of Ricketts and Kemeny [84] (Fig. 5-8), and similar to a framework developed by Jain et al. [85] to explain FQH phenomena in the experiment by Timp et al [81].

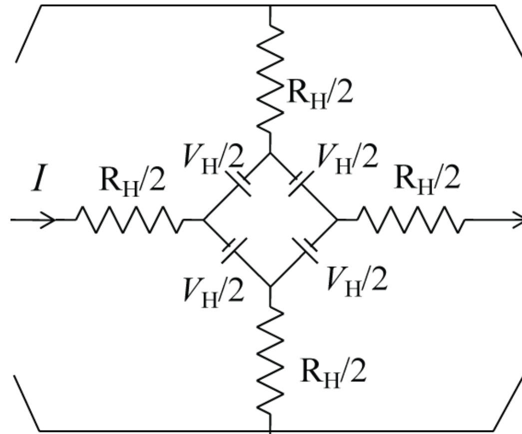

Figure 5-8 Equivalent circuit of a single scatter-free section of the nanowire. The two-terminal magnetoresistance in the quantum Hall state is equal to $R_H = \hbar / \nu e^2$. Adapted from Ref. [84].

When the quantum Hall state is reached, backscattering from associated edge states are suppressed and both the Hall resistance [71] and longitudinal magnetoresistance [86] r_{Hi} become quantized. If define $R_C = \sum_{i=1}^{N+1} R_i$, $R_H = \sum_{i=1}^{N} r_{Hi}$ and $R = R_C + R_H$ then the total two-terminal

magnetoresistance of N segments R_H is expected to be quantized in N multiples of $h/\nu e^2$ as $B \to nh/\nu e$, where allowances are made for variations in carrier density due to the mesoscopic size of the segments. Reading off the value of R_H at the ν=2 plateau, it's find that $N \approx 12 \pm 2$ segments are connected in series, each contributing $h/2e^2$ to the total quantized magnetoresistance. The uncertainty in N originates from the process by which R_C is subtracted. Plateaus at fractional quantum Hall states can be incorporated into this picture using Beenakker's extension[87] of the Landauer-Büttiker model to the FQH regime.

The linear magnetoresistance observed in R_C has been observed [88] in Hall bar devices with top gates that produce inhomogeneous electron density distributions (Fig. 5-7a). Within the Landauer-Büttiker framework, the resistance of the QPC is given by $R = (1/e)\left(n^{-1} - n_{QPC}^{-1}\right)B$, where n_{QPC} is the reduced density at the QPC. Using this expression the average carrier density in a given QPC can be estimated: $n_{QPC} = Nn/(N + neC_1R(0)) \approx 2.5 \times 10^{11}\,\mathrm{cm}^{-2}$, which is approximately three times smaller than the carrier density n derived from B_ν.

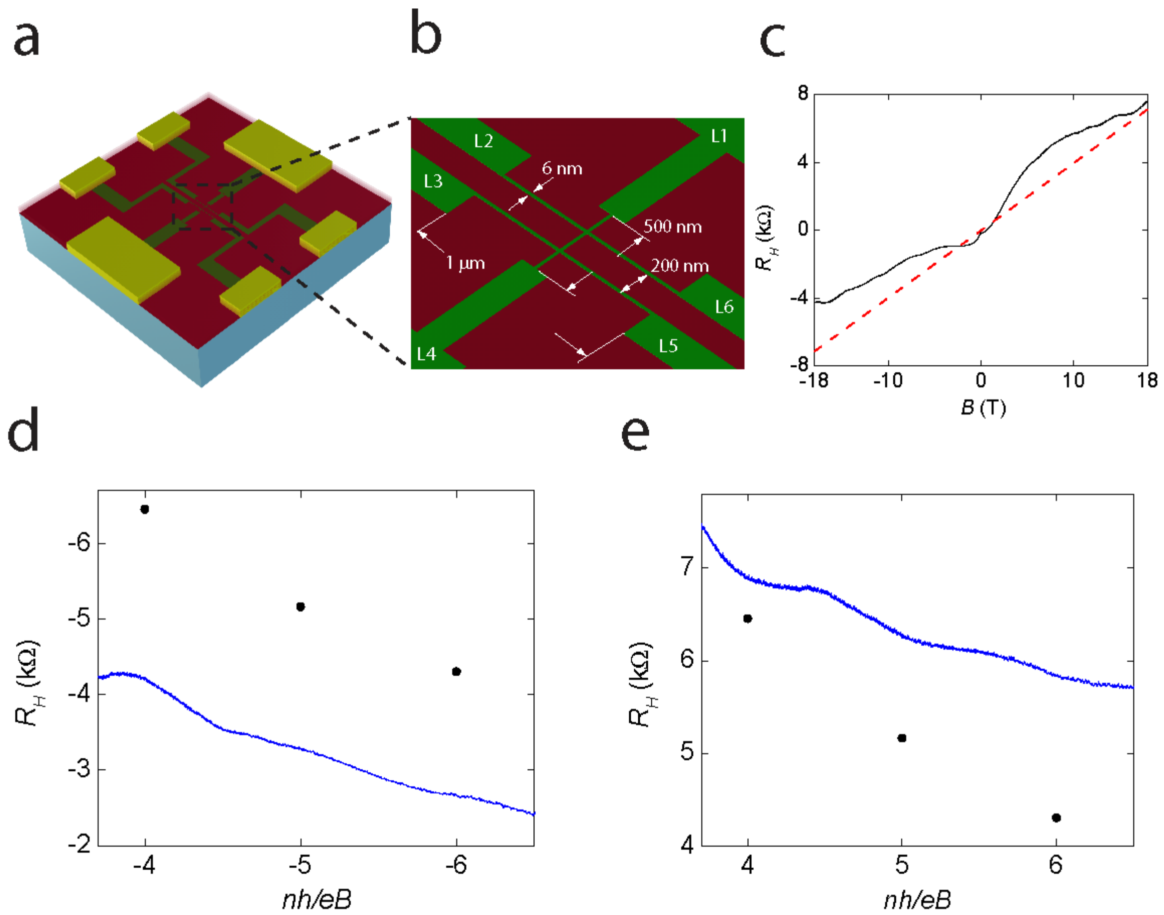

Figure 5-9 (a) Illustration of second nanostructure, formed from nanowires with measured width w=6 nm. (b) close-up, showing critical dimensions of Hall bar. (c) Hall resistance versus magnetic field at the junction formed by leads L1, L4, L3, andL5. The dashed line corresponds to a carrier density n=1.6 x 10^{12} cm^{-2}. (d,e) Hall resistance plotted as a function of the scaled inverse magnetic field *nh/eB*. Plateaus are observed for integer Landau level fillings. The expected quantized values of the Hall resistance are shown as points.

A direct measurement of the Hall effect was performed on a second structure with higher carrier density n=1.6 x 10^{12} cm^{-2} (Fig. 5-9) (See Section 10.4.2 for Hall measurement setup). In this experiment, distinct Hall plateaus were observed at values that correspond to expected

Landau level filling factors ν=4,5,6. Direct observation of Hall resistance plateaus provides independent supporting evidence of quantum Hall phenomena rather than some other origin.

Other possible interpretations of the observed phenomena not related to IQH and FQH effects cannot be definitively ruled out. Indeed, the quintessential characteristic of these phenomena, quantization of the Hall resistance, has not been directly measured. The IQH effect sequence of plateaus is rather unique in transport. Assigning the $\nu=1$ state to higher multiples of B_1 could restrict the observed plateaus to integer values and eliminate the need to invoke FQH effect. However, the notable absence of most of the "integer" plateaus leads us to discard that possibility. It's also discounted that the observed sequence of plateaus might be related to a series of "geometrical resonances". Small-amplitude oscillations that are periodic in $1/B$ have been observed at low fields for a unidirectional lateral superlattice [89] but not for the relatively simple geometries considered here.

While it has been shown that with higher carrier densities the electron gas forms a two-dimensional superconductor [15], acceptance of the standard quantum Hall interpretation immediately implies also that in the non-superconducting state, transport in the electron gas is strictly two-dimensional. Additionally, the Landau levels are expected to be fully spin-polarized due to the heavy electron mass.

The discovery of IQH and FQH states in oxides, a different class of materials than group IV and III-V semiconductors, brings with it a plethora of potential new physics and applications. Doped $SrTiO_3$ exhibits an unusually wide range of phenomena, including ferroelectricity, superconductivity and magnetism. The intermingling of these properties with strongly interacting multi-particle states will provide exciting new opportunities. For instance, the

interactions that lead to pairing and superconductivity in $SrTiO_3$ at zero magnetic field may lead to condensation of composite fermions and anyon superconductivity [90]. Perhaps the most tantalizing prospects lie in the potential to discover and braid nonabelian anyons near certain FQH states [91]. The precision with which oxide nanostructures can be defined [28,44] without sacrificing mobility (as demonstrated here) make them well suited for quasiparticle interference experiments in experimentally realizable topological quantum computing geometries [92].

6.0 A FERROELECTRIC OXIDE MADE DIRECTLY ON SILICON

This chapter is largely identical to the published paper in Science [20]*. The main contribution of the author was the piezo force microscopy measurements that directly probe ferroelectricity in* $SrTiO_3$*/Si structures. Samples were grown by collaborators in Pennsylvania State University. X-ray diffraction experiments were carried out by collaborators in National Institute of Standards and Technology and Northwestern University. Thermodynamics analysis was performed by collaborators at Penn State University. Piezo force microscopy measurements were carried out by the author, Charles R. Sleasman and Jeremy levy at University of Pittsburgh.*

Metal-oxide-semiconductor field-effect transistors, formed using silicon dioxide and silicon, have undergone four decades of staggering technological advancement. With fundamental limits to this technology close at hand, alternatives to silicon dioxide are being pursued to enable new functionality and device architectures. Ferroelectric functionality in intimate contact with silicon is achieved by growing coherently strained $SrTiO_3$ films via oxide molecular-beam epitaxy in direct contact with silicon with no interfacial silicon dioxide. Using piezo-force microscopy, ferroelectricity is observed in these ultra-thin $SrTiO_3$ layers. Stable ferroelectric nanodomains created in $SrTiO_3$ are observed at temperatures as high as 400 K.

6.1 INTRODUCTION

For decades, semiconductor device designers have envisioned numerous devices utilizing ferroelectrics in combination with semiconductors. These concepts include non-volatile memories[93-94] , “smart” transistors that can be used as temperature or pressure sensors [95] and ferroelectric field-effect transistors whose logic states require no power to maintain [96-97]. Missing, however, has been the ability to integrate ferroelectrics directly with mainstream semiconductors. Our work bridges this gap, demonstrating ferroelectric functionality in a $SrTiO_3$ thin film grown directly, without any intermediate layers and free of reaction, on the workhorse of semiconductor technology, silicon.

6.2 SAMPLE INVESTIGATED

Using molecular-beam epitaxy (MBE), collaborators in Penn State University have deposited epitaxial $SrTiO_3$ films on (001) Si substrates (Fig. 6-1) via a kinetically controlled growth process [43], which synchrotron diffraction measurements reveal to be commensurately strained up to a thickness of ~24 Å. Data from five $SrTiO_3$ films is discussed, identified by their nominal thickness in molecular layers (ML), i.e., 5 ML, 6 ML, 8 ML, 10 ML and 20 ML. These $SrTiO_3$ films were grown on (001) Si substrates by MBE in layers of one to a few molecular-strata at a time until the desired thickness was reached. The silicon substrates used in this study were *n*-type phosphorous doped (1-5 $\times 10^{15}$ phosphorous/cm^3) having a resistivity of 1-4 Ω·cm. Each layer that was grown involved a controlled sequence of steps[43], which kinetically suppress the oxidation of the substrate and reduce the tendency of the film to form islands[98].

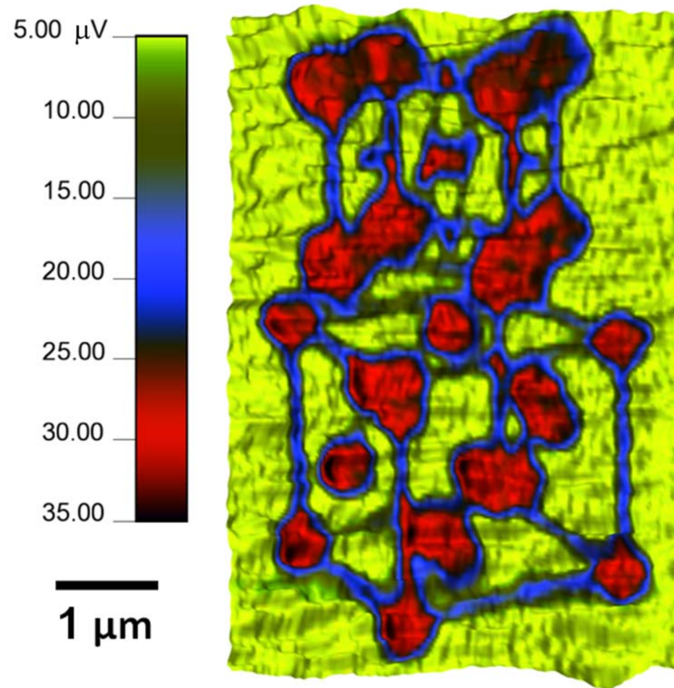

Figure 6-1 Structure of the $SrTiO_3$/Si interface, written and imaged on a 6 ML thick $SrTiO_3$/Si sample by piezo force microscopy. With the 45° in-plane rotational offset between the unit cells (*15*) the epitaxial orientation relationship is (001) $SrTiO_3$ // (001) Si and [110] $SrTiO_3$ // [100] Si.

X-ray diffraction reveals the structural quality and strain relaxation that occurs in the $SrTiO_3$ films as thickness is increased. Rocking curves in ω of the out-of-plane $SrTiO_3$ 002 reflection are shown in Figure 6-2A. Each curve displays an intense and narrow central peak due to coherently strained $SrTiO_3$ on top of a broad background peak. The height of the sharp central peak in relation to the background on this log intensity scale gives an indication of the fraction of the $SrTiO_3$ film that is coherently strained. The coherently strained fraction of the $SrTiO_3$ films decreases as the film thickness is increased. The full width at half-maximum (FWHM) of the 5 ML sample, 0.012°, is representative of the sharpness of the coherent peaks.

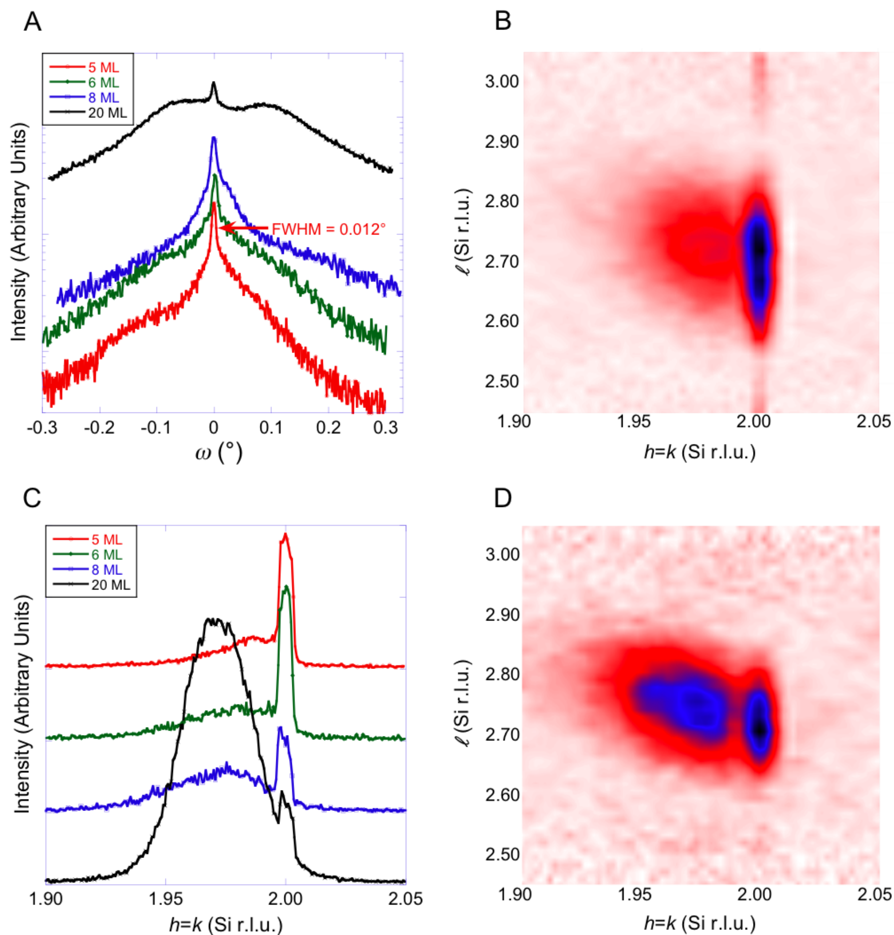

Figure 6-2 The strain state of the $SrTiO_3$ films revealed by x-ray diffraction. (**A**) Rocking curves in ω of the out-of-plane $SrTiO_3$ 002 reflection. (**B**) Reciprocal space map of the 202 $SrTiO_3$ peak for the 6 ML thick sample. Note the beating along the *l* direction. (**C**) Off-axis scans through the 202 $SrTiO_3$ peak. (**D**) Reciprocal space map of the 202 $SrTiO_3$ peak for the 8 ML thick sample

X-ray diffraction was employed to determine the in-plane strain of the $SrTiO_3$ films[98]. Since the out-of-plane lattice constant of $SrTiO_3$ is distinct from that of silicon, the in-plane lattice constant of $SrTiO_3$ can be obtained by measuring an off-axis $SrTiO_3$ reflection where there is no overlap with a substrate peak. Figure 6-2C shows scans made through the $SrTiO_3$ 202

peak for the 5 ML, 6 ML, 8 ML and 20 ML samples. The sharp peak observed at h=k=2.00 Si reciprocal lattice units (r.l.u.) is due to the commensurate portion of the $SrTiO_3$ films with in-plane lattice constant = $a_{Si}/\sqrt{2}$ = 3.840 Å. As the film thickness increases, the relative integrated intensity of the sharp peak decreases while that of a broad peak at h=k <2.00 Si r.l.u. increases. The plot clearly shows the transition from mostly commensurate $SrTiO_3$ to mostly relaxed $SrTiO_3$ as the film thickness is increased. Fig. 6-2B and 7-2D show reciprocal space maps of the $SrTiO_3$ 202 peak for the 6 ML and 8 ML samples, respectively. While the 6 ML sample (Fig. 6-2B), has its diffracted intensity mostly centered at h=k=2.00 Si r.l.u., for the 8 ML sample (Fig. 6-2D), more spectral weight is observed at lower values of h=k, i.e., at larger in-plane lattice constants due to relaxation of the $SrTiO_3$. The reciprocal space map for the 8 ML sample also shows how the spectral weight tails off to higher l with smaller h=k as strain relaxation sets in. From l scans made across the coherent peak at h=k=2.00 Si r.l.u., it's found that the coherent peak occurs at l ~ 2.71 Si r.l.u.

6.3 EXPERIMENTS AND RESULTS

To check for ferroelectricity in these strained $SrTiO_3$/ (001) Si films piezo-force microscopy (PFM) is used, a technique that has been demonstrated on ferroelectric films as thin as 28 Å[41,99-101] (See Section 10.2.3 for detail information of PFM) With strain relaxation occurring for $SrTiO_3$/ (001) Si film thickness as small as 8 ML (~32 Å), measuring the piezo response of such thin layers is challenging. The large d_{33} coefficients predicted for strained $SrTiO_3$/ (001) Si, however, makes it a reasonable signal to probe. Local electric fields were applied across the $SrTiO_3$ layer using a biased, conducting atomic force probe, and the resulting

piezoelectric response of the strained $SrTiO_3$ film was subsequently imaged using the same probe. A commercial atomic force microscope (AFM) (Asylum MFP-3D) was employed using Pt-coated (OMCL-AC240TM-W2) or diamond-coated (CDT-FMR-10) silicon cantilevers. Piezo force microscope (PFM) images were acquired using the following protocol: A voltage was applied to the tip: $V(t)=V_{tip}+V_{ac}\cos(\omega t)$, where ω is an angular frequency chosen to be close to the resonant frequency of the cantilever-sample system while in contact mode. The ac deflection of the cantilever was measured optically and detected using a lock-in amplifier. The phase of the lock-in amplifier was calibrated before each measurement such that a positive signal of the in-phase (X) channel was observed for sufficiently large V_{tip} bias. All signals acquired were taken from the X channel in this fashion. To read ferroelectric domains V_{tip} was set to 0 V.

Ferroelectric writing was achieved using the following protocol: A voltage $V_{tip}(x,y)$ was specified that corresponds to the image one intends to write (e.g., atomic structure of $SrTiO_3$/Si interface or an array of squares). The tip was held fixed while the sample position was scanned in a raster fashion such that $(x(t),y(t))$ sweeps out the entire area to be written. A voltage $V_{tip}(x(t),y(t))$ was applied as the sample was rastered to produce the desired domain structure.

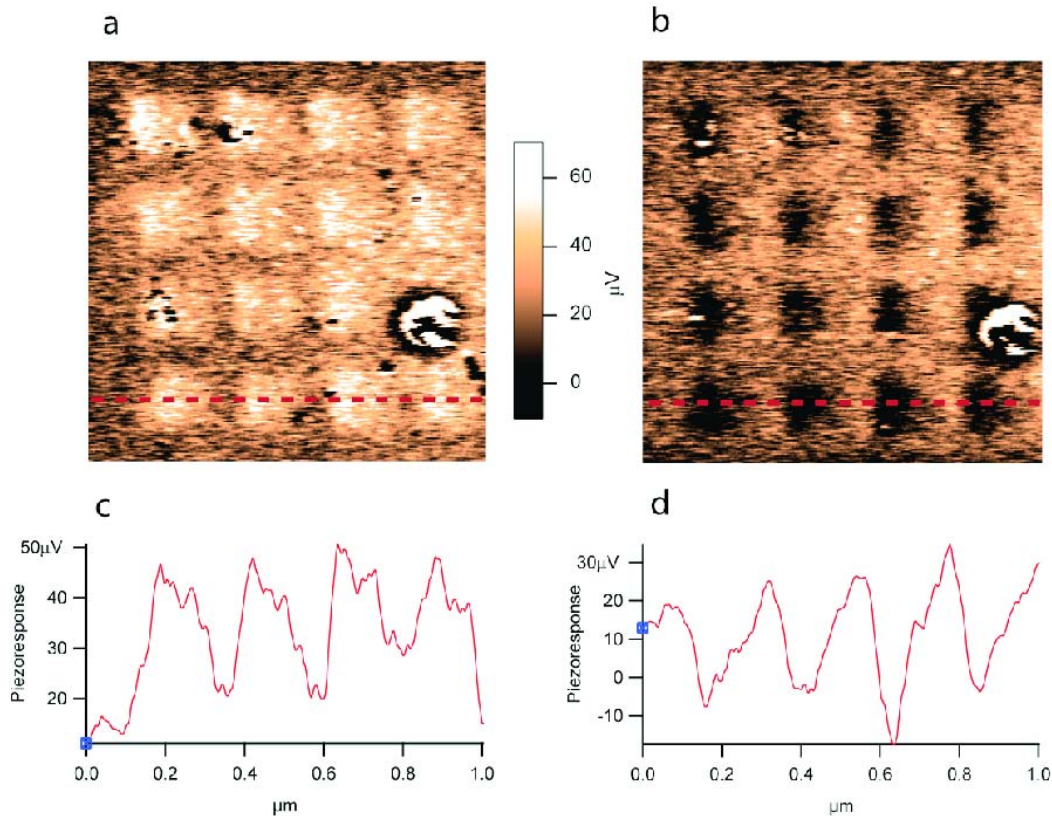

Figure 6-3 Bistable piezoelectric response. (**A**) PFM image of a 4×4 array of square positive domains, written with V_{tip} = +2 V and imaged at V_{tip} = 0 V. (**B**) Same as (**A**) except that the writing voltage V_{tip} = –2 V. (**C**) Linecut, shown above as a dashed line, indicating the profile of the piezoresponse for the case where V_{tip} = +2 V. (**D**) Same as (**C**) except V_{tip} = –2 V. The positive background piezoresponse, in the absence of poling, indicates a preferred downward orientation of the polarization of the as-grown film.

At room temperature, it's found that domains of both polarities could be patterned on the 5 ML, 6 ML, 8 ML, and 10 ML samples, but not on the 20 ML sample. Figure 6-1 shows a PFM image written on the 6 ML sample at room temperature. In all of the samples that exhibited ferroelectricity via piezoresponse, a preferred downward polarization was observed (Fig. 6-3). This agrees with reported x-ray fine structure measurements[102] and indicates that strained $SrTiO_3$ films on (001) Si are prepoled in their as-grown state. The lack of observable

ferroelectricity in the 20 ML sample is consistent with x-ray diffraction measurements showing that the 20 ML sample is mainly relaxed (Fig. 6-2C), and helps rule out other possible mechanisms, such as changes in surface chemistry, for the observed piezoelectric response in other samples. A retention study of the written domains was also carried out for the 6 ML sample at room temperature (Figs. 6-4, 6-5). The domain pattern was observed to be stable over a 72-hour period at which point the pattern was erased by rastering the atomic-force probe with a constant voltage over the patterned area.

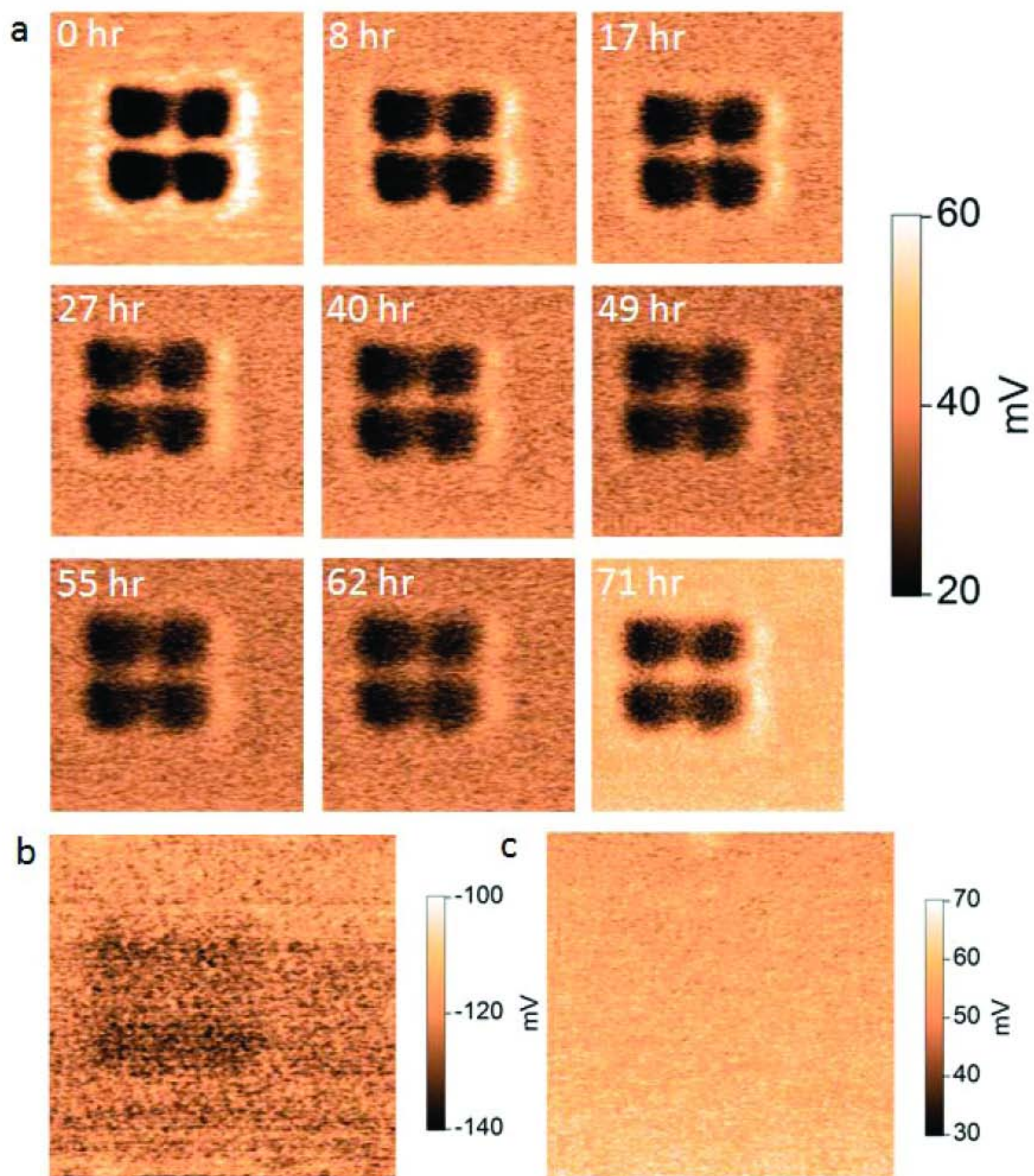

Figure 6-4 Retention of ferroelectric domains. (**A**) Images taken at different times during the 72-hour period of a 2 μm × 2 μm area of the 6 ML thick SrTiO3/Si sample that was patterned with four square domains. (**B**) PFM image obtained as the domains are being erased with *V*tip = –4 V. Note the change in the color scale. (**C**) PFM image taken after erasure showing no trace of the original domain pattern.

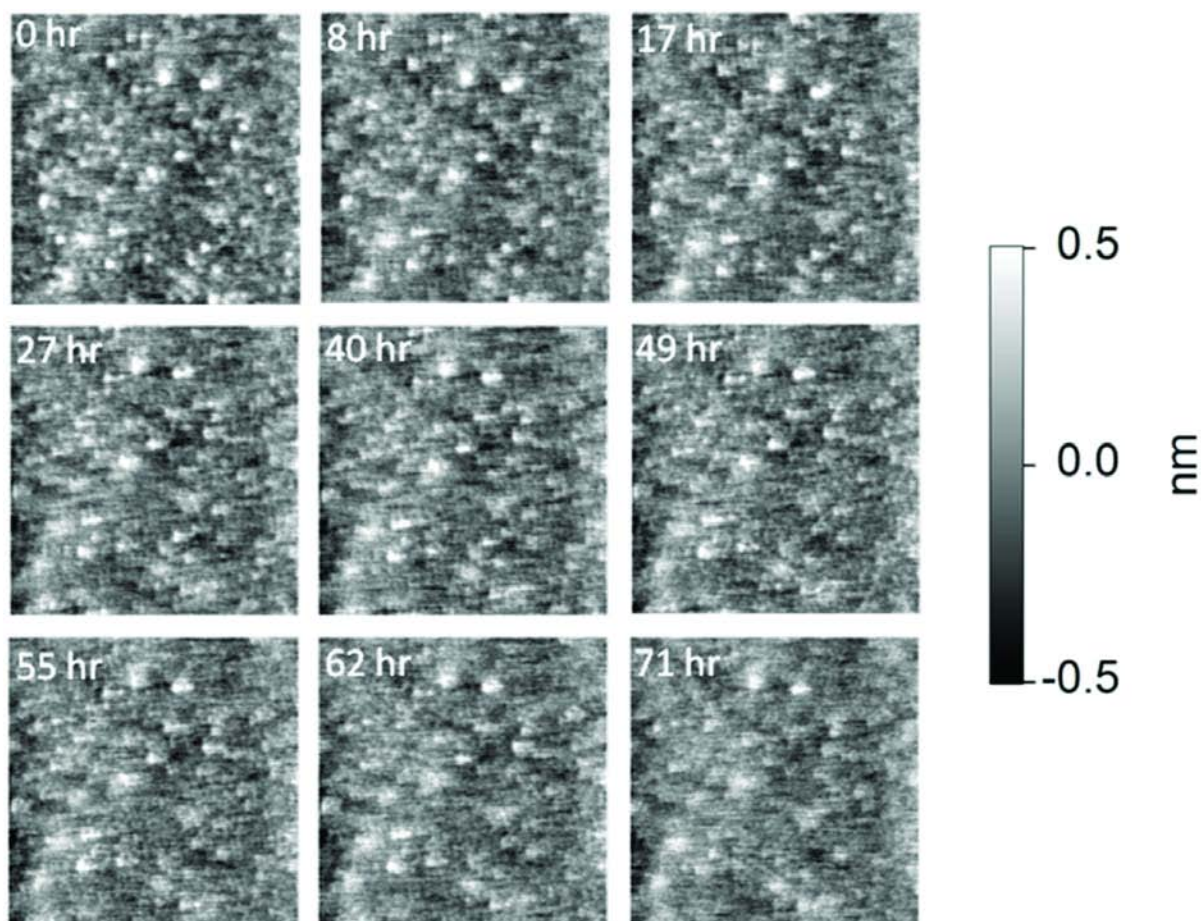

Figure 6-5 2 μm × 2 μm AFM topography images of the 6 ML thick $SrTiO_3$/Si sample taken simultaneously with the PFM images of Fig. S8A during a period of 72 hours. Images show a decrease in spatial resolution with time due to wearing of the tip.

PFM measurements performed as a function of temperature reveal a rather sharp phase transition, above which ferroelectric domains are unstable. Figure 6-6 shows a series of three PFM measurements made on the 5 ML sample at different temperatures. Each image was acquired approximately 30 min. after writing a 4×4 array of square domains. While some features that are associated with imperfections on the sample surface also show up on these images, at T=298 K each of the sixteen domains could be observed (Fig. 6-6A). The temperature

was increased and at T=314 K only 9 of the 16 domains could be seen (Fig. 6-6B). The existence of a single domain on the third row from the top rules out a variety of possible measurement artifacts, such as a "wandering" cantilever resonance frequency. At T=323 K (Fig. 6-6C) or at higher temperatures, no stable domains could be observed. These PFM measurements provide a lower bound on the paraelectric-to-ferroelectric transition temperature (T_C) $T_{C,5\ ML}$>314 K.

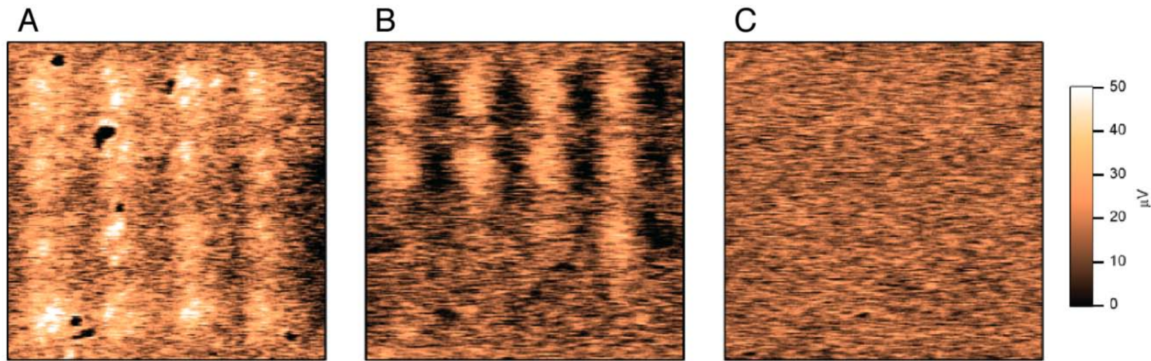

Figure 6-6 PFM images (1 μm × 1 μm) of a 4×4 pattern of domains written on the 5 ML thick $SrTiO_3$/Si sample at different temperatures. (**A**) T=298 K. (**B**) T=314 K. (**C**) T=323 K.

Measurements performed on the 6 ML sample, however, show that ferroelectric domains written on it are stable at even higher temperatures: $T_{C,6\ ML}$>410 K (Fig. 6-7) - temperatures significantly higher than that predicted by thermodynamic analysis. The theoretical calculation assumes an infinitely thick $SrTiO_3$ slab with complete polarization charge screening and with a uniform biaxial compressive strain equivalent to that obtained by growing commensurately strained $SrTiO_3$ on (001) Si. By leaving out surface effects such as structural and electronic discontinuities and the possibility of incomplete screening of the polarization charge, the thermodynamic analysis does not take into account the finite film thickness, which presumably

would lead to a substantially reduced transition temperature as has been shown for the related ferroelectrics $PbTiO_3$ [103] and $BaTiO_3$ [104]. Thus the observed experimental results indicate a substantially higher transition temperature than that predicted by theory. In the case of a metal in contact with a ferroelectric [105-106], polarization screening at the interface has been shown to enhance the ferroelectric T_C. Screening of the polarization charge as well as structural and electronic discontinuities at this heteroepitaxial $SrTiO_3$/Si interface, presently not considered in the thermodynamic analysis, could play a role in understanding the quantitative differences between experiment and theory.

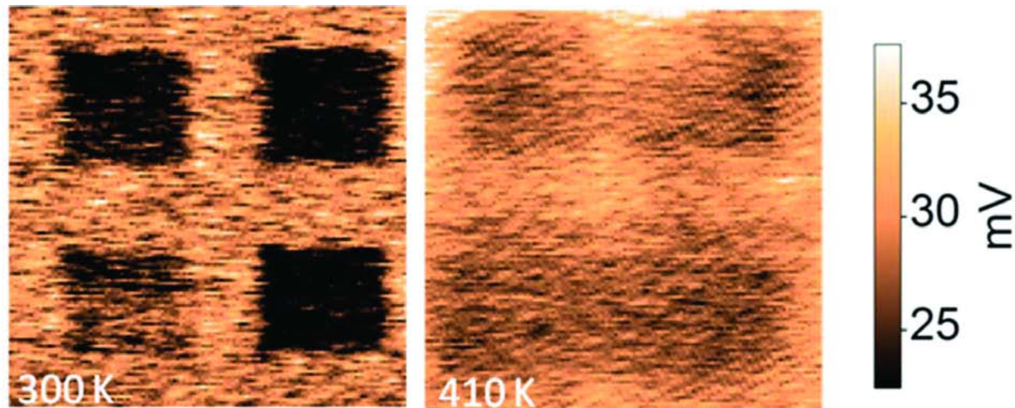

Figure 6-7 1 μm × 1 μm PFM image of four square domain patterns written and imaged on the 6 ML thick SrTiO3/Si sample at T=300 K and at T=410 K.

Phase transition temperature observed by PFM is in agreement with the temperature-dependent x-ray diffraction measurements of the out-of-plane lattice constant were performed on the 5 ML sample (Fig. 6-8)

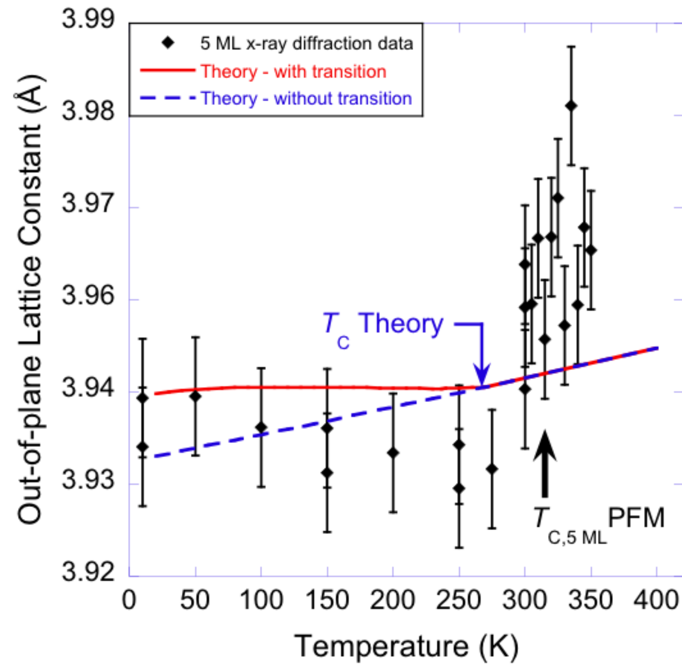

Figure 6-8 Temperature-dependence of the out-of-plane lattice constant of $SrTiO_3$ strained commensurately to the underlying silicon substrate. Theoretical prediction from thermodynamic analysis as well as experimental data obtained from x-ray diffraction measurements of the 5 ML thick sample is shown. The error bars reflect the maximum error expected considering systematic errors and that due to sample thickness. Also indicated is the transition temperature observed from PFM measurements for the 5 ML thick sample, $T_{C,5\ ML}$PFM.

6.4 CONCLUSION

A ferroelectric in direct contact with silicon invites hybrid ferroelectric-semiconductor devices [93-97]. While the low or almost non-existent conduction band offset predicted [107] and measured [108] between $SrTiO_3$ and silicon could lead to practical difficulties implementing such ferroelectric devices, it has been proposed that this problem can be overcome by carefully constructing the interface between $SrTiO_3$ and silicon [109-110].

7.0 FERROELECTRIC FIELD EFFECT TRANSISITORS ON SILICON

The structures used in experiments described in this chapter were grown by our collaborators at Pennsylvania State University. FeFET structures fabrication and transport measurements were carried out by the author at University of Pittsburgh.

$SrTiO_3$, as a great high-*k* alternative of the gate dielectrics, can promote the scaling down of metal-oxide-semiconductor field effect transistors (MOSFET) while maintain the large gate tunability. With the recent successful growth of ferroelectric $SrTiO_3$ thin films directly on Silicon [20], the persistently tunable polarization in $SrTiO_3$ can be used to gate the conductance in Si, which makes possible a novel class of Si based ferroelectric field effect transistors (FeFET). Here demonstrates the operation of FeFET structures fabricated in heterostructures of 6 mono layer (ML) thick ferroelectric $SrTiO_3$ thin films grown on Silicon on insulator (SOI) wafers with 200 nm device layers. Switching effect on the Si conductance as large as 10% as well as pronounced switch ability by electric pulse as short as 10 μs are observed.

7.1 INTRODUCTION

A ferroelectric field effect transistor (FeFET) replaces the insulating layer of a conventional metal-oxide-semiconductor field-effect transistor (MOSFET) with a ferroelectric

layer so that channel carrier density can be persistently tuned by remnant polarization in the ferroelectric layer. Since the conductance level in the semiconductor channel offers a direct and nondestructive readout of the polarization states in the ferroelectric layer, FeFET find its application in non-volatile random access memory (FeRAM) and information storage devices. Ever since the proposal of ferroelectric field transistors (FeFET) in 1950s[111], great efforts have been made in numerous approaches. However, fully functional device with adequate retention time and writing erasing cycle number as well as fast operating speed is yet to be developed. The major reason is that the interfaces between ferroelectric perovskite oxides and semiconductors are difficult to control. Any defects or interfacial trapping states can seriously degrade the interface quality. The use of heterostructures composed of only perovskite materials has been proposed [112], but integration with semiconductors is still desirable both functionally and economically.

Recently, high quality interface between $SrTiO_3$ and Si has been achieved by molecular beam epitaxy (MBE) [20]. Strain induced by lattice mismatch give rise to a ferroelectric state in $SrTiO_3$ thin film with a ferroelectric transition well above room temperature. Taking advantage of this technological advancement, FeFET devices are fabricated and characterized based on such strained $SrTiO_3$/Si heterostructures. Instead of bulk Si substrate, a Silicon on insulator (SOI) wafer with a thin Si device layer was used to ensure the tunability.

7.2 SAMPLE INVESTIGATED

6 ML strained $SrTiO_3$ film is grown using the same method as described in Ref[20]on a SOI wafer with a 200 nm thick n-type Si device layer and 400 nm SiO_2 buried oxide (BOX) layer. The Si device layer has a specified sheet conductivity of 30-56 Ωcm.

FeFET structures fabricated are composed of three electrical terminals defined by electron beam lithography (EBL): source (S), drain (D) and gate (G) as illustrated in Figure 7-1. Surrounding the device, material above the BOX layer is removed by reactive ion etching (RIE) in CF_4/O_2 mixing gas plasma to provide electrical isolation. Source and drain electrodes are formed by first etching away top $SrTiO_3$ layer by RIE then thermally evaporating Al followed by Au to form Ohmic contact with the Si channel, while in the gate region, Au is directly deposit on the $SrTiO_3$ layer. See Section 10.1 for details of sample preparation methods.

Samples with the same structure except for an exposed $SrTiO_3$ layer in gate region are characterized using piezo force microscopy (PFM) as described in Ref[20], and ferroelectric property is confirmed.

7.3 EXPERIMENTS AND RESULTS

To demonstrate the nonvolatile operation of the FeFET structures, following switch experiment (Fig. 7-1) is applied. First voltage pulse with amplitude V_1 and duration τ_1 is applied to the gate electrode while source and drain are grounded. Electric field generated across the $SrTiO_3$ layer poles the electrical polarization in the parallel direction, which alters the bound charge density at the $SrTiO_3$/Si boundary. To screen such a bound charge, carrier in Si will be

either attracted or repelled depending on the pulse polarity, which correspondingly changes the carrier density in the Si channel underneath the gate electrode and modifies the channel conductance. After the pulse, change in the channel conductance is monitored by applying a small AC voltage to the source and measuring the current flow though the drain electrode with a lock in amplifier. The gate electrode is intentionally floated during this measurement to suppress the leakage current. A second gate voltage pulse of opposite polarity is then applied with amplitude V_2 and duration τ_2, and the effect on channel conductance is measured again.

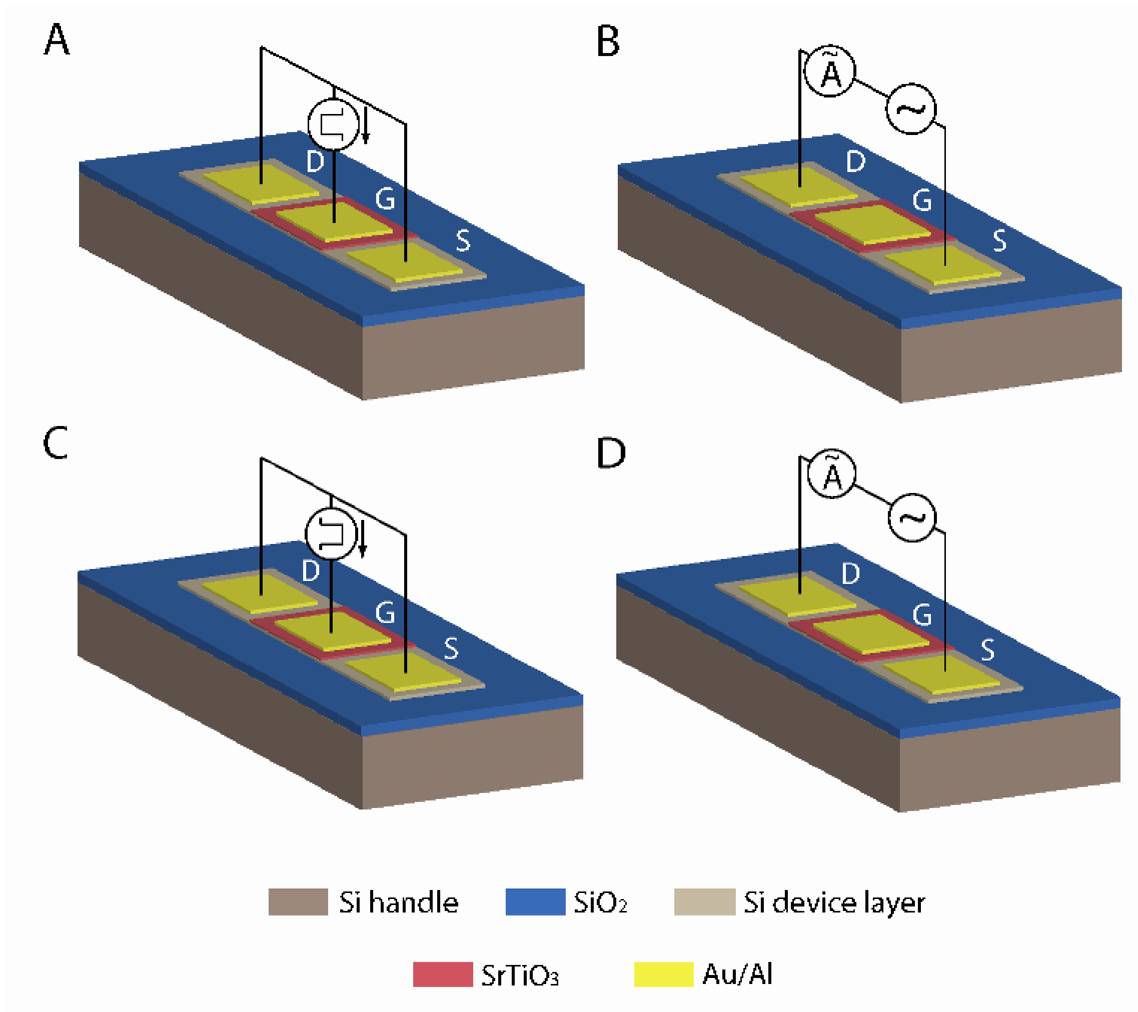

Figure 7-1 Illustration of FeFETs made in $SrTiO_3$/SOI samples and the measuring sequence. (A)A voltage pulse with certain polarity is applied to the gate (G) electrode while source (S) and drain (D) electrodes are grounded. (B)

After the first pulse, (A) Another voltage pulse with opposite polarity is applied to G while S and D electrodes are grounded. (D) After the second pulse, conductivity between S and D is measured while G is floated again.

Clear n-type modulation of Si channel conductance is observed when pulse train, which is composed of pulses with alternating polarities, is applied. In general, remnant polarization in $SrTiO_3$ layer after a positive gate pulse increases the channel conductance, while remnant polarization after a negative gate pulse reduces the conductance. Figure 7-2 shows the data measured when applying a pulse train with $\tau_1 = \tau_2 = 10$ μs. Interestingly, symmetric pulse train with $|V_1| = |V_2| = 5$ V doesn't modulate the channel conductance by much (Fig. 7-2A), while an asymmetric pulse train with larger negative pulses (V_1 = -10 V, V_2 = 5 V) starts to pull the channel conductance away from the initial value (Fig. 7-2B) and eventually realizes an approximately 0.6% stable modulation of the conductance (Fig. 7-2C). This indicates that the state with a polarization parallel with electric field generated by a positive pulse is favored by the system, which is in agreement with previous PFM and X-ray fine structure measurement results that the as grown sample is pre-poled downward [20].

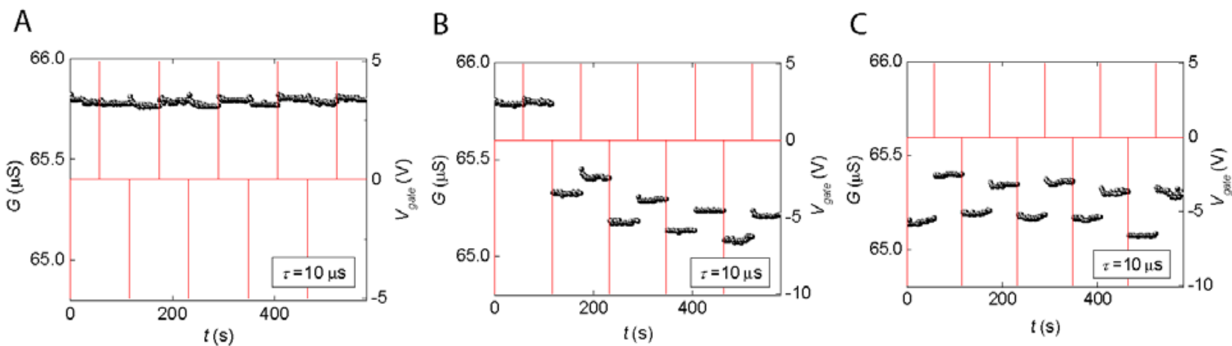

Figure 7-2 Nonvolatile switching effect on the Si channel conductance *G* by voltage pulse applied across the gate $SrTiO_3$. Sample favors the states with a spontaneous polarization pointing down. (A) Symmetric pulse train cannot

switch $SrTiO_3$ from the spontaneous state. (B) Asymmetric pulse train starts to pull the system away from the spontaneous state. (C) Stable switching effect can be achieved after certain numbers of cycles.

Generally, pulse trains with pulses of longer duration and larger amplitude show larger modulation ability. Figure 7-3 plots the conductance modulation percentage achieved by $\tau_1 = \tau_2 =$ 3 s pulse train as a function of $|V_{Gate}|$ =max ($|V_1|$, $|V_2|$). Note that to achieve the maximum modulation, the amplitude ration between positive and negative pulses is optimized and usually $|V_{Gate}|$ is equal to the negative pulses' amplitude. By increasing the pulse amplitude $|V_{Gate}|$ to 34 V, a modulation percentage of 10% can be obtained.

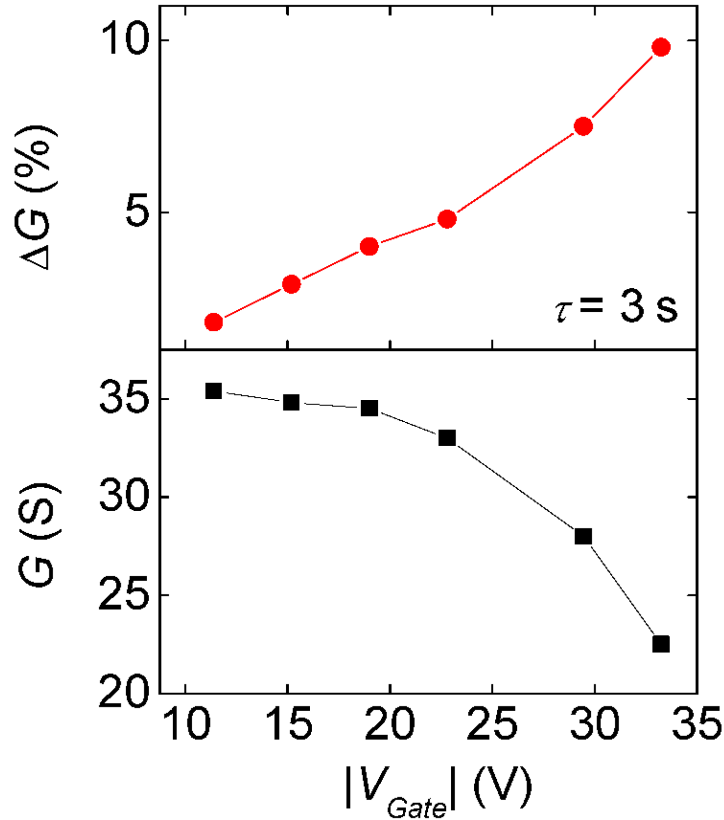

Figure 7-3 Switching effect amplitude and absolute value of channel conductance as functions of switching pulse amplitude applied across the gate $SrTiO_3$.

Different voltage values applied to the back of Si handle is also explored to find the optimized regime for FeFET operation (Fig. 7-4). Largest conductance is always achieved when zero back bias is applied. Large negative back bias will pinch off the carrier density in the Si device channel and also suppress the conductance modulation induced by $SrTiO_3$ remnant polarization. Positive back bias increases the carrier density and within moderate value range still allows the conductance modulation, but the conductance modulation percentage decreases due to the larger conductance background.

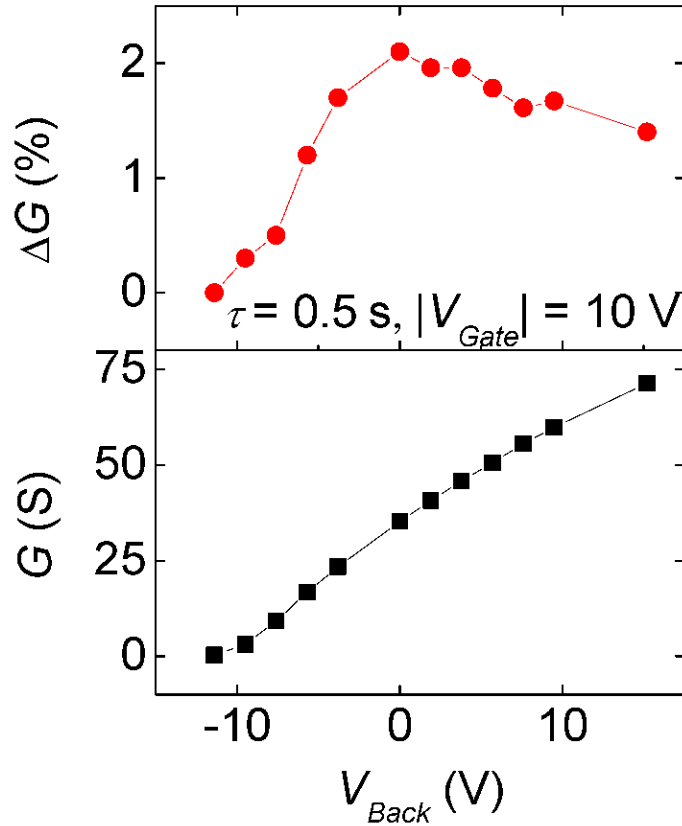

Figure 7-4 Switching amplitude and absolute value of channel conductance as functions of voltage applied to the back of Si handle.

As a control experiment, similar FeFET devices are also fabricated on sample with 5 ML $SrTiO_3$ and characterized. Conductance modulation observed is smaller comparing with 6 ML samples, which is consistent with that the ferroelectric polarization tunability is also smaller as measured by PFM. In fact, samples with 5 ML $SrTiO_3$ grown on bulk Si substrate does has a much lower ferroelectric transition temperature than samples with 6 ML $SrTiO_3$ [20].

7.4 PERSPECTIVE

N-type FeFET devices fabricated directly on SOI wafer have been demonstrated. Current n-type SOI wafer with 200 nm Si device layer used is manufactured by wafer bonding technique. In the future, to realize larger gate tunability, SOI wafer made by "separation by implantation of oxygen" (SIMOX) technique which yields Si device layer as thin as 10 nm is more desirable. Also, p-type FeFET can be fabricated choosing p-type substrate, which together with n-type FeFET can lead to more complex logic devices.

With $SrTiO_3$ as the buffer layer, there is potential to grow another magnetic perovskite layer in source and drain as in lateral spin-valve devices. Possible injection of spin polarized hot electrons tunneling through $SrTiO_3$ layer into Si and detection will opens numerous opportunities for Si based spintronics.

8.0 TIME RESOLVED LATTICE DYNAMICS STUDY OF $SrTiO_3$ ULTRATHIN FILMS GROWN DIRECTLY ON SILICON

Thin film samples used in experiments described in this chapter were grown by collaborators in Pennsylvania State University. Optical measurements were carried out by the author at University of Pittsburgh.

Time-resolved two color pump-probe polarization microscopy was performed at room temperature on $SrTiO_3$ films grown directly on Si with thickness varying from 1.6 nm to 38 nm. Coherent phonon oscillations at 190 GHz were observed. The quality factor of the time-resolved signal Fourier transform peak at 190 GHz decreases with film thickness and shows a kink at a thickness of 10 Molecular layers (ML), the thickness at which the film switches from being coherently strained to being relaxed. The dependence of the coherent phonon signal on pump and probe laser polarization is investigated.

8.1 INTRODUCTION

Great effort has been made in the integration of traditional semiconductors with oxide materials which exhibit numerous novel functional properties such as ferroelectricity, superconductivity and field tunable interfacial metal insulator transition etc. $SrTiO_3$ combines

most of the merits of the oxide materials, and serves as a template for the growth of various oxide thin films. Successful growth of strain-engineered ferroelectric $SrTiO_3$ thin films directly on Si was reported recently [20]. For future ferroelectric device implementations, understanding the complex lattice dynamics, which is closely related to key material parameters like the dielectric constant, is very important.

Traditionally, frequency domain methods such as Raman scattering and neutron diffraction have been used to detect phonon oscillations. However, for the measurement of heavily damped phonon modes with relatively low frequencies, especially in ultrathin films with small scattering cross sections, these methods are difficult to apply. On the other hand, time domain pump-probe techniques, which uses femtosecond laser pulses to generate and detect spatially and temporally coherent lattice vibrations, has been applied to various semiconductors and complex oxide systems.

Here presents room-temperature measurements of a coherent longitudinal acoustic phonon mode in strained $SrTiO_3$ films grown directly on Si. Films with thickness between 5 Molecular layers (ML) and 10 ML are reported to have a ferroelectric transition temperature above room temperature. A two color pump- probe electro-optic sampling method is employed to detect the impulsive stimulation and subsequent detection of coherent phonons in this ultrathin film of SrTiO3 grown directly on Si. The electrooptic contrast arises due to a transient anisotropy in material refractive index due to excitation of coherent acoustic phonons. Due to the high signal to noise ratio of balanced detection technique, clear phonon oscillations are observed in films as thin as 1.6 nm (4 ML).

8.2 SAMPLE INVESTIGATED

$SrTiO_3$ films of thickness d = 4, 5, 8, 10, 20ML studied here were grown by molecular beam epitaxy (MBE) with epitaxial orientation: (001)$SrTiO_3$ // (001)Si; [110]$SrTiO_3$ // [100] Si. These are the same set of samples as described in Chapter 6.

8.3 EXPERIMENTS AND RESULTS

Coherent phonon dynamics at room temperature is studied with ultrafast polarization spectroscopy using a standard pump-probe method (Fig. 8-1A). A linearly polarized pump pulse (120 fs) is intensity modulated at $\omega/2\pi$ = 42 kHz and then focused at normal incidence onto the sample. Pump beam wavelength (820 nm) is chosen to be below the bandgap of Si to avoid photoexcitation of carriers in the substrate. The ultrashort pump pulse imparts an impulsive force to the sample lattice, creating coherent phonon through impulsive stimulated scattering (ISS) process (see Section 10.3.2 for details). These coherent phonons are probed using a probe pulse generated at the second harmonic of the pump beam (410 nm). This probe beam is time delayed and focused to the same spot on the sample. Phonon oscillations will induce periodic anisotropy in the refractive index of the sample and thus change the polarization of reflected probe pulse. The delay time between pump and probe is swept to map out the time resolved signal. The reflected probe beam is split into signal and reference channels of a balance detector using a polarizing beam splitter. The balance is adjusted so that the signal before zero delay is minimized, to suppress the unwanted background and noises. After zero delay, the polarization rotation of probe pulse is measured at second harmonic of the pump's modulation frequency, to

exclude the influence of mechanical vibrations caused by the photoelastic modulator. The entire setup is illustrated in Figure 7-1 A.

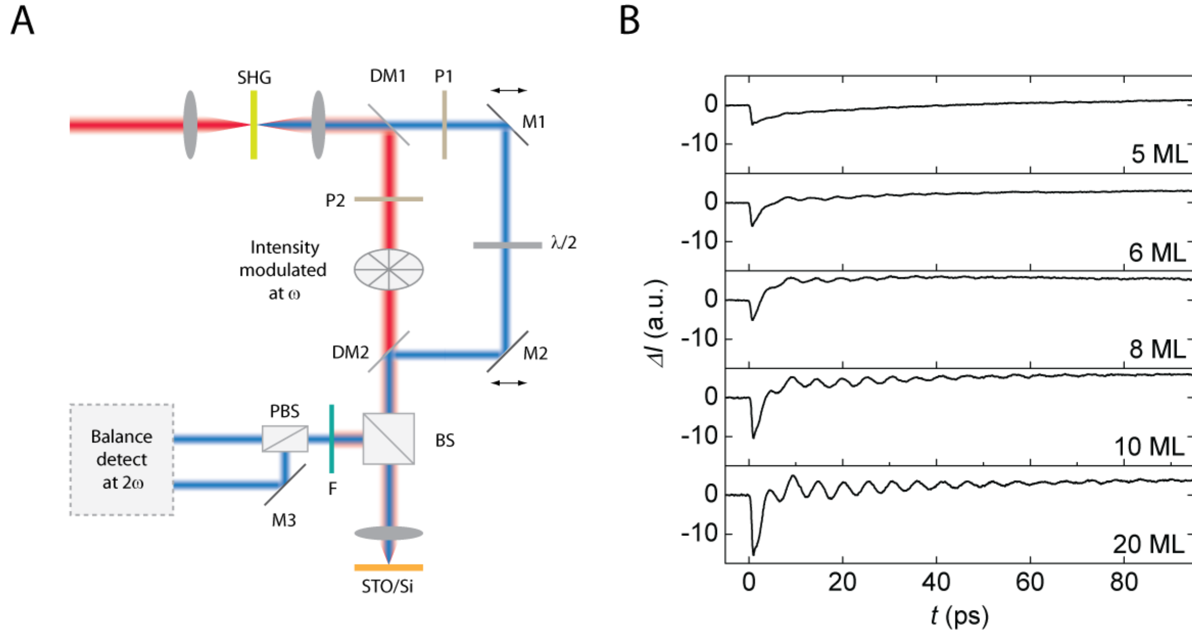

Figure 8-1 (A) Layout of pump-probe setup described in text. SHG: second harmonic generator; DM: dichroic mirror; P: polarizer; M: mirror; λ/2: half wave plate; BS: beam splitter; F: filter; PBS: polarizing beam splitter. (B) Coherent phonon oscillations measured in $SrTiO_3$ films with different thicknesses.

With incident probe beam's polarization perpendicular to the pump, signals of reflected probe's polarization change ΔI measured as a function of the delay time t between pump and probe are plotted in Figure 8-1B. At zero delay $t = 0$, a big signal rises due to coherent interaction between the pump and probe beams, and does not yield information about the coherent phonons. After that, damped phonon oscillations are observed. Figure 8-2 shows the data after low pass filtering is applied to ΔI (t), and the result is subtracted to reveal the coherent phonon signal ΔI_{cp} (t). ΔI_{cp} (t) measured in samples with five different $SrTiO_3$ film thicknesses

are plotted in Figure 8-2A. The amplitude of phonon oscillations decreases when film gets thinner. Fourier transform of ΔI_{cp} (t) (Fig. 8-2B) shows a frequency component peak at f_{cp} = 190 GHz. The quality factor of the Fourier transform peak is plotted in Figure 8-2C as a function of film thickness. A sharp discontinuity occurs at 8 ML < d < 10 ML which agrees with previous X-ray diffraction finding [20] that above 8 ML, $SrTiO_3$ film with go through a transition from mostly commensurate to Si to mostly relaxed. Below d_c (d critical), the amplitude appears to increase quadratically, indicating that the phonon oscillations are highly coherent. Above dc the increase seems to increase linearly, indicating a loss of coherence which is attributed to relaxation of the SrTiO3 film.

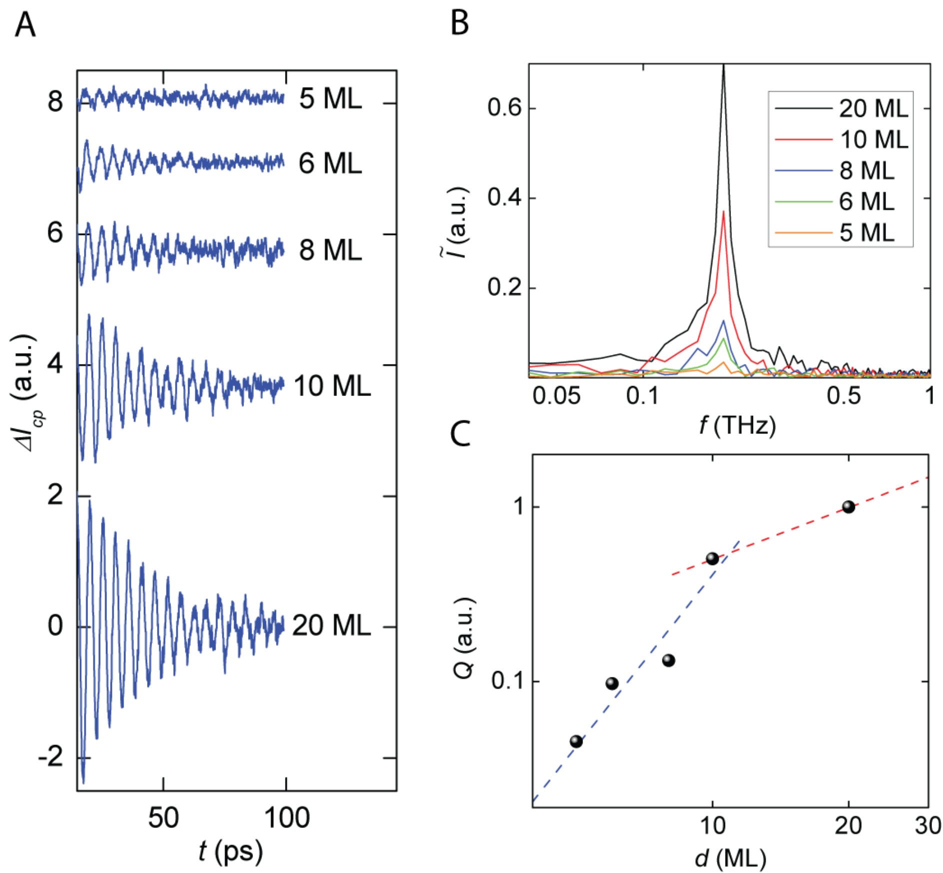

Figure 8-2 Damped phonon oscillation signal extracted after background subtraction. (B) Fourier transform (FT) of coherent phonon oscillations showing a peak at f_{cp} = 190 GHz. (C) Quality factor Q of FT peak decreases quadratically as a function of $SrTiO_3$ film thickness d when $d \leq 10$ ML and linearly above 10 ML.

Data was acquired at different polarizations of probe θ to understand the nature of the coherent phonon mode observed. At $\theta = 45°$, oscillation signal completely vanishes; at $\theta = 0°$ and 90º, magnitude of oscillation is maximized, while the phase is differed by π (Fig. 8-3). This angle dependence excludes phonon modes with vibration along c-axes, for they modify the in-plane components of refractive index isotropically and thus will not distinguish measurement

geometries with different probing polarizations. Also noted that f_{cp} is one order of magnitude lower than the frequencies reported for optical phonons in $SrTiO_3$[113]. The coherent phonon observed are therefore attributed to acoustic modes (Γ_2^-). When probe polarization has a 45 degree angle with the pump, the two degenerate TA phonon modes rotate the polarization of the scattered probe pulse by the same amount in opposite directions, giving rise to a zero net modulation of the probe pulse.

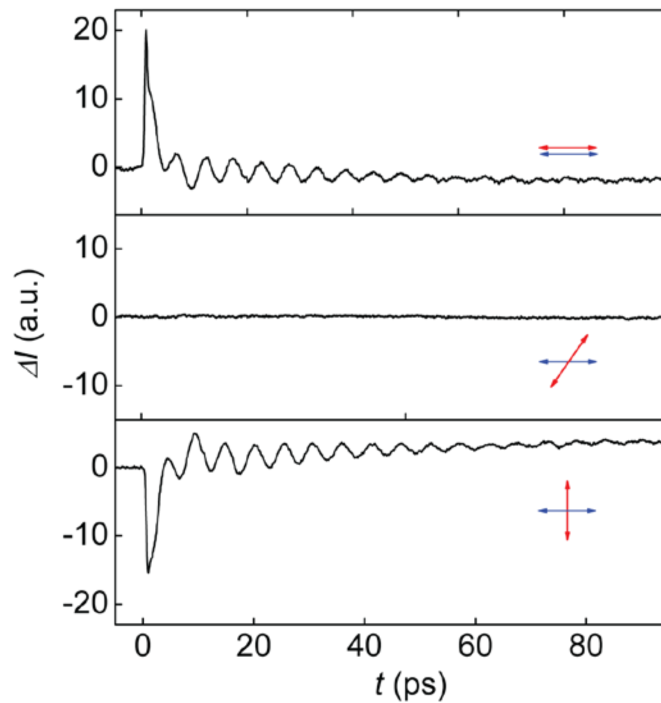

Figure 8-3 Coherent phonon oscillations in 20 ML thick $SrTiO_3$ film at three different relative polarization angles between pump and probe $\theta = 0^\circ, 45^\circ, 90^\circ$.

8.4 CONCLUSION

In summary, coherent phonon oscillations are observed in ultra thin $SrTiO_3$ films grown directly on Si substrates using ultrafast pump-probe method. The coherent phonon modes are believed to originated from the Γ_2^- acoustic branch. Indication of a transition from commensurate to mostly relaxed as $SrTiO_3$ layer gets thicker is observed. With future optimization, such as shortening of the pump and probe pulses as well as temperature dependent experiments, the ability to characterize lattice dynamics within a few monolayer thin materials opens new avenues for studying the dielectric properties and nature of ferroelectricity in thin film oxide materials.

9.0 SUMMARY AND OUTLOOK

This thesis presents studies carried out on two classes of complex-oxide heterostructures. Room temperature reversible nanoscale control of an interfacial metal-insulator transition by conductive AFM lithography is achieved at the interface between $LaAlO_3$ and $SrTiO_3$. Strain-induced ferroelectricity is confirmed and characterized in $SrTiO_3$ thin film grown directly on Si. On the basis on these discoveries, several proof-of-concept device structures have been demonstrated, which not only show great application potential but also provide a framework for the investigation of many interesting classes of behavior in condensed matter systems.

There are still several fascinating research directions offered by these two complex oxide systems which are beyond the scope of this thesis. As an example, one can take advantage of the versatility of the nanoscale patterning procedure developed in Chapter 2 to create and characterize low-dimensional structures whose properties are essentially quantum mechanical. Low temperature, high magnetic field studies of quantum Hall phenomena in nanostructures has been discussed in Chapter 5. The non-destructive AFM lithography technique can be very useful in making quantum mechanical devices which usually require complex lithographic procedures to define and are extremely sensitive to defects and impurities that might be introduced to the materials at the same time. For example, oxide interferometers measuring the quasiparticle charge in fractional quantum hall states and two dimensional potential lattices (in analogous to conventional optical lattices) simulating Hubbard model are all potentially intriguing subjects of

study. Also, more experiments need to be carried out to explore the spin degree of freedom in these complex oxide systems as well as the possible coupling and control methods. With interfacial magnetism already discovered [18] and the built-in electric field developed during writing process, manipulation of spin via spin-orbit coupling may be achieved in interfacial structures written at $LaAlO_3/SrTiO_3$ interface by AFM lithography. FeFET devices can also be modified to study the possible spin injection into Si. Lastly, the integration of these two heterostructures (*e.g.* $LaAlO_3/SrTiO_3/Si$) may give rise to coupling between different functionalities and introduce new device concepts. Especially, q-2DEG can be defined and used as gate electrodes for Si based devices, which can provide ultra-high gate density and modifiable gates arrangement without the forming of a depletion layer as in traditional Si gating method.

10.0 EXPERIMENTAL METHODS AND THEORY

10.1 SAMPLE PREPARATION METHOD

10.1.1 Electron Beam Lithography (EBL) and photolithography

Photolithography and electron beam lithography (EBL) were used frequently to define permanent device structures and electrode contacts with dimensions above 1 μm or in nanoscale respectively.

Photolithography is usually carried out by mask aligning system, which uses UV light to expose a resist layer covering the sample surface and induce molecule structure change in exposed areas. A predefined photomask selectively let through the UV light and thus transfer its own pattern onto resist layer. The exposed or unexposed areas can later be removed by developing chemicals depending on the property of resist, *e.g.* for positive tone resist, exposed area will dissolve in developer, while for negative tone resist, unexposed area will dissolve away (Fig. 10-1). Resolution limit is determined fundamentally by optical diffraction as well as other factors like the relative flatness of both mask and sample surface, and the closeness with which sample and mask can be contacted. Usually features below 1 μm are difficult to fabricate using optical lithography.

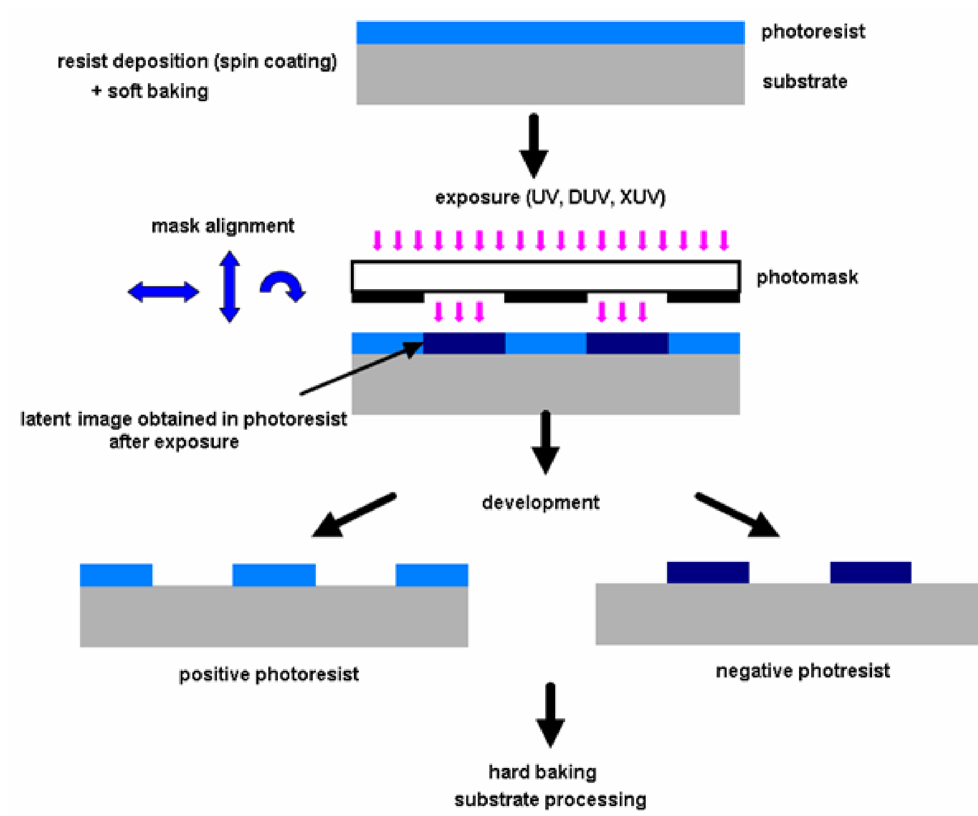

Figure 10-1 Illustration of typical photolithography procedures. (Adapted from commercial website)

EBL systems instead scan focused electron beam in controlled pattern to realize the selective exposure of resist. Since there is not contact problem involved and also electrons have much shorter wavelength than light, resolution is greatly improved. For example, in the system that were used in my research projects (Raith *e-line* system), 20 nm feature sizes can be achieved with highest electron kinetic energy setting. The other advantage is no predefined mask is required. One disadvantage though is the slow exposure speed due to raster scanning process.

10.1.2 Dry Etching

Various dry etching steps were applied to transfer the pattern from resist layer to samples, including reactive ion etching (RIE) and ion milling.

RIE uses chemically reactive plasma generated under vacuum by radio frequency electromagnetic field to remove materials. Reacting rates of different materials with plasmas generated from different gases varies largely, which allow RIE to selectively etch away certain material layers in samples.

Comparing with RIE, ion milling is a more physical etching process. It uses high energy noble gas ion (usually Ar^+) to bombard sample surface in high vacuum and knock out surface atoms by transferring momentum. Ion milling avoids unwanted element doping to sensitive samples, but can be used to create oxygen vacancies in oxide material to change sample transport properties as wanted.

10.1.3 Metal Deposition

Metal deposition is an essential step in making electrode contacts. Different metals are chosen to form either ohmic or Schottky contact with samples. Thermal evaporation and electron-beam evaporation are used depending on metals' vapor pressures and vacuum requirement.

A thermal evaporator uses an electric resistance heater to melt the material and raises its vapor pressure to allow the material reach and re-condensate on samples. Only materials with a much higher vapor pressure than the heating element can be deposited without contamination of the film.

An electron-beam evaporator uses a high-energy (and high current) electron beam from an electron gun to boil a small spot of material. Since the heating is not uniform, lower vapor pressure materials can be deposited; also, higher local temperatures can be achieved to deposit materials with higher melting points.

10.2 ATOMIC FORCE MICROSCOPY (AFM)

Atomic force microscope (AFM) is one of many types of scanning probe microscopes. It uses a cantilever with a sharp tip (usually with a radius of curvature on the order of 2-20 nanometers) to scan the sample surface. When the tip is brought close to the sample surface, forces between tip and sample will cause bending deflection of the cantilever. Possible forces include mechanical contact force, van der Waals forces, capillary forces, chemical bonding, electrostatic forces, magnetic forces, Casimir forces, solvation forces, etc. Depending on the nature of the force, the deflection signal can be used to spatially map out the information like surface topography, electric potential, magnetic moment and chemical bonding energy, etc.[114] At the same time, tip is also exerting a force to the sample which leads to applications in nanolithography and manipulation.

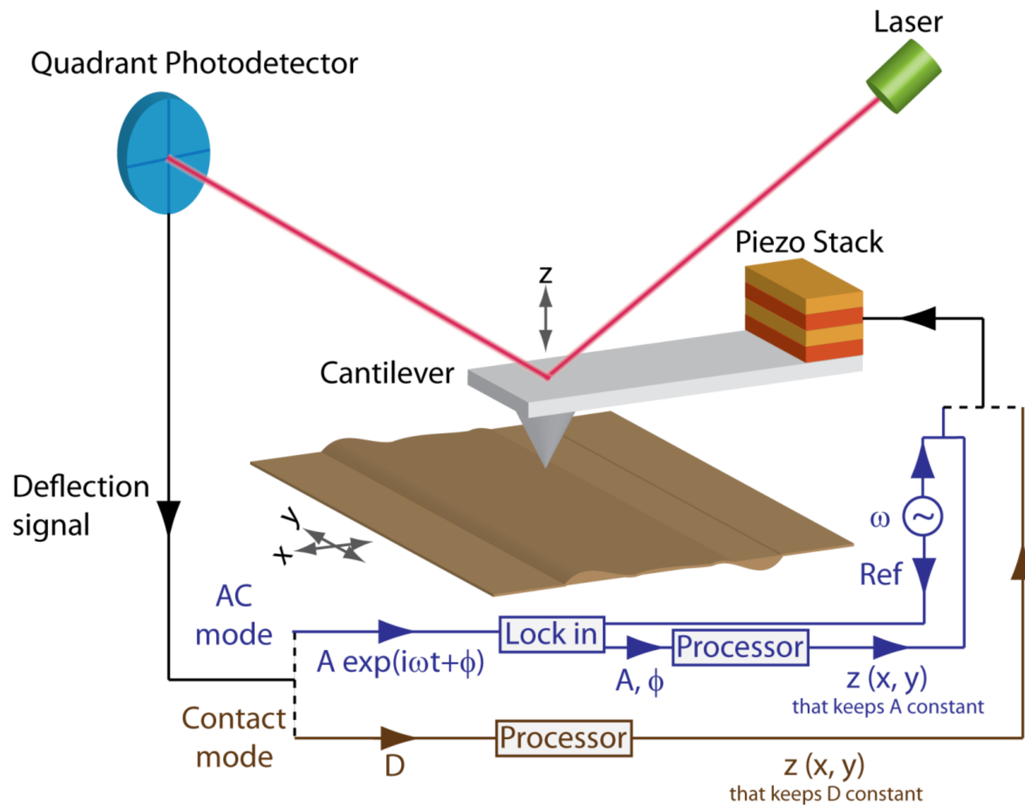

Figure 10-2 Illustration of essential components of an atomic force microscope and two most commonly used scanning modes: AC mode and contact mode

There are two most commonly used scanning modes: Contact mode and AC mode[115] (Fig. 10-2). In contact mode, A laser beam coming from the laser diode incidents on the back of the cantilever and is deflected to a quadrant photodetector (QPD). During the scan, the tip is brought to direct contact with sample surface. The movement of the reflected laser spot on the QPD is used as a read out of the interaction force between sample and tip which causes cantilever to deflect.

In AC mode, the cantilever is driven externally to oscillate at its natural resonant frequency. During the scan, interactions between tip and sample surface will modulate the

amplitude, phase and frequency of cantilever's vibrations, the change of which can be measured by lock-in detecting the deflection signal measured by the QPD at the cantilever's resonant frequency. Since tip only contacts the sample intermittently (or in so-called “non-contact” mode there is no contact), AC mode is a gentle imaging mode compared with contact mode and can be used in sensing long-range forces.

10.2.1 Conductive AFM

Conductive AFM is a variation of traditional AFM, which often operates in contact mode using a conductive probe to apply voltage and allow current flow through the AFM tip to the sample surface. In scanning mode, while collecting topography information is being collected, a separate current channel signal can be acquired to study sample resistivity distributions and dielectric properties[42,116].

If the tip is kept stationary conventional current-voltage characteristics can be recorded by (for example) sweeping the tip voltage and measuring the resulting current. This mode is similar to scanning tunneling spectroscopy except that the resolution is not as high..

Also, current that controllably flows to the sample surface can alter sample properties locally via processes like ionization, oxidation and charge transfer induced metal-insulator transition, thereby enabling nanoscale lithography patterning to be achieved.

10.2.2 Kelvin probe microscopy

Kevin probe force microscopy (KFM), also known as surface potential microscopy, maps out the work function distribution at a sample surface which can provide information about the local composition or electronic states of the sample studied.

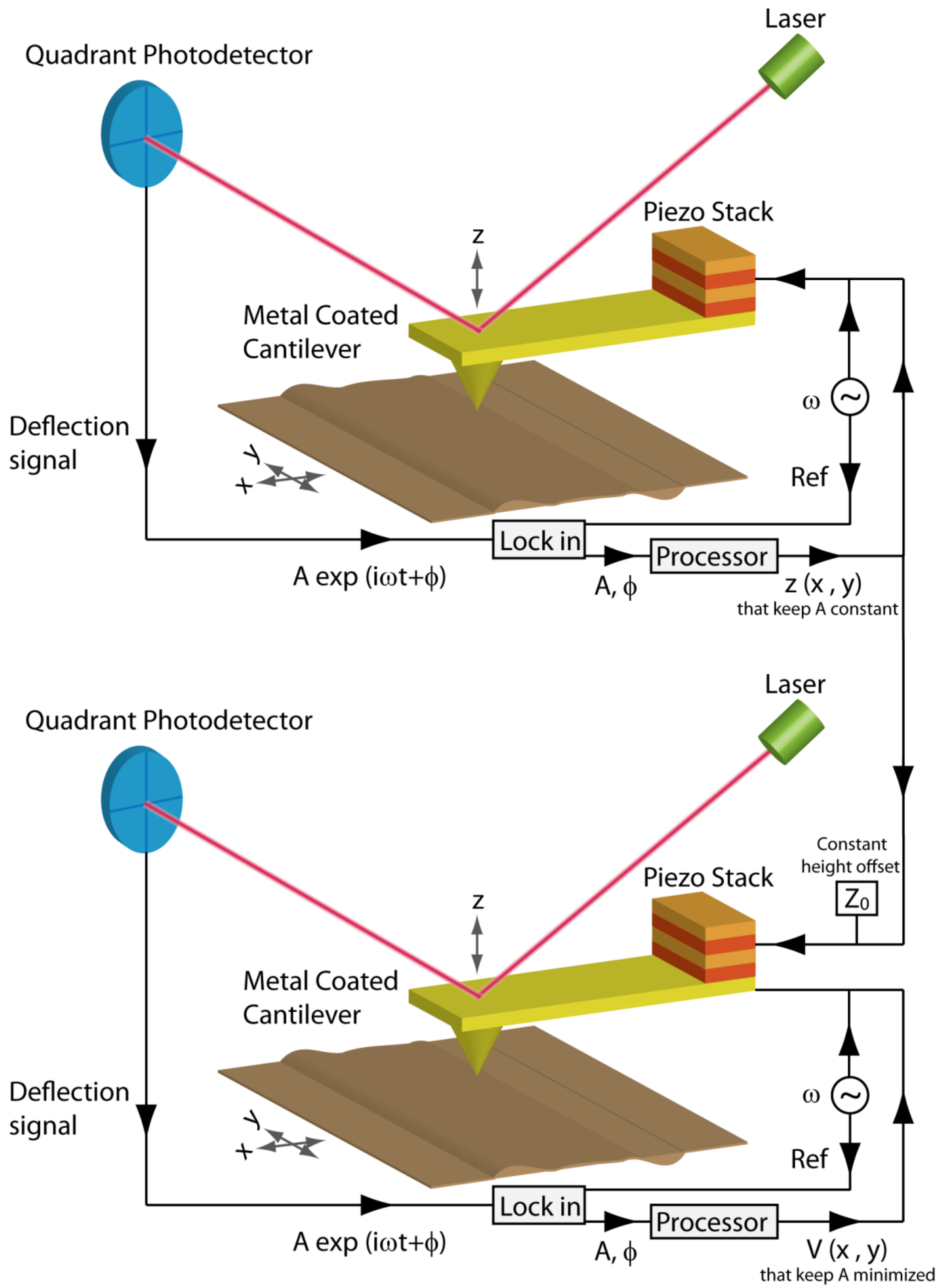

Figure 10-3 Illustration of typical operating method of Kelvin probe force microscopy

With KFM, a conductive AFM cantilever is used as a reference electrode that forms a capacitor with the surface. The capacitive interaction between tip and surface is measured to provide surface potential information. To distinguish the capacitive force from mechanical forces or other irrelevant long-range forces, one commonly used operating method involves two sequential imaging steps (Fig. 10-3). First, AFM is operated in normal AC mode and spatial distribution of height variation $z\ (x, y)$ is recorded. In the second step, using the already measured height profile, the cantilever is scanned with a constant distance from the sample surface. A sinusoidal voltage signal at the cantilever's resonant frequency $V_{AC}\sin(\omega t)$ as well as a DC voltage offset V is applied to the conductive AFM tip. The capacitive energy between the tip and sample surface is:

$$\begin{aligned} E_C &= \frac{1}{2}C(\Delta V)^2 = \frac{1}{2}C(V_{AC}\sin(\omega t) + V - U_{surf})^2 \\ &= \frac{1}{2}C[(V - U_{surf})^2 + \frac{1}{2}V_{AC}{}^2 + 2V_{AC}(V - U_{surf})\sin(\omega t) - \frac{1}{2}\cos(2\omega t)] \end{aligned} \quad (3.1)$$

Since the deflection signal is lock-in detected at ω, only term that is relevant is $CV_{AC}(V_{DC} - U_{surf})\sin(\omega t)$ which is proportional to the potential difference between tip and sample surface. During the scan, deflection signal at frequency ω is used as the feedback, and the potential V is adjusted so that cantilever's vibration at frequency ω is cancelled. In this way, spatial distribution of such a vibration nulling DC voltage applied to the tip will be a measurement of the surface potential profile $U_{surf}\,(x,y)$.

10.2.3 Piezo force microscopy

Piezoelectricity is a property of certain materials to generate an electric potential in response to a mechanical stress[117]. Piezoelectric effect is related to the dipole moment in materials, which can be induced by either ions in crystal lattice screened by asymmetry surrounding charges or a molecule with certain charge distributions. In piezoelectric materials, the dipole moment density, also called polarization P will change when stress is applied. This may be caused by the replacement or reconfiguration of the dipole inducing surrounding charges or reorientation of molecular dipole moment. Change in net polarization will vary the density of bound surface charges, which give rise to a macroscopic electric voltage.

Piezoelectric materials also show the opposite effect, where application of external electric field creates mechanical deformations. Ferroelectric materials, having a spontaneous nonzero net polarization, are also piezoelectric. The material expands if external electric field is parallel with the polarization direction and contracts if anti-parallel. When an AC voltage is applied, material deformation also oscillates in-phase or out-of-phase with the modulation field depending on the initial polarization direction (Fig. 10-4), which is called piezoresponse. This is the basic idea of how piezo-force microscopy works[118-119].

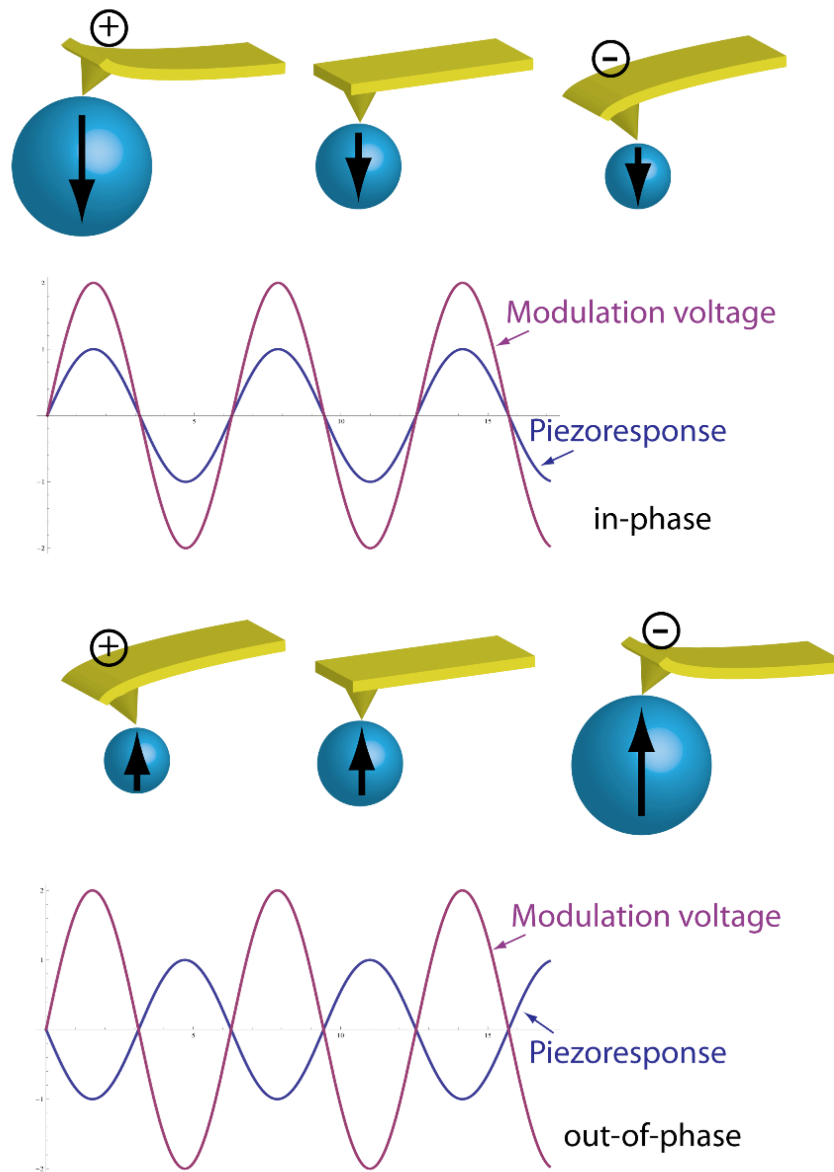

Figure 10-4 Illustration of in-phase and out-of-phase piezoresponse. Depend on the initial spontaneous polarization of the ferroelectric domain; the piezoresponse exhibits a phase difference.

During operation, a conductive probe scans in contact mode to acquire normal sample surface profile, at the same time, sum of an optional DC voltage and a small AC voltage is applied to the cantilever, whose frequency f is far off the fundamental frequency of the cantilever to avoid driving it resonantly. Deformation of the sample surface induced by the small AC

modulation voltage will periodically force to tip and deflect the cantilever. The piezoresponse is measured by lock-in detecting the cantilever deflection signal at frequency *f*. In a sample with ferroelectric domains, local polarization can be induced or changed by the DC voltage applied and later read out by piezoresponse.

10.3 ELECTRO-OPTIC EFFECT

10.3.1 Raman and Brillouin Scattering

Light scattering has long been an important method for studying material properties. When scattered by atoms or molecules, most photons are elastically scattered, which is called the Rayleigh scattering process, *e.g.* scattered light has the same wavelength as the incident light. However, a small amount of light is scattered inelastically with the scattered light having a difference wavelength.

Specifically in the case when light is inelastically scattered by vibration modes of crystal lattice (phonons), incident light either emits a phonon with the scattered light's frequency red shifted by an amount equal to the phonon frequency (Stokes) or absorbs a phonon with the scattered light's frequency blue shifted (anti-Stokes). Raman processes probe the interaction of light with optical phonons while Brillouin processes probe the interaction of light with acoustic phonons.

Raman scattering is a nonlinear electro-optic process. Consider an experiment where the incident light is monochromatic with frequency ω_I and wavevector k_I, spatial component of the associating electric field is:

$$E_I^i(\mathbf{r},t) = E_I^i e^{i(\mathbf{k}_I\cdot\mathbf{r}-\omega_I t)} \tag{3.2}$$

The polarization induced by incident field in the absence of any excitations of the medium is:

$$P^i(\mathbf{r},t) = \varepsilon_0 \chi^{ij}(\omega_I) E_I^j(\mathbf{r},t) \tag{3.3}$$

where χ is the linear susceptibility tensor of the medium at frequency. The excitation of the medium responding for inelastic scattering can be described with a space- and time-dependent amplitude:

$$X(\mathbf{r},t) = \sum_{\mathbf{q}} X(\mathbf{q},t) e^{i\mathbf{q}\cdot\mathbf{r}}. \tag{3.4}$$

The effect of the excitations is to modulate the wavefunctions and energy levels of the medium. The induced changes can be approximately represented to the first order term in perturbation theory which is linear to $X(\mathbf{q},t)$. The expression for polarization is replaced by:

$$P = \varepsilon_0(\chi E_I + \chi' X E_I), \tag{3.5}$$

where $\chi' = \left.\frac{\partial\chi}{\partial X}\right|_{X=0}$ is the second order susceptibility tensor. The linear polarization from the first term oscillates at the same frequency as the incident field and contributes to only elastic scattering. The second order polarization from the second term oscillates at frequency different from ω_I because X itself is a time dependent function. It can be seen that only vibration modes with X that gives a nonzero $\left.\frac{\partial\chi}{\partial X}\right|_{X=0}$ are so-called Raman active. The symmetry properties of the

scattering cross section are determined by the symmetry of χ' which is closely related to the medium's lattice symmetry.

10.3.2 Impulsive Stimulation and Probing Method

There are two conventional ways to realize optical excitation of coherent lattice vibrations through stimulated light scattering. One is to focus an intense laser of frequency ω_L into a medium. Raman-active vibration mode of frequency ω may be created by gaining energy from the phonon field.

The second method is to overlap two laser outputs, of frequencies and wave vectors (ω_1, $\mathbf{k}_1$) and (ω_2, $\mathbf{k}_2$), spatially and temporally in the medium with ω_1 - ω_2 = ω. Through stimulated scattering, a coherent traveling vibrational wave of frequency and wave vector (ω, $\mathbf{k} = \mathbf{k}_1 - \mathbf{k}_2$) is produced and amplified parametrically. This method permits selectivity in the vibrational mode which is to be excited.

In traditional Raman spectroscopy, a sample is illuminated with a laser beam. Light from the illuminated spot is collected with a lens and sent through a monochromator. Wavelengths close to the laser line, due to elastic Rayleigh scattering, are filtered out while the rest of the collected light is dispersed onto a detector where frequency spectrum is recorded. Stokes and anti-Stokes frequency shifts can be extracted from corresponding spectrum lines and later attribute to certain vibration modes in material studied.

Advances in ultrafast lasers make possible a time domain method to impulsively excite and probe vibrational modes in solids. Instead of having two exciting laser beams as in the

second method described above, excitation is achieved by a single laser pulse with pulse duration τ_L. For significant excitation to occur, τ_L must be much shorter than the period of the created vibration $\tau = 2\pi / \omega$ in order to exert a temporally impulsive driving force. This also can be understood in frequency domain. According to the uncertainty principle, bandwidth of the laser pulse is in the order of $\Psi_L \sim 1/\tau_L$. To obtain the amplification of the stimulated excitation through optical mixing of the Fourier components of the ultrashort incoming laser pulse, two frequency components meeting the condition $\omega_1 - \omega_2 = \omega$ must be found, which means Ψ_L must exceed the vibration frequency ω. In impulsive stimulated Raman and Brillouin scattering processes, photons with higher energy are converted to lower frequency photons to create phase coherent optical or acoustic phonons in the medium.

Coherent phonon oscillations in a medium can be detected by scattering of a second probe pulse with a variable delay relative to the first. The probe also exerts an impulsive driving force with a relative phase to the vibration in medium depending on the delay time. When in phase, energy is converted from the probe pulse to the vibration mode and the probe pulse leaves the medium red shifted; if out of phase, the probe pulse gains energy from the vibration mode and gets blue shifted. Similar time dependent momentum transfer between the probe pulse and the vibration mode as well as time-dependent polarization change of the probe can also occur, depending on the symmetry of the vibrational mode. These time dependent changes of the probe pulse can be measured to study the time domain dynamics of the vibrational mode.

10.4 HALL EFFECT MEASUREMENT

10.4.1 Classic Hall Effect

The Hall effect is the production of a voltage difference (the Hall voltage) across an electrical conductor, transverse to an electric current in the conductor and a magnetic field perpendicular to the current.

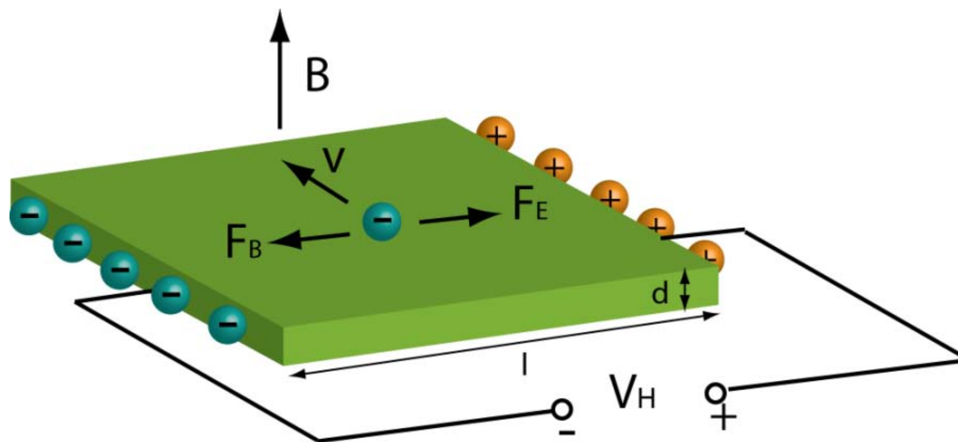

Figure 10-5 Illustration of classic Hall effect, charges accumulate at sample edges and induce a Hall voltage to balance the Lorentz force.

Current flowing in a conductor involves the movement of charge carriers. A carrier with charge q moving with a velocity **v** in an external magnetic B perpendicular to the motion direction will experience a Lorentz force $F_B = qvB$. The deflection of carriers depending on their charge polarity will cause different carriers to accumulate at the two sides of the conductor, the distance between which is l. The building of charges will induce a electric voltage V_H which will eventually exert a Coulomb force $F_E = V_H q / l$ in balance with the Lorentz force and put the carriers' movement into equilibrium (Fig. 10-5). This voltage is called the Hall voltage.

If the carrier density in the conductor of thickness *d* is *n,* current magnitude is *I*, then the average carrier velocity is $v = I / ndle$. Considering the balancing condition between Coulomb force and Lorentz force, it can be see that:

$$V_H e / l = IB / ndl \tag{3.6}$$

$$\Rightarrow R_H = \frac{V_H}{I} = \frac{B}{nde} = \frac{B}{n_S e} \tag{3.7}$$

where R_H is the Hall resistance and n_s is the sheet carrier density.

10.4.2 Conventional Magnetotransport Measurements

Transport experiments carried out in variable magnetic field can provide measurement of material parameters like sheet density *n* and carrier mobility μ.

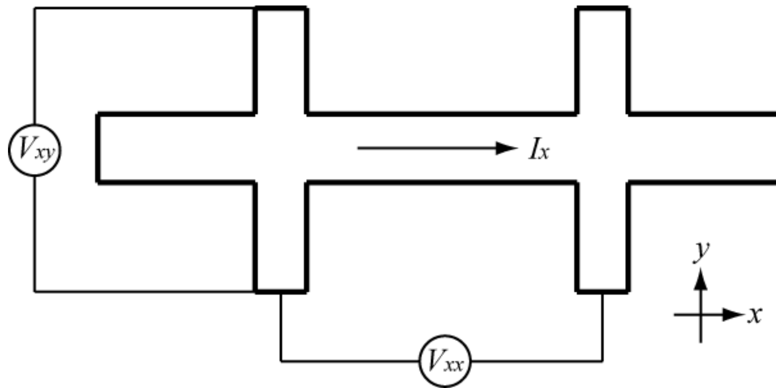

Figure 10-6 Schematic of conventional magneto transport measurement performed in a Hall bar structure.

Such measurement are usually performed in a Hall bar structure (Fig. 10-6). A constant current *I* is sourced in the main channel, and the longitudinal voltage V_{xx} is measured between two voltage sensing leads along the channel. Such a standard four-probe set up is used to extract the longitudinal resistance $R_{xx} = V_{xx} / I$. At the same time, transverse voltage across the channel V_{xy} is

measured as well to calculate the transverse resistance (Hall resistance) $R_{xy} = V_{xy} / I$. Knowing the geometric dimensions of the Hall bar, longitudinal and transverse resistivity ρ_{xx}, ρ_{xy} can then be calculated. Carrier density and mobility n, μ can be derived based on the following well known relationships:

$$\rho_{xx} = ne\mu \tag{3.8}$$

$$\rho_{xy} = \frac{B}{ne} \tag{3.9}$$

Generally in an isotropic medium, relationship between electric field $\vec{E}$ and current density $\vec{j}$ can be written as following:

$$\vec{E} = \overleftrightarrow{\rho}\vec{j} \tag{3.10}$$

where

$$\overleftrightarrow{\rho} = \begin{pmatrix} \rho_{xx} & \rho_{xy} \\ -\rho_{xy} & \rho_{xx} \end{pmatrix} = \begin{pmatrix} ne\mu & \frac{B}{ne} \\ -\frac{B}{ne} & ne\mu \end{pmatrix} \tag{3.11}$$

is the resistivity tensor. Accordingly the conductivity tensor $\overleftrightarrow{\sigma}$ is the reciprocal of $\overleftrightarrow{\rho}$:

$$\overleftrightarrow{\sigma} = \begin{pmatrix} \sigma_{xx} & -\sigma_{xy} \\ \sigma_{xy} & \sigma_{xx} \end{pmatrix} = \begin{pmatrix} \rho_{xx} & \rho_{xy} \\ -\rho_{xy} & \rho_{xx} \end{pmatrix}^{-1} = \frac{ne\mu}{1+(\mu B)^2}\begin{pmatrix} 1 & -\mu B \\ \mu B & 1 \end{pmatrix} \tag{3.12}$$

10.4.3 Quantum Hall Effect

Integer Quantum Hall Effect

The integer quantum Hall effect was discovered in 1980 by Klitzing, Dorda and Pepper [71]. They found that when a two dimensional system is a quantum Hall state, the conductivity tensor can be expressed as follows:

$$\overleftrightarrow{\sigma} = \begin{pmatrix} \sigma_{xx} & -\sigma_{xy} \\ \sigma_{xy} & \sigma_{xx} \end{pmatrix} = \begin{pmatrix} 0 & -\nu e^2/h \\ \nu e^2/h & 0 \end{pmatrix} \tag{3.13}$$

where h is the Plank's constant, e is the charge of the electron and ν is a small integer. In other words, transverse transport is quantized ($\sigma_{xy} = \nu e^2/h$, $\rho_{xy} = h/\nu e^2$) while longitudinal transport is lossless ($\sigma_{xx} = \rho_{xx} = 0$) (Fig. 10-7).

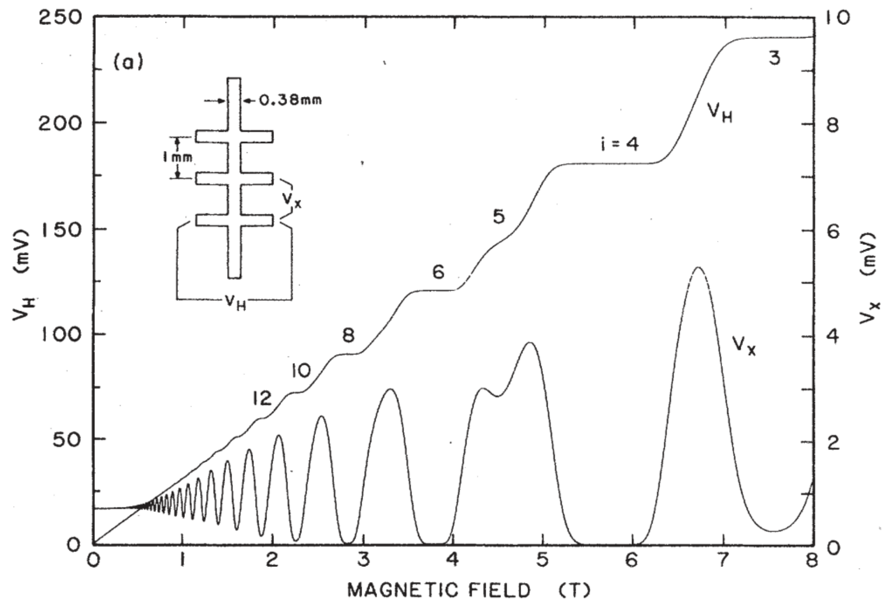

Figure 10-7 Example of quantum Hall effect measured in GaAs/AlGaAs heterostructures [120]. Transverse resistivity is quantized at quantum Hall states while longitudinal resistivity is minimized.

Integer Quantum Hall effect originates from the fact that in a quantum mechanical two dimensional electron gas system, under external magnetic field and low temperature, orbits of electrons are quantized to discrete values called Landau levels.

Consider the situation where 2D electron gas lies in the *x-y* plane with confinements in *x* and *y* directions having dimensions of *Lx* and L_y. The magnetic field *B* is in the *z* direction. Using the Landau gauge, the magnetic vector potential can be expressed as:

$$A_x = 0, \qquad A_y = Bx \tag{3.14}$$

then the Schrödinger equation takes the form:

$$\left(-\frac{\hbar^2}{2m}\partial_x^2 - \frac{\hbar^2}{2m}(\partial_y - ieBx/\hbar)^2 \right)\psi(x,y) = E\psi(x,y) \tag{3.15}$$

which is translationally invariant along the *y* direction and suggests a solution form:

$$\psi_n(x,y) = e^{iky} f_n(x) \tag{3.16}$$

Substituting this form back to (10.15), an eigenvalue equation can be obtained that can be mapped onto a harmonic oscillator:

$$\left(-\frac{\hbar^2}{2m}\partial_x^2 + \frac{\hbar^2}{2m}(k - eBx/\hbar)^2 \right) f_n(x) = E_n f_n(x) \tag{3.17}$$

with eigenenergy

$$E_n = \frac{\hbar^2 eB}{m}(n + \frac{1}{2}) \tag{3.18}$$

The wavefunction (10.16) is localized in the *x* direction around $x = \hbar k / eB$ but extended in *y* direction and highly degenerate regarding to value of *k*. Assuming a periodic boundary condition in the *y* direction, the values of *k* can be restricted to:

$$k_m = 2\pi m / L_y, \quad m \in \mathbb{N} \tag{3.19}$$

To ensure that the center of the wavefunction lies within the x confinement, values of k must meet the condition:

$$\Delta k \le eBL_x / \hbar \Rightarrow \Delta m \le \frac{eB}{h} L_x L_y \tag{3.20}$$

Therefore, in each energy level, there are a total of $\frac{eB}{h} L_x L_y$ degenerate states available.

If now apply an electric field in the x direction, a potential term of $V(x) = -eE_x x$ will be added. The wavefunction in ground state is then:

$$\psi_0(x, y) = e^{iky} e^{\frac{eB}{2}(x - \hbar k/eB - mE_x/eB^2)^2} \tag{3.21}$$

The current flux density in y direction is:

$$j_y^{0,k} = \frac{1}{2mi}(\psi_0^{\dagger} \partial_y \psi_0 - (\partial_y \psi_0^{\dagger})\psi_0) \tag{3.22}$$

After normalize the wavefunction and integrate j_y^0 along x direction, the current contributed from a single k state is eE / BL_y in the -y direction. The average current density, considering all available k states, is then:

$$j_y^0 = I_y / L_x = \frac{eE_x}{BL_y} \times \frac{eB}{h} L_x L_y / L_x = \frac{e^2}{h} E_x \tag{3.23}$$

If the carrier density in the system is n, then the total number of energy levels occupied is

$$\nu = n / \frac{eB}{h} = \frac{nh}{eB} \tag{3.24}$$

and the total current density is:

$$j_y = \frac{\nu e^2}{h} E_x \tag{3.25}$$

where v , known as the filling factor, is the number of energy levels that's occupied, and Hall conductivity $\sigma_{xy} = \frac{ie^2}{h}$ is quantized. Precise measurements found that, as long as the quantum Hall effect is observed, the quantization value is accurate to 10^{-8}, unaffected by geometrical imperfections or the presence of impurities and disorder.

Fractional Quantum Hall Effect

The fractional quantum Hall effect was discovered in 1982 by Tsui, Stormer and Gossard [58]. This effect is superficially similar to the integer quantum Hall effect in that there is a filling factor v can now take fractional values

$$v = \frac{p}{q} \tag{3.26}$$

where p and q are integers with no common factor. However, the physics behind this effect turned out to be much more subtle than for the integer quantum Hall effect, which is a single-particle phenomenon.

The mechanism of the fractional quantum Hall effect involves interactions between electrons. A theory in which fractionally charged quasiparticle are formed was first proposed by Laughlin [78] to explain fractional states corresponding to a filling factor with $p = 1; q = 2l + 1, l \in \mathbb{N}$. A composite fermion theory was later introduced by Jain [79] which extends to all filling factors of form $p / 2lp + 1$ where both p and l are integers..

Basic idea of the composite fermion theory is that strongly interacting electrons in a strong magnetic field B transform into weakly interacting composite fermions in a weaker effective magnetic field B', given by

$$B' = B - 2l\phi_0 n \tag{3.27}$$

where n is the carrier density and $\phi_0 = h/e$ is the flux quanta. By attaching $2l$ flux quanta to each electron, the repulsive Coulomb interaction between electrons is greatly screened. Electrons with filling factor ν are converted into composite fermions with filling factor

$$\nu' = n\phi_0 / |B'| \tag{3.28}$$

which gives

$$\nu = \frac{\nu'}{2l\nu' \pm 1} \tag{3.29}$$

The plus and minus sign correspond to situations when B' points parallel or antiparallel to B. The wavefunctions for interacting electrons at a given ν is

$$\Psi_\nu = \Phi_{\nu'} \prod_{j<k} (z_j - z_k)^{2p} \tag{3.30}$$

where $z_j = x_j - iy_j$ denotes the position of the jth electron, and $\Phi_{\nu'}$ are the Slater-determinant wavefunctions for non-interacting electrons with filling factor ν'.

When $2l = 1/\nu$, the effective magnetic field B' vanishes and the composite fermions fill a Fermi sea of their own. With nonzero B', composite fermion Landau levels are formed in analog with integer quantum Hall states with ν' being an integer number.

The local charge of a composite fermion, defined as the sum of its intrinsic charge ($-e$) and the charge of the screening cloud around it, takes value of $-e/(2l\nu' \pm 1)$.

BIBLIOGRAPHY

1 Ohtomo, A. & Hwang, H. Y. A high-mobility electron gas at the $LaAlO_3/SrTiO_3$ heterointerface. *Nature* **427**, 423-426 (2004).

2 Kalabukhov, A. *et al.* Effect of oxygen vacancies in the $SrTiO_3$ substrate on the electrical properties of the LaAlO3/SrTiO3 interface. *Physical Review B* **75** (2007).

3 Siemons, W. *et al.* Origin of charge density at $LaAlO_3$ on $SrTiO_3$ heterointerfaces: Possibility of intrinsic doping. *Physical Review Letters* **98** (2007).

4 Herranz, G. *et al.* High Mobility in $LaAlO_3/SrTiO_3$ Heterostructures: Origin, Dimensionality, and Perspectives. *Physical Review Letters* **98**, 216803-216804 (2007).

5 Pentcheva, R. & Pickett, W. E. Charge localization or itineracy at $LaAlO_3/SrTiO_3$ interfaces: Hole polarons, oxygen vacancies, and mobile electrons. *Physical Review B* **74**, (2006).

6 Janicka, K., Velev, J. P. & Tsymbal, E. Y. Quantum Nature of Two-Dimensional Electron Gas Confinement at LaAlO3/SrTiO3 Interfaces. *Physical Review Letters* **102**, 106803 (2009).

7 Thiel, S., Hammerl, G., Schmehl, A., Schneider, C. W. & Mannhart, J. Tunable quasi-two-dimensional electron gases in oxide heterostructures. *Science* **313**, 1942-1945 (2006).

8 Huijben, M. *et al.* Electronically coupled complementary interfaces between perovskite band insulators. *Nature Materials* **5**, 556-560 (2006).

9 Basletic, M. *et al.* Mapping the spatial distribution of charge carriers in $LaAlO_3/SrTiO_3$ heterostructures. *Nature Materials* **7**, 621-625 (2008).

10 Nakagawa, N., Hwang, H. Y. & Muller, D. A. Why some interfaces cannot be sharp. *Nature Materials* **5**, 204-209 (2006).

11 Brinkman, A. *et al.* Magnetic effects at the interface between non-magnetic oxides. *Nature Materials* **6**, 493-496 (2007).

12 Popovic, Z. S., Satpathy, S. & Martin, R. M. Origin of the Two-Dimensional Electron Gas Carrier Density at the $LaAlO_3$ on $SrTiO_3$ Interface. *Physical Review Letters* **101**, 256801 (2008).

13 Lee, J. & Demkov, A. A. Charge origin and localization at the n-type $SrTiO_3/LaAlO_3$ interface. *Physical Review B* **78**, 193104 (2008).

14 Warusawithana, M. P. *unpublished*.

15 Reyren, N. *et al.* Superconducting Interfaces Between Insulating Oxides. *Science*, 1146006(2007).
16 Caviglia, A. D. *et al.* Electric field control of the $LaAlO_3/SrTiO_3$ interface ground state. *Nature* **456**, 624-627(2008).
17 Schooley, J. F., Hosler, W. R. & Cohen, M. L. Superconductivity in semiconducting $SrTiO_3$. *Phys. Rev. Lett.* **12**, 474-475 (1964).
18 Brinkman, A. *et al.* Magnetic effects at the interface between non-magnetic oxides. *Nat Mater* **6**, 493-496 (2007).
19 Neville, R. C., Hoeneisen, B. & Mead, C. A. Permittivity of strontium titanate. *Journal of Applied Physics* **43**, 2124 (1972).
20 Warusawithana, M. P. *et al.* A Ferroelectric Oxide Made Directly on Silicon. *Science* **324**, 367-370 (2009).
21 Muller, K. A. & Bukard, H. $SrTiO_3$: An intrinsic quantum paraelectric below 4 K. *Phys. Rev. B* **19**, 3593 (1979).
22 Hulm, J. K., Ashkin, M., Deis, D. W. & Jones, C. K. Progress Low Temp. *Phys* **6**, 205 (1970).
23 Uwe, H. & Sakudo, T. Stress-induced ferroelectricity and soft phonon modes in $SrTiO_3$. *Physical Review B* **13**, 271 (1976).
24 Pertsev, N. A., Tagantsev, A. K. & Setter, N. Phase transitions and strain-induced ferroelectricity in $SrTiO_3$ epitaxial thin films. *Physical Review B* **61**, R825-R829 (2000).
25 Haeni, J. H. *et al.* Room-temperature ferroelectricity in strained $SrTiO_3$. *Nature* **430**, 758-761 (2004).
26 Tenne, D. A. *et al.* Probing nanoscale ferroelectricity by ultraviolet Raman spectroscopy. *Science* **313**, 1614 (2006).
27 Bousquet, E. *et al.* Improper ferroelectricity in perovskite oxide artificial superlattices. *Nature* **452**, 732-734(2008).
28 Cen, C. *et al.* Nanoscale control of an interfacial metal-insulator transition at room temperature. *Nature Materials* **7**, 298-302(2008).
29 Schneider, C. W., Thiel, S., Hammerl, G., Richter, C. & Mannhart, J. Microlithography of electron gases formed at interfaces in oxide heterostructures. *Applied Physics Letters* **89** (2006).
30 Ohtomo, A., Muller, D. A., Grazul, J. L. & Hwang, H. Y. Artificial charge-modulation in atomic-scale perovskite titanate superlattices. *Nature* **419**, 378-380 (2002).
31 Ohtomo, A. & Hwang, H. Y. A high-mobility electron gas at the $LaAlO_3/SrTiO_3$ heterointerface. *Nature* **441**, 120-120 (2006).
32 Ohtomo, A. & Hwang, H. Y. Corrigendum: A high-mobility electron gas at the $LaAlO_3/SrTiO_3$ heterointerface. *Nature* **441**, 120-120 (2006).
33 Huijben, M. *et al.* Electronically coupled complementary interfaces between perovskite band insulators. *Nat Mater* **5**, 556-560 (2006).

34 Hotta, Y., Susaki, T. & Hwang, H. Y. Polar discontinuity doping of the $LaVO_3/SrTiO_3$ interface. *Physical Review Letters* **99**, 236805 (2007).

35 Okamoto, S., Millis, A. J. & Spaldin, N. A. Lattice relaxation in oxide heterostructures: LaTiO3/SrTiO3 superlattices. *Physical Review Letters* **97**, 056802 (2006).

36 Pentcheva, R. & Pickett, W. E. Charge localization or itineracy at $LaAlO_3/SrTiO_3$ interfaces: Hole polarons, oxygen vacancies, and mobile electrons. *Physical Review B* **74**, 7 (2006).

37 Ahn, C. H., Triscone, J. M. & Mannhart, J. Electric field effect in correlated oxide systems. *Nature* **424**, 1015-1018 (2003).

38 Helmolt, R. v., Wecker, J., Holzapfel, B., Schultz, L. & Samwer, K. Giant negative magnetoresistance in perovskitelike $La_{2/3}Ba_{1/3}MnO_x$ ferromagnetic films. *Phys. Rev. Lett.* **71**, 2331 (1993).

39 Levi, B. G. Interface between nonmagnetic insulators may be ferromagnetic and conducting. *Phys. Today* **60**, 23 (2007).

40 Eckstein, J. N. Oxide interfaces: Watch out for the lack of oxygen. *Nat Mater* **6**, 473-474 (2007).

41 Ahn, C. H. *et al.* Local, nonvolatile electronic writing of epitaxial $Pb(Zr_{0.52}Ti_{0.48})O_3/SrRuO_3$ heterostructures. *Science* **276**, 1100-1103 (1997).

42 Frammelsberger, W., Benstetter, G., Kiely, J. & Stamp, R. C-AFM-based thickness determination of thin and ultra-thin SiO2 films by use of different conductive-coated probe tips. *Applied Surface Science* **253**, 3615-3626 (2007).

43 Li, H. *et al.* Two-dimensional growth of high-quality strontium titanate thin films on Si. *Journal of Applied Physics* **93**, 4521-4525 (2003).

44 Cen, C., Thiel, S., Mannhart, J. & Levy, J. Oxide Nanoelectronics on Demand. *Science* **323**, 1026-1030(2009).

45 Whitesides, G. M., Mathias, J. P. & Seto, C. T. Molecular self-assembly and nanochemistry: A chemical strategy for the synthesis of nanostructures. *Science* **254**, 1312-1319 (1991).

46 Reed, M. A., Zhou, C., Muller, C. J., Burgin, T. P. & Tour, J. M. Conductance of a molecular junction. *Science* **278**, 252-254 (1997).

47 Andres, R. P. *et al.* Self-assembly of a two-dimensional superlattice of molecularly linked metal clusters. *Science* **273**, 1690-1693 (1996).

48 Leonard, D., Krishnamurthy, M., Reaves, C. M., Denbaars, S. P. & Petroff, P. M. Direct formation of quantum-sized dots from uniform coherent islands of InGaAs on GaAs-surfaces. *Applied Physics Letters* **63**, 3203-3205 (1993).

49 Collins, P. G., Zettl, A., Bando, H., Thess, A. & Smalley, R. E. Nanotube nanodevice. *Science* **278**, 100-103 (1997).

50 Bachtold, A., Hadley, P., Nakanishi, T. & Dekker, C. Logic circuits with carbon nanotube transistors. *Science* **294**, 1317-1320 (2001).

51 Duan, X. F., Huang, Y., Cui, Y., Wang, J. F. & Lieber, C. M. Indium phosphide nanowires as building blocks for nanoscale electronic and optoelectronic devices. *Nature* **409**, 66-69 (2001).
52 Klein, D. L., Roth, R., Lim, A. K. L., Alivisatos, A. P. & McEuen, P. L. A single-electron transistor made from a cadmium selenide nanocrystal. *Nature* **389**, 699-701 (1997).
53 Snow, E. S. & Campbell, P. M. Fabrication of Si nanostructures with an atomic-force microscope. *Applied Physics Letters* **64**, 1932-1934 (1994).
54 Chou, S. Y., Krauss, P. R. & Renstrom, P. J. Nanoimprint lithography. *Journal of Vacuum Science & Technology B* **14**, 4129-4133 (1996).
55 Piner, R. D., Zhu, J., Xu, F., Hong, S. H. & Mirkin, C. A. "Dip-pen" nanolithography. *Science* **283**, 661-663 (1999).
56 Heinrich, A. J., Lutz, C. P., Gupta, J. A. & Eigler, D. M. Molecule cascades. *Science* **298**, 1381-1387 (2002).
57 Dingle, A. R., Stormer, A. H. L., Gossard, A. A. C. & Wiegmann, A. W. Electron mobilities in modulation-doped semiconductor heterojunction superlattices. *Appl. Phys. Lett.* **33**, 665-667 (1978).
58 Tsui, D. C., Stormer, H. L. & Gossard, A. C. Two-Dimensional Magnetotransport in the Extreme Quantum Limit. *Phys. Rev. Lett.* **48**, 1559 (1982).
59 Albina, J. M., Mrovec, M., Meyer, B. & Elsasser, C. Structure, stability, and electronic properties of $SrTiO_3/LaAlO_3$ and $SrTiO_3/SrRuO_3$ interfaces. *Physical Review B* **76** (2007).
60 Barrett, J. H. Dielectric Constant in Perovskite Type Crystals. *Physical Review* **86**, 118 (1952).
61 Fuchs, D., Schneider, C. W., Schneider, R. & Rietschel, H. High dielectric constant and tunability of epitaxial SrTiO3 thin film capacitors. *Journal of Applied Physics* **85**, 7362-7369 (1999).
62 Lippmaa, M. *et al.* Step-flow growth of $SrTiO_3$ thin films with a dielectric constant exceeding 10(4). *Applied Physics Letters* **74**, 3543-3545 (1999).
63 Weaver, H. E. Dielectric properties of single crystals of $SrTiO_3$ at low temperatures. *Journal of Physics and Chemistry of Solids* **11**, 274, IN275-IN276, 275-277 (1959).
64 Antons, A., Neaton, J. B., Rabe, K. M. & Vanderbilt, D. Tunability of the dielectric response of epitaxially strained $SrTiO_3$ from first principles. *Physical Review B* **71** (2005).
65 Bouzehouane, K. *et al.* Enhanced dielectric properties of $SrTiO_3$ epitaxial thin film for tunable microwave devices. *Applied Physics Letters* **80**, 109-111 (2002).
66 Hemberger, J., Lunkenheimer, P., Viana, R., Bohmer, R. & Loidl, A. Electric-Field-Dependent Dielectric-Constant And Nonlinear Susceptbility IN $SrTiO_3$. *Physical Review B* **52**, 13159-13162 (1995).

67 Park, K. C. & Cho, J. H. Electric field dependence of ferroelectric phase transition in epitaxial $SrTiO_3$ films on $SrRuO_3$ and $La_{0.5}Sr_{0.5}CoO_3$. *Applied Physics Letters* **77**, 435-437 (2000).
68 Hellberg, S. (unpublished).
69 Hoppler, J. *et al.* X-ray study of structural domains in the near-surface region of $SrTiO_3$ substrates with $Y_{0.6}Pr_{0.4}Ba_2Cu_3O_7/La_{2/3}Ca_{1/3}MnO_3$ superlattices grown on top. *Physical Review B* **78** (2008).
70 Jena, D. & Konar, A. Enhancement of carrier mobility in semiconductor nanostructures by dielectric engineering. *Physical Review Letters* **98** (2007).
71 Klitzing, K. v., Dorda, G. & Pepper, M. New Method for High-Accuracy Determination of the Fine-Structure Constant Based on Quantized Hall Resistance. *Physical Review Letters* **45**, 494 (1980).
72 Novoselov, K. S. *et al.* Two-dimensional gas of massless Dirac fermions in graphene. *Nature* **438**, 197-200 (2005).
73 Zhang, Y., Tan, Y. W., Stormer, H. L. & Kim, P. Experimental observation of the quantum Hall effect and Berry's phase in graphene. *Nature* **438**, 201-204 (2005).
74 Tsukazaki, A. *et al.* Quantum Hall effect in polar oxide heterostructures. *Science* **315**, 1388-1391 (2007).
75 Van Zalk, M. *et al.* Magnetoresistance oscillations and relaxation effects at the $SrTiO_3/LaAlO_3$ interface. *Arxiv preprint arXiv:0806.4450* (2008).
76 Shibuya, K., Ohnishi, T., Sato, T. & Lippmaa, M. Metal-insulator transition in $SrTiO_3$ induced by field effect. *Journal of Applied Physics* **102**, 083713 (2007).
77 Mattheiss, L. F. Energy Bands for $KNiF_3$, $SrTiO_3$, $KMoO_3$, and $KTaO_3$. *Physical Review B* **6**, 4718-4740 (1972).
78 Laughlin, R. B. Anomalous Quantum Hall Effect: An Incompressible Quantum Fluid with Fractionally Charged Excitations. *Physical Review Letters* **50**, 1395 (1983).
79 Jain, J. K. Composite-fermion approach for the fractional quantum Hall effect. *Physical review letters* **63**, 199-202 (1989).
80 Sakaki, H. Scattering suppression and high-mobility effect of size-quantized electrons in ultrafine semiconductor wire structures. *Japanese Journal of Applied Physics* **19**, L735-L738 (1980).
81 Timp, G., Behringer, R., Cunningham, J. E. & Howard, R. E. Fractional quantum Hall effect in one dimension. *Physical Review Letters* **63**, 2268 (1989).
82 Kvon, Z. D. *et al.* Quantum Hall effect in a single-mode wire. *Semiconductors* **33**, 1238-1240 (1999).
83 Buttiker, M. Scattering theory of thermal and excess noise in open conductors. *Physical review letters* **65**, 2901-2904 (1990).
84 Ricketts, B. W. & Kemeny, P. C. Quantum Hall effect devices as circuit elements. *Journal of Physics D: Applied Physics* **21**, 483-487 (1988).

85 Jain, J. K. & Kivelson, S. A. Quantum Hall effect in quasi one-dimensional systems: Resistance fluctuations and breakdown. *Physical Review Letters* **60**, 1542 (1988).
86 Fang, F. F. & Stiles, P. J. Quantized magnetoresistance in two-dimensional electron systems. *Physical Review B* **27**, 6487 (1983).
87 Beenakker, C. W. J. Edge channels for the fractional quantum Hall effect. *Physical Review Letters* **64**, 216 (1990).
88 Hirai, H. & Komiyama, S. Linear magnetoresistance due to an inhomogeneous electron-density distribution in a two-dimensional electron gas. *Solid State Communications* **72**, 1033-1037 (1989).
89 Endo, A. & Iye, Y. Small amplitude low-field magnetoresistance oscillation in unidirectional lateral superlattices: Geometric resonance of Bragg-reflected cyclotron orbits. *Physical Review B* **71**, 081303 (2005).
90 Wilczek, F. *Fractional statistics and anyon superconductivity*. (World Scientific Pub Co Inc, 1990).
91 Nayak, C., Simon, S. H., Stern, A., Freedman, M. & Das Sarma, S. Non-Abelian anyons and topological quantum computation. *Reviews of Modern Physics* **80**, 1083-1159 (2008).
92 Das Sarma, S., Freedman, M. & Nayak, C. Topologically Protected Qubits from a Possible Non-Abelian Fractional Quantum Hall State. *Physical Review Letters* **94**, 166802 (2005).
93 Suzuki, M. *J. Ceram. Soc. Jan. Int. Ed* **103**, 1088 (1995).
94 Vettiger, P. & Bining, G. *Sci. Am.* **288**, 47 (2003).
95 Wu, Y. R. & Singh, J. Polar heterostructure for multifunction devices: Theoretical studies. *IEEE Transactions on Electron Devices* **52**, 284-293 (2005).
96 Morton, J. A. *U.S. Patent 2,791,761* (1957).
97 Chang, L. L. *IBM TECH DISCL B* **14**, 1250 (1971).
98 Kourkoutis, L. F. *et al.* Imaging the phase separation in atomically thin buried SrTiO3 layers by electron channeling. *Physical Review Letters* **100**, 036101 (2008).
99 Tybell, T., Ahn, C. H. & Triscone, J. M. Control and imaging of ferroelectric domains over large areas with nanometer resolution in atomically smooth epitaxial Pb(Zr0.2Ti0.8)O-3 thin films. *Applied Physics Letters* **72**, 1454-1456 (1998).
100 Tybell, T., Ahn, C. H. & Triscone, J. M. Ferroelectricity in thin perovskite films. *Applied Physics Letters* **75**, 856-858 (1999).
101 Lichtensteiger, C. *et al.* Monodomain to polydomain transition in ferroelectric $PbTiO_3$ thin films with $La_{0.67}Sr_{0.33}MnO_3$ electrodes. *Applied Physics Letters* **90**, 2433757 (2007).
102 Woicik, J. C. *et al.* Ferroelectric distortion in $SrTiO_3$ thin films on Si(001) by x-ray absorption fine structure spectroscopy: Experiment and first-principles calculations. *Physical Review B* **75**, 140103 (2007).
103 Fong, D. D. *et al.* Ferroelectricity in ultrathin perovskite films. *Science* **304**, 1650-1653 (2004).

104 Junquera, J., Zimmer, M., Ordejon, P. & Ghosez, P. First-principles calculation of the band offset at $BaO/BaTiO_3$ and $SrO/SrTiO_3$ interfaces. *Physical Review B* **67**, 155327 (2003).

105 Ghosez, P. & Rabe, K. M. Microscopic model of ferroelectricity in stress-free $PbTiO_3$ ultrathin films. *Applied Physics Letters* **76**, 2767-2769 (2000).

106 Stengel, M., Vanderbilt, D. & Spaldin, N. A. Enhancement of ferroelectricity at metal/oxide interfaces. *Nature Materials* **8**, 392-397 (2009).

107 Robertson, J. & Chen, C. W. Schottky barrier heights of tantalum oxide, barium strontium titanate, lead titanate, and strontium bismuth tantalate. *Applied Physics Letters* **74**, 1168 (1999).

108 Chambers, S. A., Liang, Y., Yu, Z., Droopad, R. & Ramdani, J. Band offset and structure of $SrTiO_3$/Si(001) heterojunctions. *J. Vac. Sci. Technol. A-Vac. Surf. Films* **19**, 934-939 (2001).

109 Junquera, J. & Ghosez, P. Critical thickness for ferroelectricity in perovskite ultrathin films. *Nature* **422**, 506-509(2003).

110 Forst, C. J., Ashman, C. R., Schwarz, K. & Blochl, P. E. The interface between silicon and a high-k oxide. *Nature* **427**, 53-56(2004).

111 Ross. (U.S.Patents, 1957).

112 Mathews, S., Ramesh, R., Venkatesan, T. & Benedetto, J. Ferroelectric field effect transistor based on epitaxial perovskite heterostructures. *Science* **276**, 238 (1997).

113 Vogt, H. & Rossbroich, G. Accurate determination of the far-infrared dispersion in SrTiO3 by hyper-Raman spectroscopy. *Physical Review B* **24**, 3086 (1981).

114 Rugar, D. & Hansma, P. Atomic force microscopy. *Phys. Today* **43**, 23-30 (1990).

115 Meyer, E. & Palmer, R. Atomic force microscopy. *Progress in surface science* **41**, 3-3 (1992).

116 Olbrich, A., Ebersberger, B. & Boit, C. Conducting atomic force microscopy for nanoscale electrical characterization of thin SiO_2. *Applied Physics Letters* **73**, 3114-3116 (1998).

117 Ikeda, T. *Fundamentals of piezoelectricity*. (Oxford University Press Oxford, 1990).

118 Christman, J. A., R. R. Woolcott, J., Kingon, A. I. & Nemanich, R. J. Piezoelectric measurements with atomic force microscopy. *Applied Physics Letters* **73**, 3851-3853 (1998).

119 Kolosov, O., Gruverman, A., Hatano, J., Takahashi, K. & Tokumoto, H. Nanoscale Visualization and Control of Ferroelectric Domains by Atomic Force Microscopy. *Physical Review Letters* **74**, 4309 (1995).

120 Cage, M. E., Dziuba, R. F. & Field, B. F. A test of the quantum Hall effect as a resistance standard. *IEEE transactions on instrumentation and measurement* **34**, 301-303 (1985).